



## 저작자표시-비영리-변경금지 2.0 대한민국

이용자는 아래의 조건을 따르는 경우에 한하여 자유롭게

- 이 저작물을 복제, 배포, 전송, 전시, 공연 및 방송할 수 있습니다.

다음과 같은 조건을 따라야 합니다:



저작자표시. 귀하는 원저작자를 표시하여야 합니다.



비영리. 귀하는 이 저작물을 영리 목적으로 이용할 수 없습니다.



변경금지. 귀하는 이 저작물을 개작, 변형 또는 가공할 수 없습니다.

- 귀하는, 이 저작물의 재이용이나 배포의 경우, 이 저작물에 적용된 이용허락조건을 명확하게 나타내어야 합니다.
- 저작권자로부터 별도의 허가를 받으면 이러한 조건들은 적용되지 않습니다.

저작권법에 따른 이용자의 권리는 위의 내용에 의하여 영향을 받지 않습니다.

이것은 [이용허락규약\(Legal Code\)](#)을 이해하기 쉽게 요약한 것입니다.

[Disclaimer](#)

공학박사 학위논문

**Evaluation of Residual Stress Using  
Instrumented Wedge Indentation  
: Stress Directionality and Magnitude**

**Wedge 연속압입시험을 활용한  
잔류응력 방향성 및 크기 평가**

2017년 2월

서울대학교 대학원

재료공학부

안 희 준



# Evaluation of Residual Stress Using Instrumented Wedge Indentation : Stress Directionality and Magnitude

Wedge 연속압입시험을 활용한  
잔류응력 방향성 및 크기 평가

지도교수 권 동 일

이 논문을 공학박사 학위논문으로 제출함  
2016년 12월

서울대학교 대학원  
재료공학부  
안 희 준

안희준의 박사학위논문을 인준함  
2016년 12월

위 원 장

오 유 환



부위원장

권 동 일



위 원

주영창



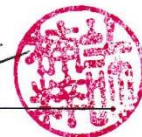
위 원

이승건



위 원

허남두





# **Abstract**

Ahn, Hee-Jun

Department of Materials Science and Engineering

The Graduate School

Seoul National University

Safety and reliability assessments are of vital importance in preventing accident because the failure of structures induces not only extensive damage but also loss of life, and requires huge effort and expense for recovery. In order to prevent unexpected accidents or failures, the stress states in structures must be considered. In particular, residual stress is defined as a stress state that exists in bulk materials or components without external load or other sources of stress. Residual stress arises in materials in almost every processing and manufacturing procedure. When residual stress is combined with external applied stress, some structure can fail at stresses beneath the yield strength of homogeneous and bulk material. In addition, residual stresses are detrimental to the performance and reliability of in-service structures. For these reasons, the quantitative assessment of residual stress is fundamental for the safe use and

economical maintenance of industrial structures and facilities.

Instrumented indentation testing (IIT) was developed to measure mechanical properties by analyzing the indentation load-depth curve. Over the last several decades, IIT has been extended beyond hardness and elastic modulus to methodologies evaluating for tensile properties, fracture toughness, fatigue characteristics, impact properties, interface adhesion and residual stress.

IIT evaluates residual stress by looking at the difference in the indentation load-depth curve for the stress-free and stressed states. Previous research has evaluated the average surface residual stress using a Vickers indenter, and has also obtained information on the principal direction and stress ratio using a two-fold symmetric indenter, for example, Knoop indenter. As it can be necessary (as in testing curved pipes, or narrow welding regions) to evaluate nonequibiaxial residual stress within a small indent area, here we suggest a novel way to evaluate the directionality of the residual stress,  $p$ , using a wedge indenter characterized by two parameters, edge length and inclined angle.

The present work describes a new wedge indentation model for evaluating surface nonequibiaxial residual stresses without change in indenter. We develop a wedge-indentation-mechanics model based on

predetermined conversion factors determined by IITs for various uniaxial stressed states combined with finite element analysis (FEA) simulations. With this new model with pre-information on principal direction, two wedge indentation tests with respect to principal directions are required. On the other hand, without information on principal directions, four wedge indentations at intervals 45 degrees from some randomly chosen direction are needed. Principal directions and stress ratio are evaluated with two sets of load difference ratios at 90-degree intervals and a predetermined conversion factor ratio. The sum of the surface residual stress is obtained from the sum of load difference directionality with 90- degree intervals and the sum of conversion factors.

To verify the suggested wedge indentation model, indentation tests were performed on 15 combinations of cruciform specimens, applied stress and various principal directions using stress-generating jigs. Additionally, the biaxial residual stress as evaluated using the new model are compared with values from the Vickers indentation model.

**Keyword:** Residual stress; Wedge indenter; Conversion factor; Principal direction; Stress magnitude; Stress directionality

**Student Number:** 2010-20614





# Contents

<b>Abstract</b> .....	i
<b>Contents</b> .....	v
<b>List of Tables</b> .....	viii
<b>List of Figures</b> .....	ix
<b>Chapter 1. Introduction</b> .....	1
1.1. Objective of the Thesis .....	2
1.2. Outline of the Thesis .....	8
<b>Chapter 2. Research Background</b> .....	11
2.1. Definition of Residual Stress .....	12
2.1.1. Residual Stress on Weldment .....	14
2.1.2. Residual Stress on Thin Film .....	16
2.2. Measurement of Residual Stress .....	17
2.2.1. Destructive Methods .....	17
2.2.2. Non-destructive Methods .....	21
2.3. Instrumented Indentation Test .....	24
2.3.1. Basic Properties .....	26
2.3.2. Advanced Properties .....	30
2.4. Evaluation of Residual Stress using indentation .....	37
2.4.1. Vickers Indentation Model .....	37

2.4.2. Knoop Indentation Model .....	39
2.5. Limitations of Previous Methods .....	48
<b>Chapter 3. Wedge Indentation Test Setup .....</b>	<b>73</b>
3.1. Wedge Indenter Shape .....	74
3.1.1. Included Angle .....	75
3.1.2. Edge Length .....	76
3.2. Setting Machine Compliance and Zero Index .....	77
3.2.1. Machine Compliance .....	77
3.2.2. Zero Index of Wedge Indenter .....	80
3.3 Determination of Indent Interval .....	81
<b>Chapter 4. Determination of Conversion Factor (<math>\beta</math>) for Evaluating Stress Magnitude and Directionality ....</b>	<b>95</b>
4.1. Modeling of Conversion Factor with Uniaxial stress state ...	96
4.2. Physical Meaning of Conversion Factor Ratio .....	100
4.2.1. Subjected area of Penetrating Indenter .....	101
4.2.2. Subjected area of Plastic Zone Beneath Indenter .....	102
4.3. Indentation Dependency of Conversion Factor Ratio .....	103
<b>Chapter 5. Modeling for Evaluating Residual Stress Magnitude and Directionality .....</b>	<b>115</b>
5.1. Modeling for Evaluating Sum of Biaxial Residual Stress Magnitudes with Wedge Indentation .....	116

5.2. Modeling for Evaluating Residual Stress Directionality and Magnitude with Wedge Indentation .....	119
5.2.1. Known Principal Direction .....	119
5.2.2. Unknown Principal Direction .....	121
<b>Chapter 6. Experimental Verification of Model .....</b>	<b>131</b>
6.1. Experimental Apparatus .....	132
6.1.1. Testing Equipment and Specimens .....	132
6.1.2. Stress Generating Jig .....	134
6.2. Finite Element Analysis Condition .....	135
6.3. Results and Discussion .....	137
6.3.1. Verification of Experiments with Stress-generating jig .....	137
6.3.2. Comparison of Residual Stress Summation with Previous Vickers Model .....	138
<b>Chapter 7. Conclusion .....</b>	<b>153</b>
<b>Reference .....</b>	<b>157</b>
<b>Abstract in Korean (초록) .....</b>	<b>165</b>

## List of Tables

### Table 4.1

Mechanical properties used for plastic zone size ratio evaluation.

### Table 4.2

Plastic zone size of two directions and the ratio.

### Table 6.1

Experimental and simulation conditions for determination of conversion factors: various materials and applied tensile stress states.

### Table 6.2

Mechanical properties of materials for model verification.

### Table 6.3

Applied stress state conditions and principal direction for model verification.

### Table 6.4

Summary of applied stress state conditions and evaluated stress magnitude and directionality.

## List of Figures

**Fig. 2.1** A thermal switch that turns on/off depending on the temperature change [26].

**Fig. 2.2** Residual stress distributions in plate butt joint [27].

**Fig. 2.3** Schematic illustrations of heat cycles in welding and residual stress distribution [27].

**Fig. 2.4** Residual stress effect on thin film [24].

**Fig. 2.5** Mechanisms of thermal stress, intrinsic stress and epitaxial stress [24].

**Fig. 2.6** Schematic illustration of the force-per-width and micro structural characteristics for high-mobility and low-mobility films; (a) compressive stress in island by surface energy (tension) (b) tensile stress by elimination of grain boundary (grain growth) (c) compressive stress by continuous inputting impurity and extra atom and (d) tensile stress by substitution of island surface with grain boundary [38].

**Fig. 2.7** Hole-drilling method for evaluating residual stress.

**Fig. 2.8** Schematic illustration of sectioning method.

**Fig. 2.9** Schematic drawing of contour method based on super position principle [26].

**Fig. 2.10** Residual stress distribution on a plane which is measured by slitting method [26].

**Fig. 2.11** Schematic drawing of curvature method.

**Fig. 2.12** Schematic drawing of X-ray diffraction method.

**Fig. 2.13** Determined properties from indentation load-depth curve.

**Fig. 2.14** Schematic diagram of typical indentation load-depth curve [24].

**Fig. 2.15** Cross section of spherical indenter: contact morphology in the loaded state [24].

**Fig. 2.16.** Schematic drawing of the tensile properties evaluation methodology [76].

**Fig. 2.17** Schematic diagram of residual stress effect on indentation depth at the same indentation load [24].

**Fig. 2.18.** Shift in indentation load-depth curve from tensile and compressive residual stress [80].

**Fig. 2.19** Definitions of conversion factors [80].

**Fig. 2.20** Conversion factors in each orthogonal direction of Knoop indenter [6].

**Fig. 2.21** Ratio of conversion factors with indentation depth [80].

**Fig. 2.22** Schematic illustration of determination of stress directionality using Knoop indenter [80].

**Fig. 2.23** (a) Stress directions of  $0^\circ$ ,  $45^\circ$ ,  $90^\circ$  and  $135^\circ$  and principal stresses and (b) orientations of Knoop indentations perpendicular to stress directions [24].

**Fig. 3.1** Shape of wedge indenter.

**Fig. 3.2** Indent of wedge indenter with (a) 60 degree angle (b) 90 degree angle.



**Fig. 3.3** Specification verification of suggested wedge indenter: (a) included angle (b) edge length.

**Fig. 3.4** Deformation of indenting frame and sample [81].

**Fig. 3.5** Machine compliance of wedge indenter.

**Fig. 3.6** Several indentation tests with smaller indenting depth than that generally used: (a) 1 $\mu$ m (b) 3 $\mu$ m (a) 10 $\mu$ m (a) 20 $\mu$ m.

**Fig. 3.7** Recommended intervals between indents in indentation tests [76].

**Fig. 3.8** Comparison of required testing area for Vickers/Knoop and Knoop indentation models [80].

**Fig. 3.9** Plastic zone size beneath wedge indenter: (a) included angle direction (b) edge length direction

**Fig. 3.10** Considerations for indent size of two wedge indentations.

**Fig. 3.11** Considerations for indent size of four wedge indentations and four Knoop indentations.

**Fig. 3.12** Comparison of indent size of two wedge indentation (red) and two Knoop indentations (blue)

**Fig. 4.1** Schematic indentation load-depth curve from two wedge indentations in the biaxial stress state.

**Fig. 4.2** Definition of conversion factor (a)  $\beta_{\perp}$ , (b)  $\beta_{//}$

**Fig. 4.3** Relationship between applied stresses and load differences [77].

**Fig. 4.4** Subjected area of penetrating wedge indenter.

**Fig. 4.5** Determination of plastic zone size of two directions by finite element analysis.

**Fig. 4.6** Geometrical self-similarity consideration of two directions for reviewing the conversion factor ratio dependency on indentation depth.

**Fig. 4.7** Conversion factor ratio dependency on indentation depth determined from load difference of experiments and FEA [77].

**Fig. 4.8** Conversion factor ratio dependency on indentation depth determined from ratio of plastic zone size.

**Fig. 5.1** Change of Knoop (axisymmetric) hardness of aluminum and steel due to uniaxial stress [78].

**Fig. 5.2** Schematic drawing of wedge indentations: (a) known principal direction (b) unknown principal direction

**Fig. 5.3** Summary of wedge indentations: (a) known principal direction (b) unknown principal direction

**Fig. 6.1** AIS 3000 equipment made by Frontics Inc.

**Fig. 6.2** Schematic drawing and photograph of 10-mm-thick cruciform samples.

**Fig. 6.3** Finite Element Analysis modeling of wedge indentation (a) meshed wedge indenter and specimen (b) deformed shape of specimen in wedge indentation.

**Fig. 6.4** Verification of invariant residual stress sum.

**Fig. 6.5** Verification of principal direction: (a) uniaxial stress state, (b) equibiaxial stress state, (c) nonequibiaxial stress state.

**Fig. 6.6** Verification of principal stress ratio: (a) uniaxial stress state, (b) equibiaxial stress state, (c) nonequibiaxial stress state.

**Fig. 6.7** Verification of principal stress magnitude from uniaxial stress state.

**Fig. 6.8** Verification of principal stress magnitude from equibiaxial stress state.

**Fig. 6.9** Verification of principal stress magnitude from nonequibiaxial stress state.

**Fig. 6.10** Comparison stress magnitude sum between wedge indentation and Vickers indentation.



# Chapter 1

---

---

## Introduction

### *Contents*

1.1. Objective of the Thesis .....	2
1.2. Outline of the Thesis .....	8

## **1.1 Objective of the Thesis**

Many structural materials are subjected to forces or loads when in service. In such situations it is necessary to know the material properties and to design the structures into which it is made in such a way that no excess deformation, let alone fracture, will occur. An important mechanical property for safety and reliability assessment is strength, defined as the resistance to deformation and often assessed by tensile testing. In tensile testing a dogbone-shape specimen is deformed, usually to fracture, with a gradually increasing load that is applied uniaxially along the long axis. This standard method generally requires specific specimen geometry and size. In addition, testing procedures are complex and must be well controlled, thus making mechanical properties evaluation quite difficult; furthermore, it cannot be applied to in-service structures.

Residual stress is able to defined as a stress state that exists in a bulk material without application of an external load (including gravity) or other source of stress, such as a thermal gradient [1, 2]. Residual stress can be generated in materials, components or structures in most steps of materials manufacturing such as rolling, drawing, bending, forging,

pressing, brazing, and welding in component combining process. Also, thermochemical treatments like quenching, ion plating, film deposition, carburizing and nitriding can induce residual stress. As residual stress is also the stress state already present in structures, it can be affected by the operating environment so that environmental operating effects are superposed or cancelled out. Hence the evaluation and management of residual stress is key issue in reliability because it can reduce not only tensile properties like yield strength but also fatigue strength and fracture properties of structures. In additions, in the electronics industry, assessing and maintaining residual stress is significant in preventing failures such as bending, twisting, buckling, and cracking.

Previous research on measuring residual stress falls into two categories: destructive and nondestructive methods. Destructive methods, such as hole-drilling, sectioning, slitting, and layer-removal methods, are based on measuring strains changes before and after stress relaxation through mechanical deformation in the target sample. Because these methods do need on stress-free references, there are relatively few limitations on the target materials, but their practical application is severely limited by their destructive characteristics. On the other hand, methods without specimen destruction, such as X-ray or neutron diffraction,



magnetic Barkhausen noise and ultrasonic method, can assess the difference in physical parameters between residual stressed and stress-free specimen. The drawback of these techniques is the need to keep the specimen in a stress-free state. In addition, the results often show poor reproducibility and greater scatter than mechanical relaxation methods, because interpreting the signal and separating out residual stress effects, microstructural factors and environmental noise are very difficult.

Instrumented indentation testing, which developed from conventional hardness testing, differs greatly from these other techniques in that it measures the indenting load and depth continuously and simultaneously. Also, the test procedure is relatively simple, as observing the residual impression area is not necessary, it can be operated with a portable apparatus for in-field nondestructive applications such as pipes, vessels, or any structure in plants, vehicles, airplanes, etc. In addition, micro- and nano-scale applications as in thin films, electronics modules and components are simple to perform.

Many studies have sought to evaluate residual stress with IIT. Suresh and Giannakopoulos proposed a theoretical model using a sharp indenter to assess the equi-biaxial stress based on residual-stress-independent parameter, contact area. Thus they set up their model from the

ratio of the true contact area of stressed and stress-free samples in terms of residual stress and contact hardness [3].

Lee et al. [4,5] suggested a modified sharp indentation model that extracts a plastic-deformation-correlated deviatoric stress component in tensor form. Han et al. [6] tried to obtain the information on stress ratio,  $p$ , using a twofold-symmetric indenter, the Knoop indenter. This indenter defines two included angles, the ratio of major and minor axes of an indent is 7.11:1 [7], and has been used to assess material anisotropy by its directional hardness [8-23]. Han's model was given in terms of the load differences of two Knoop indentations at two orthogonal axes along the principal directions; the ratio of conversion factors, which are linear slope to uniaxial residual stress with load differences from two Knoop indentations operated at a  $90^\circ$  interval. This ratio is experimentally taken as 0.34 and was validated from two indentation tests on specimens with various stress ratios. Choi et al. [24] proposed using two sets of two indentations each at  $45^\circ$  degree intervals for specimens whose principal directions are unknown. From these four load differences along the  $0^\circ$ ,  $45^\circ$ ,  $90^\circ$ , and  $135^\circ$  directions, the residual stress directionality (principal direction and ratio) can be deduced in terms of two sets of load differences. However, previous research found that several indentations with two kinds

of indenters, Vickers and Knoop indenters, are required. Since changing indenters in the field is inconvenient, a method for evaluating residual stress, including its magnitude, with only Knoop indenter is researched.

The objective of the current study is to develop a residual stress assessment method using a smaller indent. A new model for evaluating residual stress magnitude and directionality was suggested with novel indenter shape, a wedge. A wedge indenter, consisting of a included angle and edge length, was chosen after considering the decrease in the amount of indent size along its edge, and the experimental ease of using the included angle. To obtain a conversion factor ratio for a wedge indenter, two indentation tests are conducted orthogonally on specimens in a uniaxial stress state. In addition, FEA simulations were run with wedge-shape indenters and stressed samples to obtain a conversion factor and investigate the physical meaning of the conversion factor ratio. The conversion factor ratio for the suggested wedge indenter was found to be 0.463 and the FEA verification was performed. The model for residual stress magnitude assessment was set up with the sum of conversion factors at 100  $\mu\text{m}$  indentation depth, as the conversion factors and its ratio are depth-dependent parameters in wedge indentation. The previous Knoop indentation model for residual stress directionality was modified and

experimentally verified for 15 combinations of stress states and material specimens using a stress-generating jig, and the results were compared with previous Vickers indentation models for stress magnitude assessment.

## **1.2 Outline of the Thesis**

This thesis has seven chapters. The objective and outline of thesis are briefly introduced in Chapter 1. Research background about definition, origin, and measurement methods of residual stress, the introduction of instrumented indentation tests, and previous research of residual stress assessment with IIT was described in Chapter 2. The origin of instrumented indentation tests and the basic concept of its use to evaluate various mechanical properties, as well as giving an historical overview of residual stress evaluations using instrumented indentation test are also included in Chapter 2. Chapter 3 discusses the experimental conditions, for example, shape of novel suggested indenter, compliance and zero index of machine, and the consideration on indent interval. In Chapter 4, the conversion factor which is relating parameters between uniaxial residual stress and load difference according to indenting direction is determined by experiments and finite element analysis. The approach for physical meaning of conversion factor ratio are supplement in Chapter4. The theoretical modeling for the magnitude and directionality evaluation of surface residual stress with wedge indentation test are described in Chapter

5. Experimentally verification work of the suggested model with stress generating jig and the results comparison of wedge indentation model and previous Vickers indentation model are contained in Chapter 6. Finally, Chapter 7 summarizes and concludes the findings of this study.



# Chapter 2

---

---

## Research Background

### *Contents*

2.1	Definition of Residual Stress .....	12
2.1.1	Residual Stress on Weldment .....	14
2.1.2	Residual Stress on Thin Film .....	16
2.2	Measurement of Residual Stress .....	17
2.2.1	Destructive Methods .....	17
2.2.2	Non-destructive Methods .....	21
2.3	Instrumented Indentation Test .....	24
2.3.1	Basic Properties .....	26
2.3.2	Advanced Properties .....	30
2.4	Evaluation of Residual Stress using indentation .....	37
2.4.1	Vickers Indentation Model .....	37
2.4.2	Knoop Indentation Model .....	39
2.5	Limitations of Previous Methods .....	48



## **2.1. Definition of Residual Stress**

Residual stresses are stress fields that exist without any external load. All mechanical processes can induce elastic/plastic deformations that may create to residual stresses [26]. A thermal gradient caused by nonuniform heating or cooling [26, 2], incompatibilities from plastic deformation, discontinuity in deformation under temperature changes produced by mismatched thermal expansion coefficients, or self-equilibrating internal sources of stresses in a free body without external force or constraints on its boundary may all produce residual stress [27]. In addition, residual stress can be caused during manufacturing processes such as welding, brazing, cladding and thin film processing, or during heat or thermochemical treatments like quenching, carburizing, nitriding and ion plating [26, 2]. Thus, the residual stress state depends on both prior processing and material properties arising from the current mechanical processing or the environment. As these residual stresses can induce various unexpected failures, cracks, fractures, and distortion, their measurement and analysis are important.

A thermal switch that uses residual stresses to produce desired

movements is illustrated in Fig. 2.1. The switch consists of two layers that have different thermal expansion coefficients  $\alpha_1$  and  $\alpha_2$  but the same length at room temperature. When  $\alpha_1$  is larger than  $\alpha_2$ , as the temperature increases  $\Delta T$  will make layer 1 expand more than layer 2. However, the bonding between the two layers keeps layer 1 from expanding freely. In this case, a tension state is induced in layer 2 and a compression state is in layer 1. The two features are interrelated: any tension or compression is always balanced and the stress in the region restricted from expansion is compressive and vice versa [26].

### 2.1.1 Residual Stress in Weldments

Welding is a process of joining metal by applying heat or heat combined with pressure and adding a filler material. When the two base metals are melted, a filler material is typically added to the joint to form a weld pool and they are quenched together. In this process, the thermal coefficient difference between the base metals and the filler introduces residual stresses of various directions and magnitude. A non-uniform heating gradient causes changes in the expansion and shrinkage of each part of the base metals, and these deformations are expressed by thermal strain from solidification of the melted part. In addition, this thermal stress is accompanied by a phase transformation in the metals due to the welding processes.

Welding residual stress has two parts: in-plane residual stress, which is parallel or perpendicular to the welding line, and out-of-plane residual stress, the through-thickness residual stress generated during thick plate welding. The in-plane residual stresses are a longitudinal residual stress and transverse residual stress and are shown as  $\sigma_x$ ,  $\sigma_y$  respectively in the schematic diagram in Fig.2.2.

Fig. 2.3. details the generation of welding residual stress along the welding line. There are no temperature distribution in the section [A-A], so residual stress is not present. In the section [B-B], a large temperature distribution is induced by the melted pool located in the center, and lower residual stress exists in the center because there are no mechanical constraints. As the temperature distribution in section [C-C] decreases, the filler material and adjacent base metals are cooling and shrinking. During this stage, tensile residual stress is generated in the center and compressive residual stress appears around the center to balance the equilibrium state. There is no temperature distribution in section [D-D], and the magnitude of residual stress is increased by completion of cooling stage: we see a residual stress distribution similar to that in section [C-C].

### **2.1.2 Residual Stress on Thin Film**

Residual stress in thin films leads to bending, twisting, buckling, or cracking, and is one of the main factors in film failure (Fig.2.4). Residual stress in thin films is of three types: thermal stress, intrinsic stress, and epitaxial stress (see Fig. 2.5) [29-31]. The thermal stress is introduced by the difference in thermal expansion coefficient between the thin film and is created in the deposition process or in the in-service environment. The intrinsic stress is defined as a self-generated stress during film growth. Microstructural changes such as grain boundaries, dislocations, vacancies, impurities, and secondary phases or phase transformations cause changes in density changes, and elastic strain and stress are induced to maintain coherency between substrate and volume. Epitaxial stress is generated by the coherency of substrate and film that have similar atomic constants. Generally, intrinsic stress is observed as a compressive state at the top and bottom and tensile state at center through-thickness direction and is called CTC behavior [31-38]. Fig. 2.6 shows a schematic illustration of CTC behavior.

## 2.2 Measurement of Residual Stress

### 2.2.1 Destructive Methods

#### 2.2.1.1 Hole-drilling Method

The hole-drilling method is a conventional method based on measuring the strain difference between the original surface and a stress-relaxed region after a small hole is drilled. A strain gauge rosette attached on the specimen surface, detects relaxed strain in the three directions around the hole (Fig.2.7). The principal residual stress and direction can be determined from:

$$\sigma_{res}^{max} = \frac{\varepsilon_1 + \varepsilon_3}{4A} + \frac{1}{4B} \sqrt{(\varepsilon_3 - \varepsilon_1)^2 + (\varepsilon_3 + \varepsilon_1 - 2\varepsilon_2)^2} \quad (2-1)$$

$$\sigma_{res}^{min} = \frac{\varepsilon_1 + \varepsilon_3}{4A} - \frac{1}{4B} \sqrt{(\varepsilon_3 - \varepsilon_1)^2 + (\varepsilon_3 + \varepsilon_1 - 2\varepsilon_2)^2} \quad (2-2)$$

$\varepsilon_1$ ,  $\varepsilon_2$  and  $\varepsilon_3$  are the strain values measured in the three directions, and

A and B are constants correlated with the elastic properties of target specimens.

This method has two limitations. The first is that it is destructive and accompanied by plastic deformation caused by the hole-drilling. This plastic deformation around the hole disturbs the relaxation of residual stress and may induce additional deformation near the strain gauge. The second limitation is its dependency on the operator's skill. For these reasons, the accuracy and repeatability of residual stress measurements can be poor.

#### 2.2.1.2 Sectioning Method

The sectioning method is mainly used for non-uniform residual stress evaluation in welded specimens (Fig. 2.8). Many strain gauges are attached perpendicular to the specimen cutting line and then the values of the strains relieved by cutting the part of specimen are measured. The in-plane biaxial residual stress in each direction is calculated by Eq. (2-3) and Eq. (2-4) using these measured relieved strains:

$$\sigma_{res}^x = \frac{E}{(1-\nu^2)} (\varepsilon_x + \nu \varepsilon_y) \quad (2-3)$$

$$\sigma_{res}^y = \frac{E}{(1-\nu^2)} (\varepsilon_y + \nu \varepsilon_x) \quad (2-4)$$

The quantitative residual stress is affected by the distance between the strain gauges and the cutting region, but the results can be used to estimate the relative distribution of residual stresses.

Nowadays, the deformation due to each sectioning is recorded and later used in a three-dimensional (3D) finite element analysis (FEA) to obtain the residual stress [26]. This method also called the contour method and based on solid mechanics, determines residual stress by carefully cutting a specimen into two pieces and measuring the resulting deformation due to residual stress redistribution (Fig. 2.9) [39].

#### 2.2.1.3. Slitting Method

The slitting method uses a cut of progressively increasing depth to relax the residual stress on a given plane during the deformation is recorded



(Fig.2.10). It is a more rapid method than sectioning and layer removing and can be applied in both the near-surface and through- thickness direction. This method was developed in order to obtain the distribution of residual normal stresses in one or more planes of interest. [26]

## 2.2.2 Non-destructive Methods

### 2.2.2.1 Curvature Method

The curvature method is a fundamental method for measuring residual stress in thin films [40]. The curvature of the substrate is evaluated by laser, optical interferometry or another method and the residual stress is evaluated from the Stoney equation (Eq. 2-5) using this curvature value (Fig. 2.11).

$$\sigma_f = \left( \frac{E}{1-\nu} \right)_s \frac{t_s^2}{6t_f} \left( \frac{1}{R_2} - \frac{1}{R_1} \right) \quad (2-5)$$

The limitation of this method is that it measures only an average residual stress: it cannot evaluate the residual stress in local area.

### 2.2.2.2 X-ray Diffraction Method

The X-ray diffraction method for measuring residual stress is based on the lattice spacing and diffraction angle (Fig. 2.12). The residual strain is expressed by Eq. (2-6) using the lattice spacing measured in the stressed state  $d$  and that measured in the stress-free state  $d_0$ :

$$\frac{d_{\psi,\phi} - d_0}{d_0} = \frac{1}{E} [\sigma_\phi (1 + \nu) \sin^2 \psi] \quad (2-6)$$

This method can be used only for specimens with regular crystalline structure, and the result can be easily affected by microstructural factors.

#### 2.2.2.3 Magnetic Barkhausen Noise Method

The magnetic Barkhausen noise method measures the change in the noise signal in ferromagnetic materials caused by an external magnetic field. Residual stress can change materials' magnetic properties. The results of this method are shown as a deviation from a reference stress level in a master curve. However, this method has the limitations that it can be applied only to ferromagnetic materials and that it is difficult to determine

master curves for such complex microstructures as weldments.

#### 2.2.2.4 Ultrasonic Method

The velocity of ultrasonic waves as they propagate through a medium (solid or liquid) is related to the elastic property of the medium. As residual stress can influence the ultrasonic wave velocity, this method can evaluate residual stress effects. It easily detects longitudinal and circumferential stress, but it cannot evaluate local residual-stress distributions, since its results are averaged over the distance traveled by the ultrasonic wave. Also, it has the limitation that it is not easy to separate the effect of residual stress from environmentally detected noise.

## **2.3 Instrumented Indentation Test**

Instrumented indentation testing (IIT) has been developed from conventional hardness testing, which simultaneously records indentation load and penetration depth. The greatest difference between indentation testing and conventional hardness testing is that in IIT it not necessity to measure the indent after unloading. Instead, the elastic modulus and hardness are obtained by analyzing the indentation load-depth curve. The theory and technique of IIT have been extended to nondestructive evaluation of other advanced properties such as tensile properties, fracture toughness, fatigue properties, interfacial adhesion properties and residual stress (Fig. 2.12). As mentioned above, the significant characteristic of IIT is its simple and in-field, in-situ methodology. In addition, it does not require any particular specimen shape. To extend its availability, standards for IIT have been established for hardness/material parameter and residual stress measurement, including methods of verification and testing machine calibration [41-44].

IIT can yield some of the material properties and characteristics from tensile tests by analyzing the indentation load-depth curve and taking

into account the stress field beneath a spherical indenter. By converting the indentation load-depth curve to a stress-strain curve, a defined representation, tensile properties such as yield and ultimate tensile strength, elastic modulus and strain-hardening exponent can be obtained. Ductile/brittle models have also been developed for estimating fracture behavior by considering the fracture criterion from mechanical properties. Both models take the indentation fracture energy as matching to the fracture energy required for crack extension. In addition, methods for evaluating residual stress have been established based on a stress-invariant contact hardness model.

### 2.3.1 Basic Properties

IIT has been generally used to obtain elastic modulus and hardness in local region from indentation load and depth [45, 46]. Indentation load and depth are recorded in real time during a test. After the load is completely unloaded by indenter, the material deformation has two parts: elastic recovery and permanent deformation. As the unloading curve depends only on the elastic properties, it can determine the stiffness and elastic modulus. Fig. 2.13 is a schematic illustration of an indentation load-depth curve, where the parameter  $L$  designates the load and  $h$  the displacement relative to the initial un-deformed surface. Three important quantities can be measured from the  $L$ - $h$  curves: the maximum load ( $L_{max}$ ), the maximum displacement ( $h_{max}$ ), and the elastic unloading stiffness ( $S$ ), also called the contact stiffness and defined as the initial slope of the unloading curve. Experimentally accurate sensing of these parameters is important because it relates directly to the accuracy of the hardness and elastic modulus. The final depth  $h_f$ , which is the permanent depth of penetration after full unloading, is also significant. The contact stiffness can be expressed by:

$$S = \left. \frac{dL}{dh} \right|_{h=h_{max}} \quad (2-7)$$

Determination of the accurate contact depth is a significant step in evaluating elastic modulus and hardness, as it is the dominant factor. Materials show elastic deflection and plastic pile-up/sink-in. With contact mechanics [46], Oliver and Pharr expressed the elastic deflection,  $h_d$ , as

$$h_d = \varepsilon \frac{L_{max}}{S} \quad (2-8)$$

where  $\varepsilon$  is a constant depending on indenter geometry. The constants are  $\varepsilon = 0.72$  for conical indenters,  $\varepsilon = 0.75$  for parabolic indenters including Vickers and Berkovich indenter (which approximates to a sphere at small depths) and  $\varepsilon = 1.00$  for flat punches [45].

Much research on plastic pile-up/sink-in behavior has been performed to find the relationship between indentation behavior and parameters. The plastic pile-up behavior is expressed by the work-hardening exponent and



the ratio of maximum indentation depth and to indenter radius [47-57]:

$$h_{pile} = f\left(n, \frac{h_{max}}{R}\right) \quad (2-9)$$

where,  $h_{pile}$  is the plastic pile-up height from the undeformed surface. Using Eq. (2-9) to approximate the vertical displacement of the adjacent region of contact, the contact depth ( $h_c$ ) is (Fig. 2.14).

$$h_c = h_{max} - h_d + h_{pile} \quad (2-10)$$

From the contact depth, the area of the contact  $A_c$  can be worked out and the hardness and elastic modulus evaluated from the indenter geometry. The area function must be carefully calibrated and deviations from non-ideal indenter geometry must be taken into account. For a spherical indenter, the relation between the contact area  $A_c$  and the contact depth  $h_c$  is:

$$A_c = \pi(2Rh_c - h_c^2) \quad (2-11)$$

For sharp indenters such as Vickers or Berkovich indenters, the relation is:

$$A_c = 24.5h_c^2 \quad (2-12)$$

Finally, the hardness and elastic modulus are calculated in Eq. (2-13) and Eq. (2-14)

$$H = \frac{L_{\max}}{A_c} \quad (2-13)$$

$$E_r = \frac{\sqrt{\pi}}{2} \frac{S}{\sqrt{A_c}} \quad (2-14)$$

## 2.3.2 Advanced Properties

### 2.3.2.1 Tensile Properties

In order to determine mechanical properties, the plastic behavior, that is the plastic pile-up/sink-in, at the indent must be considered. Kim et al. [58] proposed a relationship between the heights of plastic pile-up ( $h_{pile}$ ) divided by the contact depth ( $h_c$ ) and the work-hardening exponent  $n$  and the ratio of penetration depth  $h_{max}$  and indenter radius  $R$ ,  $h_{max}/R$ . Using linear regression to obtain data, they expressed the plastic behavior of materials as:

$$\frac{h_{pile}}{h_c} = f\left(n, \frac{h_{max}}{R}\right) \quad (2-15)$$

Tabor's research [59] proposed a representative stress with indentation load as the relation between mean pressure (indentation load normalized by contact area) and representative stress:

$$\sigma = \frac{P_m}{\psi} = \frac{1}{\psi} \frac{L}{\pi a_c} \quad (2-16)$$

where  $\psi$  is a plastic constraint factor that correlates the stress state in a uniaxial tensile specimen and triaxial stress state beneath a spherical indenter,  $a_c$  is the contact radius and  $L$  is the load. Jeon et al. [59] used from 38 experimental and simulated materials to derive the value  $\psi=3$ , which covers most metallic materials. Ahn et al. [60], studying the representative strain under a spherical indenter using a tangential function, express representative strain as:

$$\varepsilon = \left( \frac{\alpha}{\sqrt{1 - (a_c / R)^2}} \right) \left( \frac{a_c}{R} \right) = \alpha \tan \gamma \quad (2-17)$$

where  $\alpha$  is a proportional constant equal to 0.14 determined by finite element analysis and is independent of material. From indentation testing

with several loading-unloading curves, fifteen points of representative stress and strain are obtained. A constitutive equation is used to describe the tensile curve from each representative stress-strain point. There are two options for hardening behavior, Holloman-type, and linear-hardening type [61]:

$$\sigma = K\varepsilon^n \quad (2-18)$$

$$\sigma = A + E\varepsilon \quad (2-19)$$

From these constitutive equations, the yield strength is determined through the 0.2% offset method, and ultimate tensile strength is calculated from representative strain and the corresponding work-hardening exponent based on instability in tension. Fig. 2.15 summarizes the method for evaluating tensile properties using spherical indentation.

#### 2.3.2.2 Residual Stress

The indentation load-depth curve can be shifted by the magnitude and direction of residual stress (Fig. 2.16). Work based on evaluating residual stress from changes in contact morphology during indentation shows that hardness and elastic modulus are invariant properties, independent of residual stress [1, 62-63].

Tsui et al. [62] used IIT to look for a relationship between the applied stress state and such mechanical properties as conventional hardness, indentation hardness, elastic modulus and stiffness: they found that conventional hardness, elastic modulus and stiffness were invariant. Bolshakov et al. [63] did similar work using Finite Element Analysis to establish the exact indentation contact area. Suresh et al. [3] first developed a theoretical model for estimating surface average residual stress by measuring the apparent contact area during instrumented sharp indentation. Swadener et al. [64] suggested a residual stress measurement method with spherical indentation test for improved residual stress sensitivity. Giannakopoulos [65] analyzed analytically and experimentally the effect of the initial surface stresses on the load-depth response in instrumented sharp indentation. And Lee et al. [5] and Jang et al. [66], using tensor analysis of the stress beneath the indenter for the same purpose, linked the  $zz$ -direction deviatoric stress component to the indentation load. Since a

stress-induced normal load difference  $L_0 - L_S$  affects only z-direction deviatoric stress, a relation between load difference and residual stress is found. Lee et al. [5, 67] looked at evaluating residual stress directionality in specimens in nonequibiaxial residual stress states by observing the contact morphology. Han et al. [6] and Choi et al. [68], working on evaluating stress directionality by instrumented Knoop indentation testing, found a relationship between uniaxial residual stress and load difference that they called it a conversion factor. By performing instrumented Knoop indentation tests twice in the principal direction, they created a model for biaxial residual stress directionality with a conversion factor ratio.

Kim et al. [69] studied estimating principal direction and stress directionality by performing instrumented Knoop indentation testing four times and related the physical meaning of the conversion factor ratio to the size of the plastic zone beneath the indenter. Kim et al. [70] recently developed to establish a method to evaluate biaxial residual stress magnitude, directionality, and principal direction using only instrumented Knoop indentation testing.

#### 2.3.2.3 Fracture Properties

Previous research has used the indentation cracking method to evaluate fracture toughness in brittle materials such as ceramics. Estimating fracture toughness for brittle material involves a crack that occurs in the indenter contact and is the main factor in characterizing the fracture toughness. In ductile materials such as metals, however, cracking does not occur during indentation. Many researchers have tried to estimate the fracture toughness of metals, using a criterion that matches the critical fracture point to indentation parameters, and many models such as critical fracture stress [71], critical fracture strain [72], and critical void volume fraction [73] have been developed.

Nevertheless, it still remains possible that the fracture toughness of ductile materials can be estimated from instrumented indentation tests. Previous research [73] has characterized the stress state ahead of the crack tip and spherical indenter tip by finite element analysis and shown that the stress concentration generated by indentation with a spherical indenter is similar to that ahead of a crack tip. The result means that the material under spherical indenter is highly constrained by surrounding elastic material and that the constraint effect at a certain indentation depth is similar to that in front of a sharp notch. Even though indentation of a ductile material to a certain critical depth is sufficient to initiate a crack, the high constraint



effect might suppress crack formation. Hence, fracture toughness can be predicted by determining a critical indentation depth corresponding to the onset of unstable crack extension. Using an energy approach, the energy required for fracture initiation can be expressed as the ratio of the indentation deformation energy absorbed per unit area to the critical indentation depth.

Lee et al. [74] developed a simple and realistic approach to estimating fracture toughness in metallic materials. The concepts of the critical fracture stress and critical fracture strain are applied to set up a fracture toughness model using IIT for relatively brittle and ductile metallic materials. For brittle fracture it was assumed that cleavage fracture takes place when the local tensile stress exceeds a critical value that was expressed in terms of a yielding condition. In contrast, the ductile fracture model was deduced by linking the local strain to the fracture strain in tension tests as determined from material properties measured by IIT. Each fracture criterion is then used to determine the indentation fracture energy corresponding to the fracture energy required for crack extension.

## 2.4 Evaluation of Residual Stress using indentation

### 2.4.1 Vickers indentation model

Residual stress is evaluated by finding the difference in load to indent a stress-free and a stressed specimen. If the specimen is in a tensile or compressive residual stress state, the indentation load-depth curve shifts upward or downward (Fig. 2.17). Tensile residual stress adds to the indentation load, since the indenter can penetrate the material more easily than in the stress-free state, and compressive residual stress decreases the indentation load.

To analyze the relation between the quantitative amount of residual stress and the load difference, Lee et al.[5] tried to calculate the equi-biaxial residual stress by the biaxial residual stress and to correlate  $L_{res}$  with  $-2\sigma_{res}/3(\sigma_r^D)$  from the deviatoric stress.

A mathematical tensor decomposition was performed:

$$\begin{aligned}
& \text{Biaxial stress} \\
& \overbrace{\begin{pmatrix} \sigma_{res,x} & 0 & 0 \\ 0 & \sigma_{res,y} & 0 \\ 0 & 0 & 0 \end{pmatrix}} = \overbrace{\begin{pmatrix} \sigma_{res,x} & 0 & 0 \\ 0 & p\sigma_{res,x} & 0 \\ 0 & 0 & 0 \end{pmatrix}} = \\
& \underbrace{\begin{pmatrix} \frac{(1+p)}{3}\sigma_{res,x} & 0 & 0 \\ 0 & \frac{(1+p)}{3}\sigma_{res,x} & 0 \\ 0 & 0 & \frac{(1+p)}{3}\sigma_{res,x} \end{pmatrix}}_{\text{Hydrostatic stress}} + \underbrace{\begin{pmatrix} \frac{(2-p)}{3}\sigma_{res,x} & 0 & 0 \\ 0 & \frac{(2-p)}{3}\sigma_{res,x} & 0 \\ 0 & 0 & -\frac{(1+p)}{3}\sigma_{res,x} \end{pmatrix}}_{\text{Deviatoric stress}} \quad (2-20)
\end{aligned}$$

If the stress ratio  $p$ , which is the ratio of residual stress at the x, y-axis and the z-axis direction (indenting direction) component of the deviatoric stress tensor is pre-informed, each residual stress is expressed as:

$$\sigma_{res,x} = \frac{3(L_0 - L_T)}{(1+p) \cdot A_c^T} \quad (2-21)$$

$$\sigma_{res,y} = p\sigma_{res,x} = \frac{3p(L_0 - L_T)}{(1+p) \cdot A_c^T} \quad (2-22)$$

## 2.4.2 Knoop indentation model

### 2.4.1.1 Determination of residual stress ratio

It is not possible to evaluate non-equibiaxial stress stress using Vickers indentation because the Vickers indenter has fourfold symmetry. Knoop indentation was suggested because the Knoop indenter has twofold symmetry, so that it can establish a stress difference from two indentations at a 90° interval. It is assumed that residual stress and load difference at the same depth from Knoop indentation have a linear relationship. The Knoop indenter has a 7.11:1 ratio of long and short indent diagonals and causes different load differences in the load-depth curve according to the penetration direction. For quantitative evaluation, a relation between the load difference and residual stress in each direction is introduced:

$$\Delta L_1 = \alpha_{\perp} \sigma_{res}^x + \alpha_{\parallel} \sigma_{res}^y \quad (2-23)$$

$$\Delta L_2 = \alpha_{\parallel} \sigma_{res}^x + \alpha_{\perp} \sigma_{res}^y \quad (2-24)$$

Here  $\alpha_{\perp}$  and  $\alpha_{//}$  are correlation factors between the residual stress and the indentation load difference, as shown in Fig. 2.18, and are depth-dependent variables. Han et al. [6] experimentally obtained conversion factors for each direction with a Knoop indenter (Fig. 2-19); they found the relationship between the ratio of load difference of each directions and

the stress ratio ( $p = \frac{\sigma_{res}^y}{\sigma_{res}^x}$ ) to be:

$$\frac{\Delta L_2}{\Delta L_1} = \frac{\frac{\alpha_{//}}{\alpha_{\perp}} + \frac{\sigma_{res}^y}{\sigma_{res}^x}}{1 + \frac{\alpha_{//}}{\alpha_{\perp}} \frac{\sigma_{res}^y}{\sigma_{res}^x}} = \frac{\frac{\alpha_{//}}{\alpha_{\perp}} + p}{1 + \frac{\alpha_{//}}{\alpha_{\perp}} p} \quad (2-25)$$

where  $\alpha_{//} / \alpha_{\perp}$  is a predetermined conversion factor ratio of value 0.34.

The load difference ratio is a function of stress directionality and the conversion factor ratio; the conversion factor is derived experimentally as 0.34. Their experiments showed that the ratio is not dependent on depth (Fig. 2.20).

As the load difference ( $\Delta L_1$ ,  $\Delta L_2$ ) in Eq. (2-25) is easily retained by two

Knoop indentations at 90° intervals (Fig. 2.21) and the conversion factor ratio is predetermined independent of materials, indentation depth, and residual stress state, the stress ratio,  $p$ , can be obtained.

By combining two kinds of indentation testing, Knoop indentation and Vickers indentation, the surface residual stress can be obtained. In particular, we can deduce the axial residual stress and hoop residual stress in weldments, and we can also perform local stress mapping near the weld.

#### 2.4.1.2 Determination of principal direction

The basic concept of evaluating the principal direction by Knoop indentation [69] starts from determination of residual stress ratio. Two Knoop indentations are made at 45° intervals from two previous Knoop indentations. In other words, four Knoop indentation tests are made along the 0°, 45°, 90° and 135° directions (see Fig. 2.22). The 0° is indentation is located randomly and the 45°, 90° and 135° directions are also determined. The residual stresses in each direction are defined as  $\sigma_{res}^0$ ,  $\sigma_{res}^{45}$ ,  $\sigma_{res}^{90}$  and  $\sigma_{res}^{135}$ . Knoop indenter is related by the perpendicular residual stress to the orientation of the long diagonal of Knoop indenter. Hence load

differences obtained from four Knoop indentations along the preselected directions are also determined as  $\Delta L_0$ ,  $\Delta L_{45}$ ,  $\Delta L_{90}$  and  $\Delta L_{135}$ . That is,  $\sigma_{res}^0$  affects  $\Delta L_0$  and  $\sigma_{res}^{45}$  is related to  $\Delta L_{45}$ .

From two sets of Knoop indentations at  $90^\circ$  intervals, the values of the two stress directionality are measured from the load differences using Eq. (2-25).  $p'$  and  $p''$  are defined as the stress ratios between  $\sigma_{res}^0$ ,

$\sigma_{res}^{90}$ , and  $\sigma_{res}^{45}$ ,  $\sigma_{res}^{135}$ .

$$p' = \frac{\sigma_{res}^{90}}{\sigma_{res}^0} = \frac{\frac{\Delta L_0}{\alpha_{//}} - \frac{\alpha_{//}}{\alpha_{\perp}}}{1 - \frac{\alpha_{//}}{\alpha_{\perp}} \frac{\Delta L_0}{\Delta L_{90}}} \quad (2-26)$$

$$p'' = \frac{\sigma_{res}^{135}}{\sigma_{res}^{45}} = \frac{\frac{\Delta L_{45}}{\alpha_{//}} - \frac{\alpha_{//}}{\alpha_{\perp}}}{1 - \frac{\alpha_{//}}{\alpha_{\perp}} \frac{\Delta L_{45}}{\Delta L_{135}}} \quad (2-27)$$

From the plane stress transformation,  $\sigma_\theta$  and  $\theta_\rho$  are determined by

rotation of the stress direction using Eqs. (2-28) and (2-29) [69]:

$$\sigma_{\theta} = \frac{\sigma_{res}^0 + \sigma_{res}^{90}}{2} + \frac{\sigma_{res}^0 - \sigma_{res}^{90}}{2} \cos 2\theta + \tau_{xy} \sin 2\theta \quad (2-28)$$

$$\tan 2\theta_p = \frac{2\tau_{xy}}{\sigma_{res}^0 - \sigma_{res}^{90}} \quad (2-29)$$

By combining Eq. (2-26), Eq. (2-27), Eq. (2-28), Eq. (2-29), the principal direction  $\theta_p$  and ratio of principal residual stresses  $P$  can be expressed as:

$$\tan 2\theta_p = \frac{(1 + p')(1 - p'')}{(1 - p')(1 + p'')} \quad (2-30)$$

$$P = \frac{\sigma_2}{\sigma_1} = \frac{(1 + p')\cos 2\theta_p - (1 - p')}{(1 + p')\cos 2\theta_p + (1 - p')} \quad (2-31)$$

Kim et al. [70] recently established a way to evaluate biaxial residual stress magnitude, directionality, and principal direction using only instrumented Knoop indentation testing. The sum of the conversion factors can be



derived by comparing previous Vickers and Knoop indentation models. By substituting  $p$  into the Vickers indentation model (Eq. (2-21), and Eq. (2-22)), the sum of the surface residual stresses is determined as:

$$\sigma_{res}^x + \sigma_{res}^y = \frac{3}{\psi} \frac{1}{A_c} \Delta L \quad (2-32)$$

From the Knoop indentation model, Eq. (2-21) is converted to:

$$\sigma_{res}^x + \sigma_{res}^y = \frac{1}{\alpha_{\perp} + \alpha_{//}} (\Delta L_1 + \Delta L_2) \quad (2-33)$$

As the left-hand sides of Eqs. (2-30) and (2-31) are the same, the right-hand sides of Eqs. (2-30) and (2-31) are also equal:

$$\frac{3}{\psi} \frac{1}{A_c} \Delta L = \frac{1}{\alpha_{\perp} + \alpha_{//}} (\Delta L_1 + \Delta L_2) \quad (2-34)$$

Assuming that the Knoop indenter is equivalent to the sum of Vickers indenters, the load difference  $\Delta L$  is substituted into the sum of directional load differences for the Knoop indenter,  $\Delta L_1 + \Delta L_2$ . Eq. (2-34) can be converted to a sum of conversion factors as:

$$\alpha_{\perp} + \alpha_{//} = \frac{\psi}{3} A_c \quad (2-35)$$

where  $\Psi$  is a plastic constraint factor. Since  $\Psi$  can be taken as a constant equal to 3 in common metallic materials, the sum of the conversion factors  $\alpha_{\perp} + \alpha_{//}$  is theoretically equivalent to the contact area of the Knoop indentation, and the ratio of conversion factors  $\alpha_{//} / \alpha_{\perp}$  is 0.34 from previous Knoop indentation models [6]. As the two sums and ratios of two conversion factors are obtained, each conversion factor is calculated. For a known principal axis of residual stress and two Knoop indentations in each principal direction, the principal residual stress can be expressed as:

$$\begin{pmatrix} \Delta L_1 \\ \Delta L_2 \end{pmatrix} = \begin{pmatrix} \alpha_{\perp} & \alpha_{//} \\ \alpha_{//} & \alpha_{\perp} \end{pmatrix} \begin{pmatrix} \sigma_{res}^x \\ \sigma_{res}^y \end{pmatrix} \quad (2-36)$$

where  $\Delta L_1$  and  $\Delta L_2$  are load differences from the two Knoop indentations according to principal direction.  $\sigma_{res}^x$ ,  $\sigma_{res}^y$  can be expressed by rearrangement as:

$$\sigma_{res}^x = \frac{\Delta L_1 - \frac{\alpha_{//}}{\alpha_{\perp}} \Delta L_2}{\left(1 - \frac{\alpha_{//}}{\alpha_{\perp}}\right)(\alpha_{\perp} + \alpha_{//})} \quad (2-37)$$

$$\sigma_{res}^y = \frac{\Delta L_2 - \frac{\alpha_{//}}{\alpha_{\perp}} \Delta L_1}{\left(1 - \frac{\alpha_{//}}{\alpha_{\perp}}\right)(\alpha_{\perp} + \alpha_{//})} \quad (2-38)$$

As the ratio and sum of conversion factors are replaced by  $k$  and  $A_c$ , Eq.

(2-37) and Eq. (2-38) reduce to:

$$\sigma_{res}^x = \frac{3}{\psi} \frac{1}{A_c} \frac{k\Delta L_1 - \Delta L_2}{k - 1} \quad (2-39)$$

$$\sigma_{res}^y = \frac{3}{\psi} \frac{1}{A_c} \frac{k\Delta L_2 - \Delta L_1}{k - 1} \quad (2-40)$$

If there is no information on the principal direction, it is calculated from

Eq. (2-41):

$$\tan 2\theta_p = -\frac{\Delta L_3 - \Delta L_4}{\Delta L_1 - \Delta L_2} \quad (2-41)$$

The principal residual stresses  $\sigma_I$  and  $\sigma_{II}$  are then:

$$\sigma_I = \frac{3}{\psi} \frac{1}{2A_c} \left\{ (\Delta L_1 + \Delta L_2) + \frac{k+1}{k-1} \frac{\Delta L_1 - \Delta L_2}{\cos 2\theta_p} \right\} \quad (2-42)$$

$$\sigma_{II} = \frac{3}{\psi} \frac{1}{2A_c} \left\{ (\Delta L_1 + \Delta L_2) - \frac{k+1}{k-1} \frac{\Delta L_1 - \Delta L_2}{\cos 2\theta_p} \right\} \quad (2-43)$$

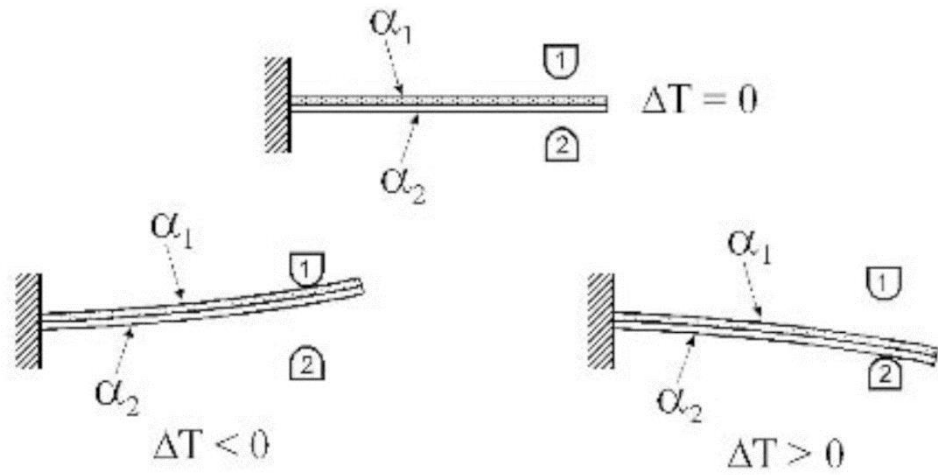
Compared to previous research using both Vickers and Knoop indenters, four Knoop indentations and contact areas for the Knoop indenter are needed.

## 2.5 Limitations of Previous Methods

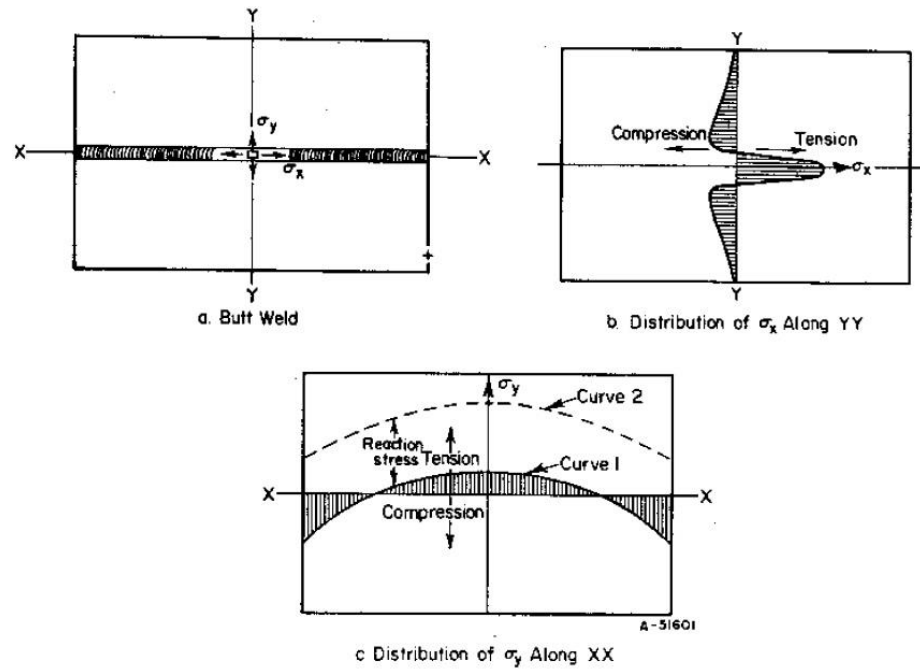
We often want to know the stress directionality in a small indent area, for example a curved structure or in-field experiments, and the Knoop indenter is difficult to use for small indent sizes because it has two obtuse angles. The intervals between the indents in indentation tests are generally recommended to be 10 times the indentation depth. Therefore doing four Knoop indentation tests and a Vickers indentation test requires a rectangular testing area of about  $1.5 \sim 2 \text{ cm}^2$ . Since residual stress varies with specimen location, local mapping in this smaller testing area means higher resolution in residual stress result. In addition, for in-field testing, changing the indenting tip is inconvenient and making two kinds of indentations is time-consuming. Moreover, curved surfaces may impose restrictions on the testing area (see Fig.2.16) it might be decreased more than 30% of testing area by using Knoop indentation only.

If the Knoop indentation test is performed on smaller indentation depths, as the load difference decreases rapidly, small experimental issues such as specimen surface preparation or indentation normality can become significant. In order to overcome this difficulty, I suggest here performing indentation testing with a novel indenter shape, a wedge indenter. There

are two reasons for evaluating residual stress directionality with a wedge indenter. The first is the decrease in indent size. Unlike the Knoop indenter, the wedge shape makes it possible to select the edge length independent of indenting depth. The second reason is the increased sensitivity to residual stresses. In this case the increased load difference between stress-free and stressed-state specimens, can be related to residual stress sensitivity on each direction. When the specifications are controlled, it is possible to maximize the residual stress sensitivity in one direction in biaxial residual stress. Here we propose a technique for residual stress evaluation with a wedge indenter and verify our model by applying stress to cruciform samples using a stress-inducing jig and by finite element analysis.

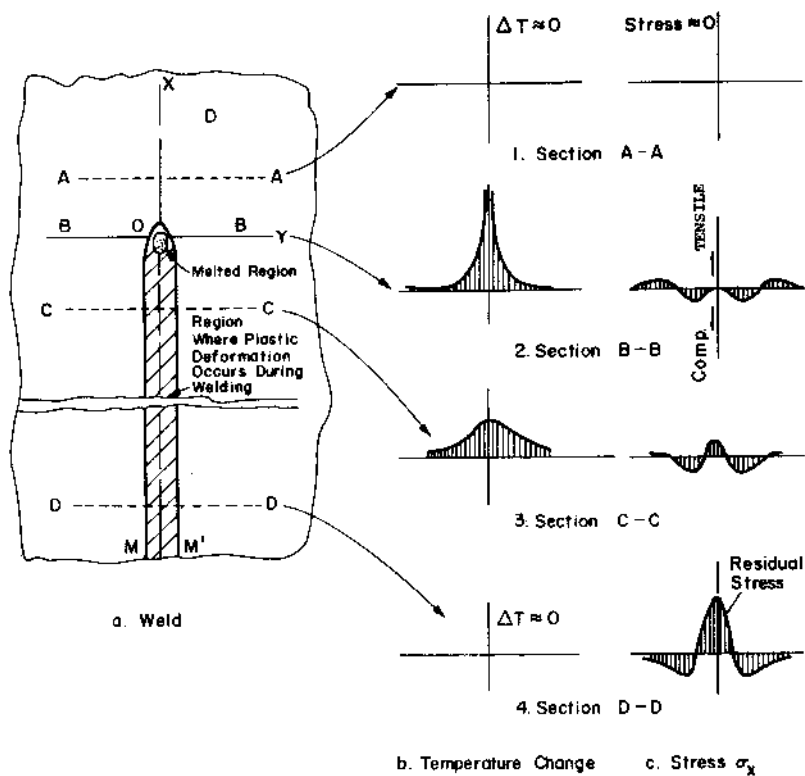


**Fig. 2.1** A thermal switch that turns on/off depending on the temperature change [26].

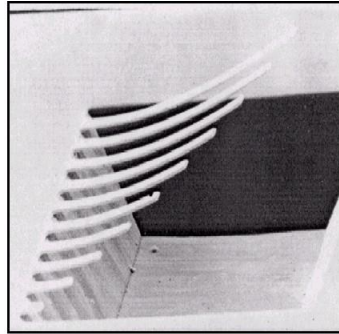


**Fig. 2.2** Residual stress distributions in plate butt joint [27].

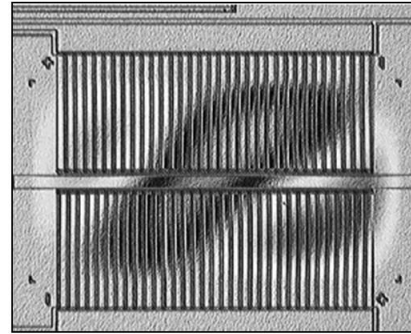




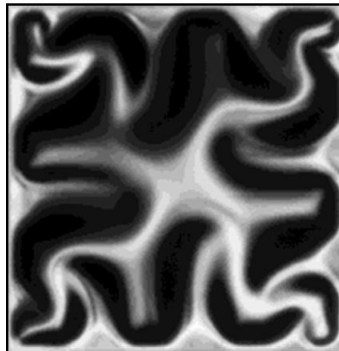
**Fig. 2.3** Schematic illustrations of heat cycles in welding and residual stress distribution [27].



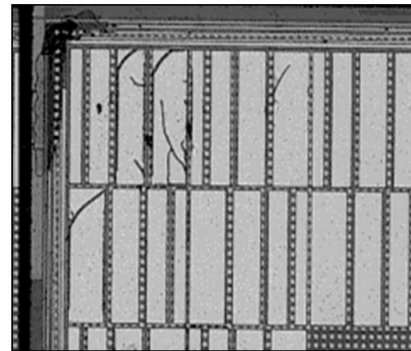
Bending



Twisting


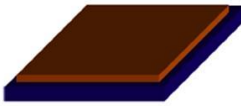
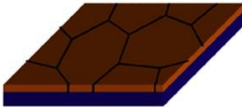
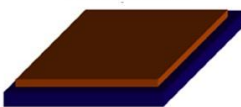
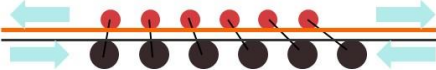


Buckling

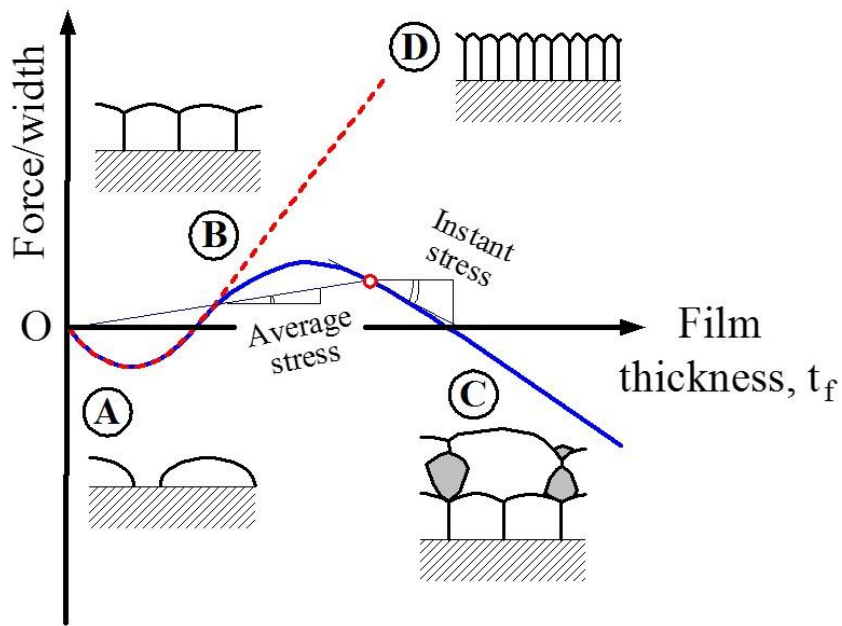


Cracking

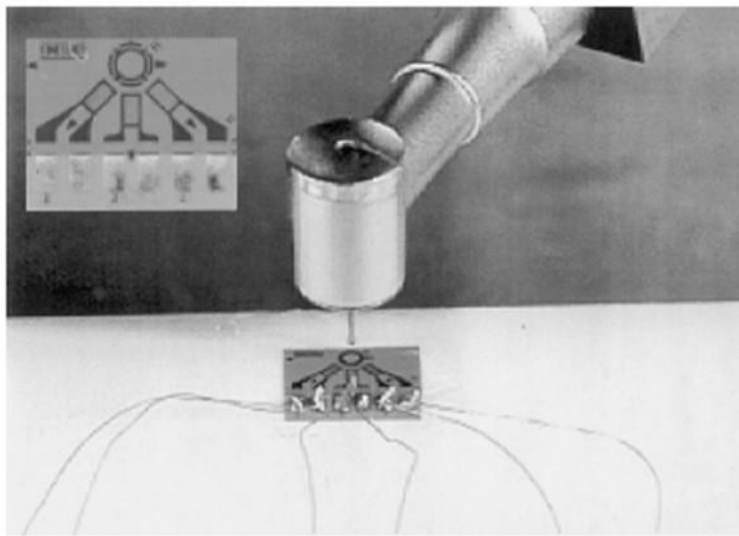
**Fig. 2.4** Residual stress effect on thin film [24].

	Cause	Mechanism
<b>Thermal stress</b>	<b>Adhesion</b> (Maintenance of adhesion)	<p>At high temperature : stress relaxation</p>  <p>Cooling down : volume shrinkage induced by coefficient of thermal expansion</p> 
<b>Intrinsic stress</b> (growth stress)		<p>Polycrystalline structure</p>  <p>Grain growth and volume shrinkage</p> 
<b>Epitaxial stress</b>	<b>Coherency</b> (Relief of atomic mismatch, maintenance of coherency)	

**Fig. 2.5** Mechanisms of thermal stress, intrinsic stress and epitaxial stress [24].

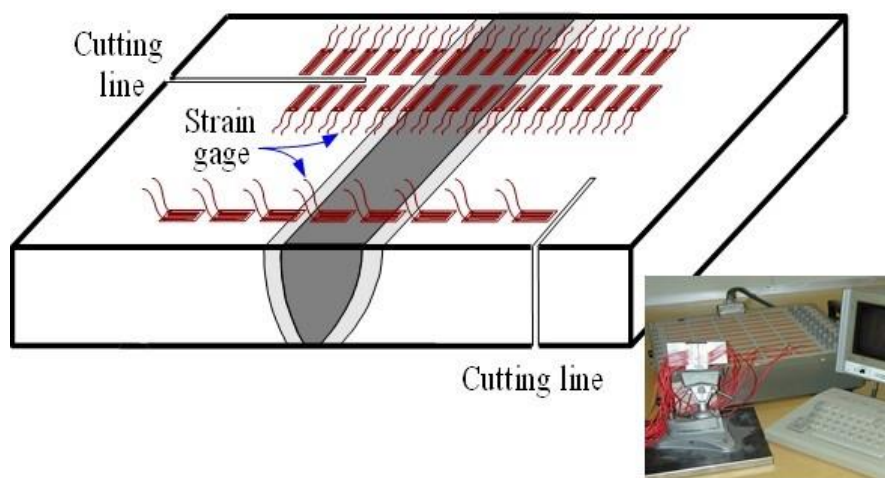


**Fig. 2.6** Schematic illustration of the force-per-width and micro structural characteristics for high-mobility and low-mobility films; (a) compressive stress in island by surface energy (tension) (b) tensile stress by elimination of grain boundary (grain growth) (c) compressive stress by continuous inputting impurity and extra atom and (d) tensile stress by substitution of island surface with grain boundary [38].

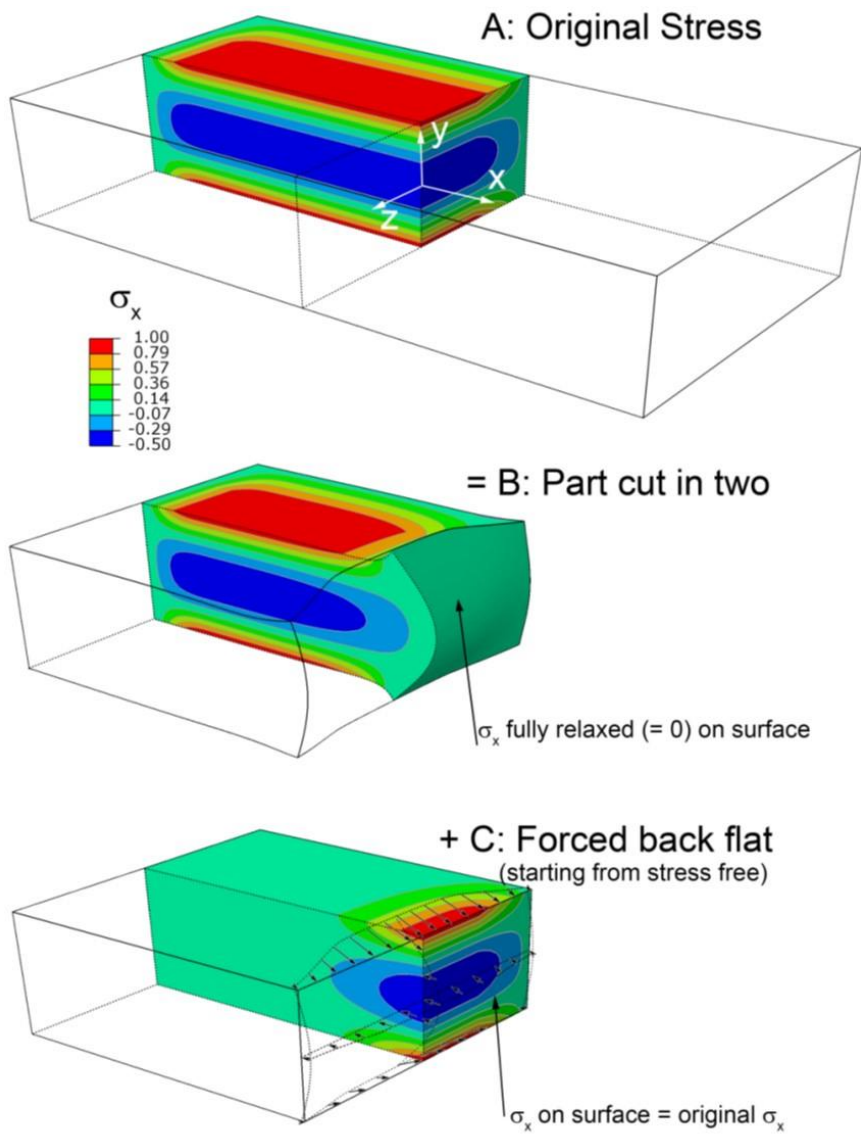


### *Hole-drilling method*

**Fig. 2.7** Hole-drilling method for evaluating residual stress.

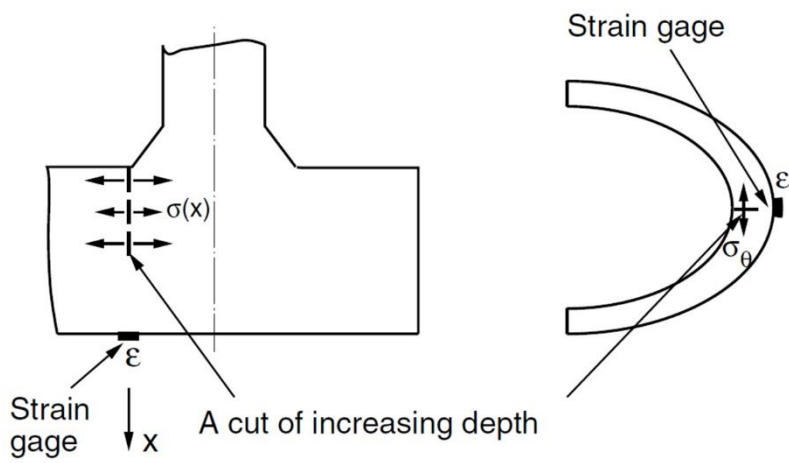


**Fig. 2.8** Schematic illustration of sectioning method.



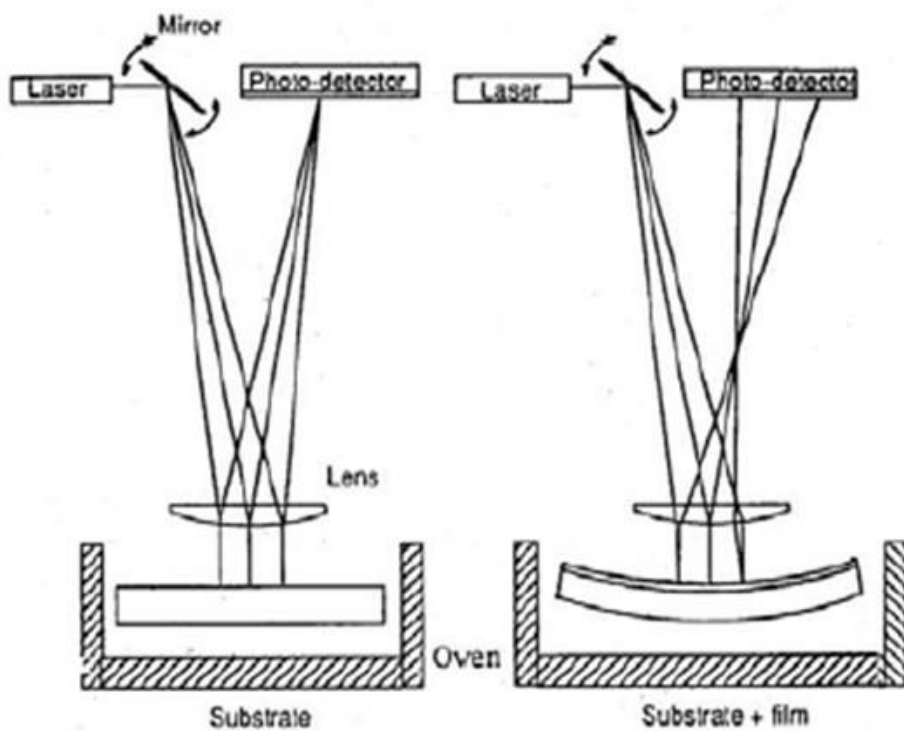
**Fig. 2.9** Schematic drawing of contour method

based on super position principle [26].

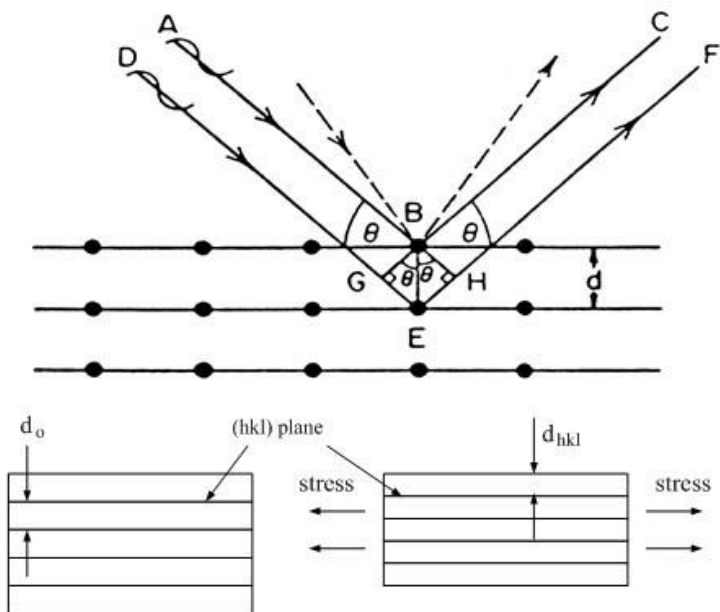


**Fig.2.10** Residual stress distribution on a plane  
which is measured by slitting method [26].

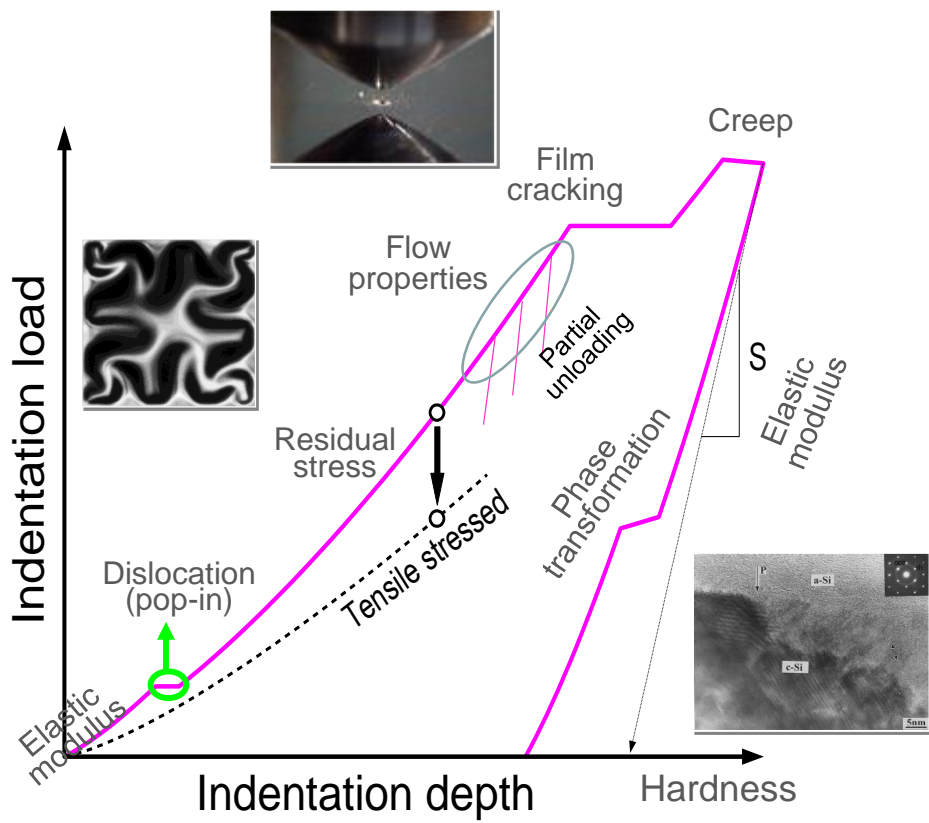




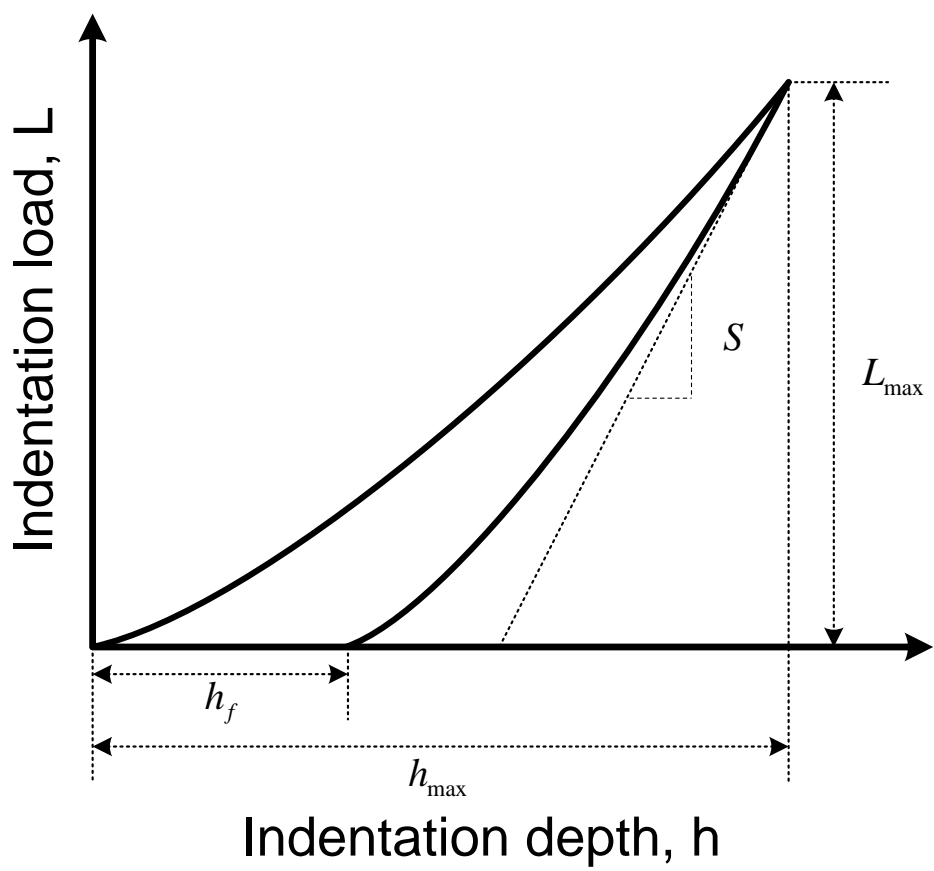
**Fig.2.11** Schematic drawing of curvature method.



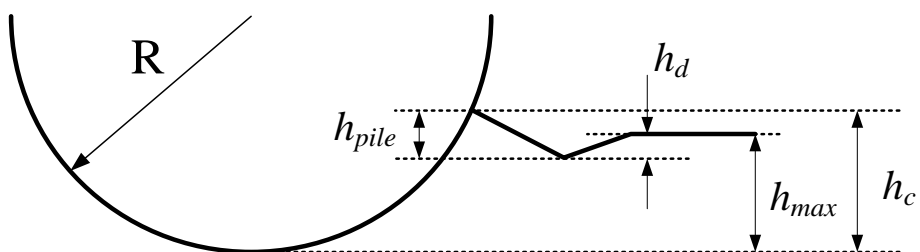
**Fig.2.12** Schematic drawing of X-ray diffraction method.



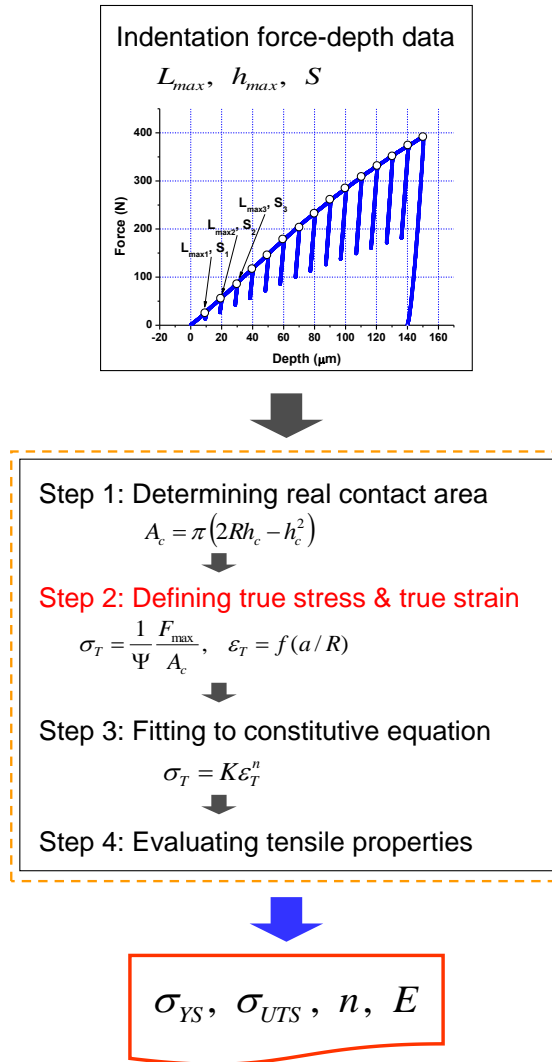
**Fig .2.13** Determined properties from indentation load-depth curve.



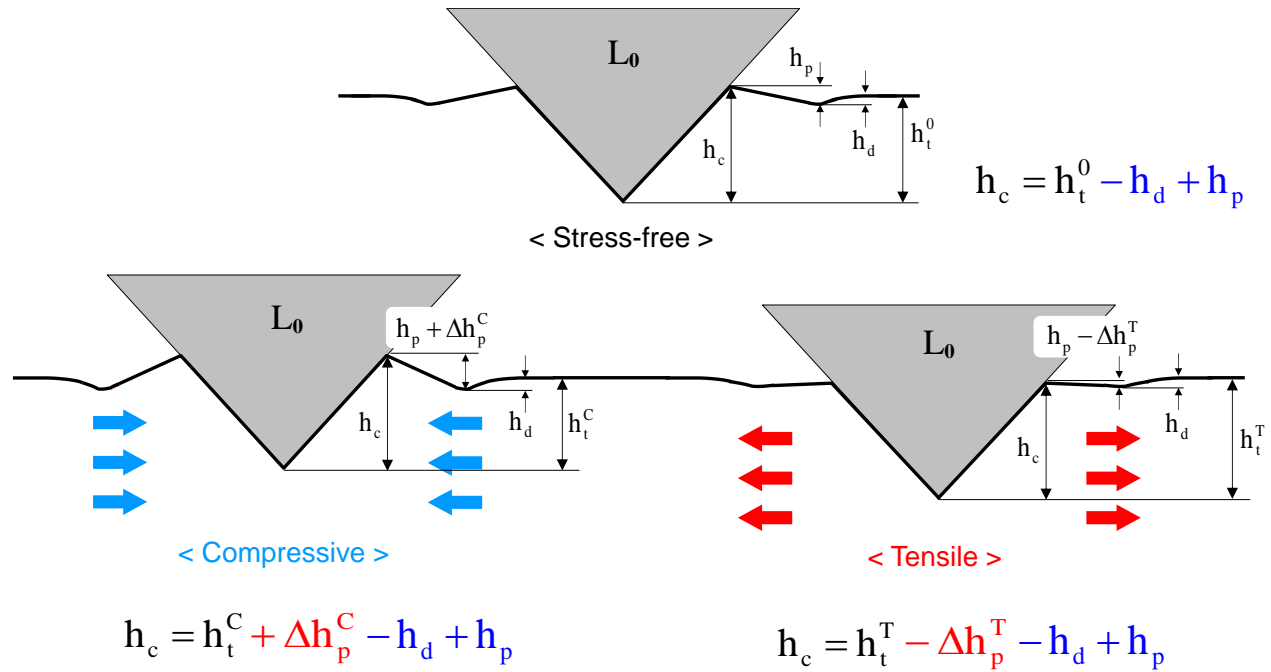
**Fig. 2.14** Schematic diagram of typical indentation load-depth curve [24].



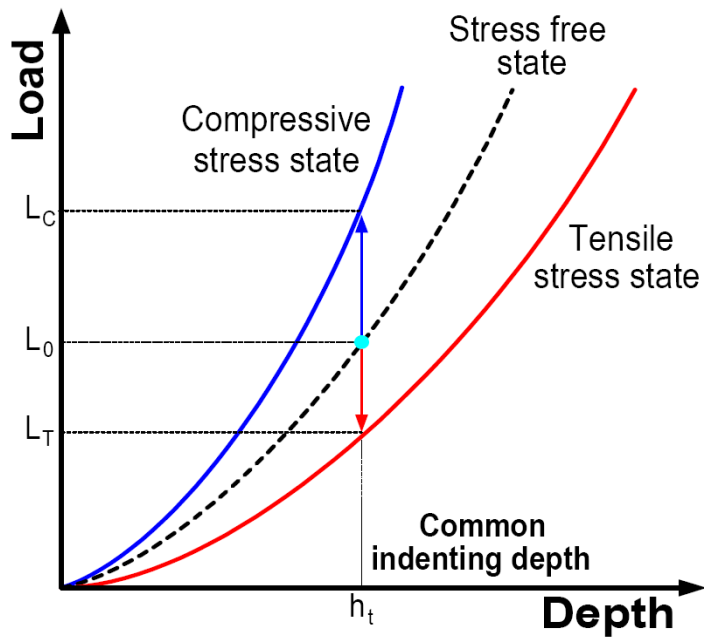
**Fig. 2.15** Cross section of spherical indenter:  
contact morphology in the loaded state [24].



**Fig. 2.16.** Schematic drawing of the tensile properties evaluation methodology [76].

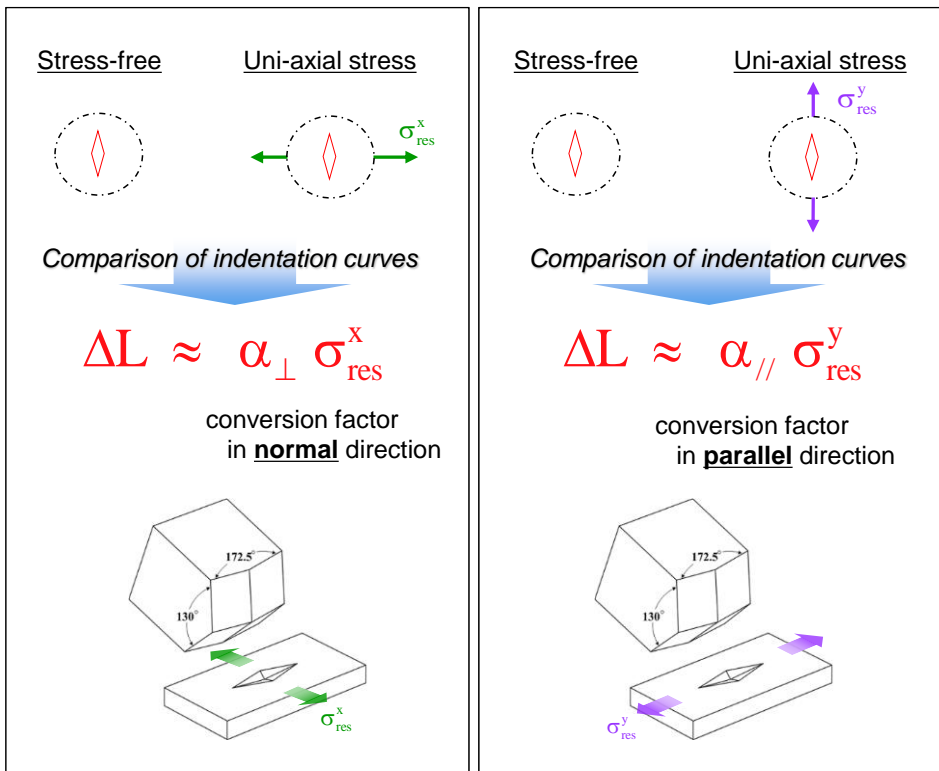


**Fig. 2.17** Schematic diagram of residual stress effect on indentation depth at the same indentation load [24].

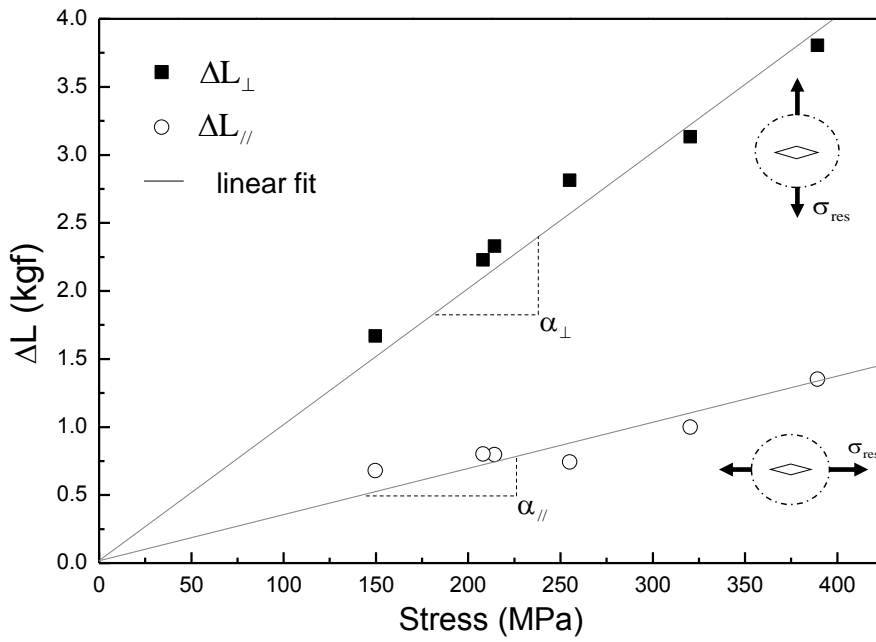


**Fig. 2.18.** Shift in indentation load-depth curve from tensile and compressive residual stress [80].

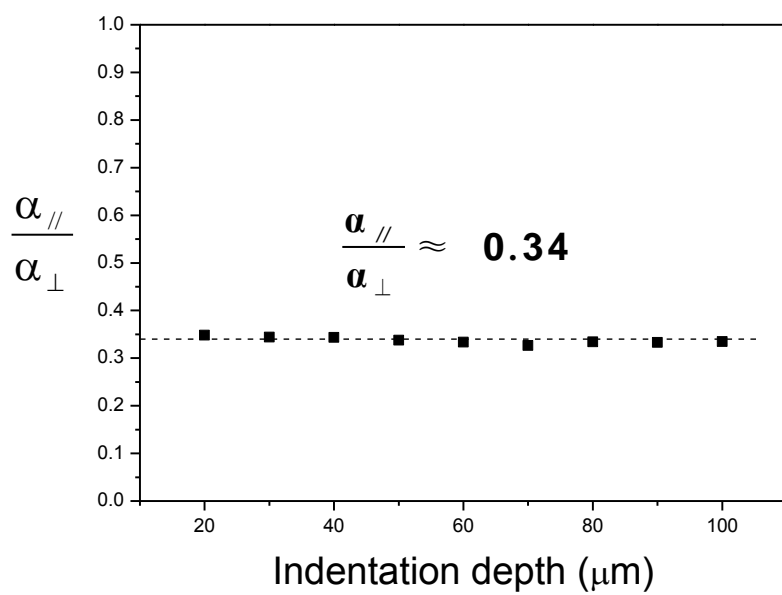




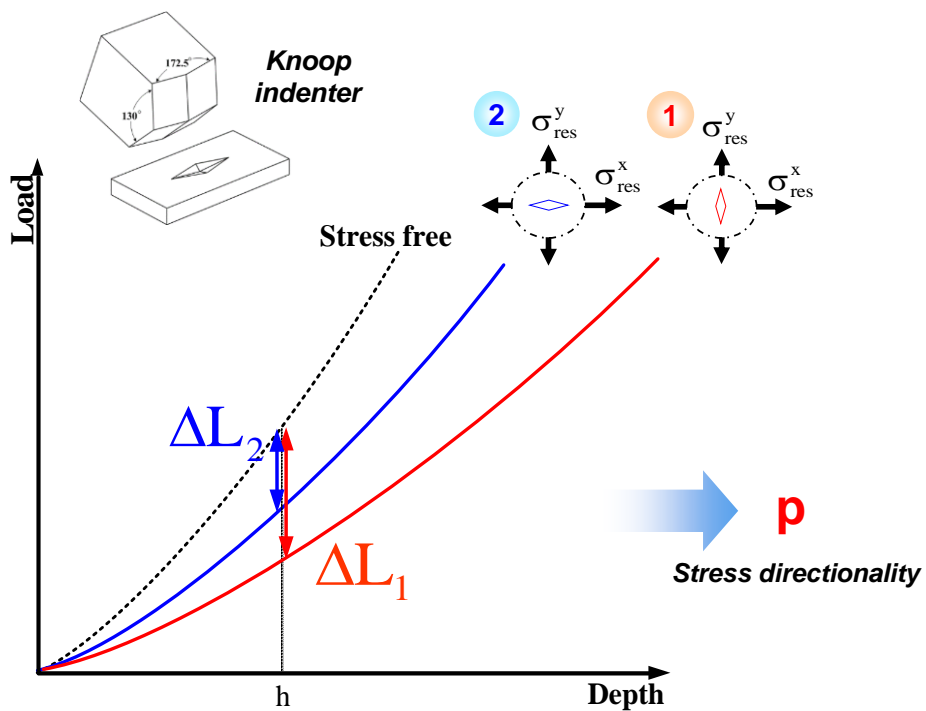
**Fig. 2.19** Definitions of conversion factors [80].



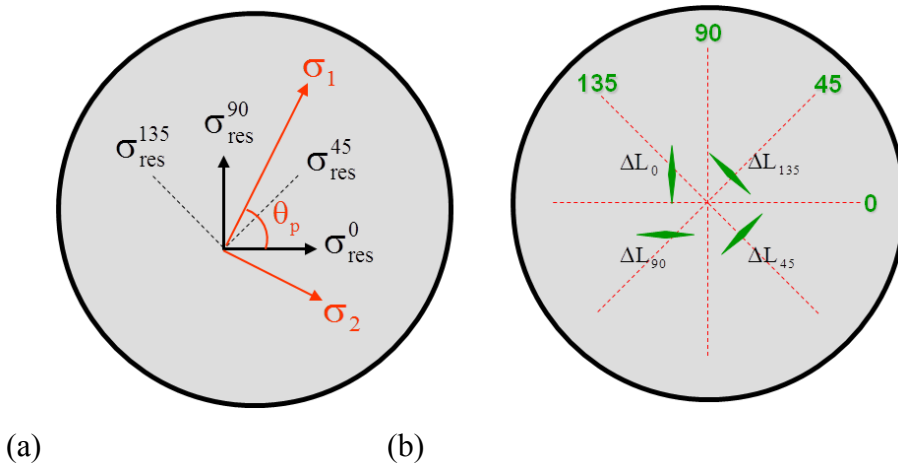
**Fig. 2.20** Conversion factors in each orthogonal directions of Knoop indenter [6]



**Fig. 2.21** Ratio of conversion factors with indentation depth [80].



**Fig. 2.22** Schematic illustration of determination of stress directionality using Knoop indenter [80].



**Fig. 2.23** (a) Stress directions of  $0^\circ$ ,  $45^\circ$ ,  $90^\circ$  and  $135^\circ$  and principal stresses and (b) orientations of Knoop indentations perpendicular to stress directions [24].

## Chapter 3

---

---

### Wedge Indentation Test Setups

#### *Contents*

3.1. Wedge Indenter Shape .....	74
3.1.1 Included Angle .....	75
3.1.2 Edge Length .....	76
3.2. Setting Machine Compliance and Zero Index.....	77
3.2.1. Machine Compliance .....	77
3.2.2. Zero Index of Wedge Indenter.....	80
3.3. Determination of Indent Interval.....	81

### 3.1 Wedge Indenter Shape

Most symmetrical indenters, like Berkovich, Vickers, cube corner and Knoop indenters are defined by their included angles; a spherical indenter is defined by its radius. However, customized indenters are often used as well. As mentioned before, the Knoop indenter was introduced to evaluate biaxial residual stresses, but is difficult to use for small indent sizes because it has two obtuse angles. For accuracy in indentation testing, enough indenting depth is essential, and the size of a Knoop indent increases as the indenter penetrates into the specimen; it is not easy to decrease the indent depth and yet attain similar accuracy and sensitivity. To overcome this limitation, another indenter shape, the wedge shape, is suggested. The wedge indenter has two dimensions: an included angle ( $\theta$ ) and an edge length ( $l$ ), (Fig. 3.1). Included angle and edge length are considered in order to optimize the shape of the wedge indenter.

### 3.1.1 Included Angle

The various included angles in wedge indenters are selected to investigate the plastic deformation beneath the indenter. In this thesis, two included angles,  $60^\circ$  and  $90^\circ$ , are considered. Although it is easily seen that the smaller included angle gives a smaller conversion factor ratio, which makes it more sensitive to stress directionality, the cracking induced by indentation is a concern. For stability and applicability to in-field structures, indentation tests with  $60^\circ$  included angle and  $90^\circ$  included angle are carried out on the same specimen. As shown in Fig. 3.2, the  $60^\circ$  wedge indenter makes a crack near the indent, but there is no crack near the  $90^\circ$  wedge indenter. Also, as the short length of the  $90^\circ$  included angle wedge indenter matches the half-indent impression of the Knoop indenter, we think this indenter shape a good one for our purposes. The  $90^\circ$  included angle is verified with optical microscopy (Fig. 3.3 (a)).



### 3.1.2 Edge Length

In order to take advantage of the indent size, the edge length of the custom wedge indenter is targeted to be one half the long diagonal of the Knoop indenter with an indentation depth of 100  $\mu\text{m}$ . As said before, the diagonals of the Knoop indenter are depth-dependent parameters, so the indenting depth criterion calculation was taken as 100  $\mu\text{m}$ . From the calculation, as the long diagonal of the Knoop indenter was about 3.05 mm at 100  $\mu\text{m}$  indentation depth, the edge length of wedge indenter was taken as 1.5 mm independent of indentation depth. Fig.3.3 (b) shows the edge length of suggested wedge indenter as observed with optical microscopy.

## 3.2 Setting Machine Compliance and Zero Index

### 3.2.1 Machine Compliance

Measuring the indentation depth in instrumented indentation is the most significant technique originating in hardness testing. As interesting feature of IIT is that even though the instrumented indentation tester is composed of an accuracy sensor for displacement measurement, the actual indentation or penetrated depth cannot be measured precisely. When compressed by the load cell, the indenting frame penetrates the specimen and the penetrated depth is recorded by a displacement sensor. However, the real penetration depth to the specimen is not the same as the depth measured by the displacement sensor, because the frame is also deformed during indentation and this additional displacement is included in the load-depth curve. Thus the deformation effect of the indenting frame must be calibrated in order to obtain an accurate indentation depth.

The concept of *frame compliance* is generally adopted in order to calibrate frame deformation. Compliance is defined as the calibration of length ( $\Delta h$ ) at unit load ( $L$ ) in the system:

$$C = \frac{\Delta h}{L}. \quad (3-1)$$

Frame compliance as an indentation system characteristic can be obtained at various indentation depths by Eq. (3-2):

$$h_{sample} = h_{total} - h_{frame} = h_{total} - LC_{frame}, \quad (3-2)$$

where  $h_{sample}$  is the unknown accurate indentation depth,  $h_{total}$  is the indentation depth directly measured by the sensor,  $h_{frame}$  is the compressed displacement at the frame and  $C_{frame}$  is frame compliance (Fig. 3.4). Oliver et al. [45] suggest a general method to determine frame compliance by considering elastic contact mechanics and invariant hardness. The general relations between compliances and indentation parameters are as follows:

$$C_{total} = C_{sample} + C_{frame}, \quad (3-3)$$

$$\frac{1}{S_{total}} = \frac{1}{S_{sample}} + C_{frame}, \quad (3-4)$$

$$\frac{1}{S_{total}} = \frac{\sqrt{\pi}}{2E_r} \frac{1}{\sqrt{A_c}} + C_{frame}, \quad (3-5)$$

$$\frac{1}{S_{total}} = \frac{\sqrt{\pi}\sqrt{H}}{2E_r} \frac{1}{\sqrt{L}} + C_{frame}, \quad (3-6)$$

Eq. (3-5) is the most general form for determining frame compliance. If contact area is measured by optical microscopy and stiffness is obtained from the unloading curve of the indentation load-depth curve, frame compliance can be taken as the intercept of the  $1/\sqrt{A_c}$  and  $1/S_{total}$  curve. As the elastic modulus is taken as constant, this method is generally accepted. Eq. (3-6) is converted from Eq. (3-5) from the definition of hardness. Frame compliance and the indenter area function can be derived from reference materials whose elastic modulus is known. From Eq. (3-6), frame compliance is also obtained from the intercept of the  $1/\sqrt{L}$  and  $1/S_{total}$  curves. In this thesis, the frame compliance is determined from the intercept of the  $1/\sqrt{A_c}$  and  $1/S_{total}$  curve and obtained

as  $0.066 \mu\text{m/kgf}$  (Fig. 3.5).

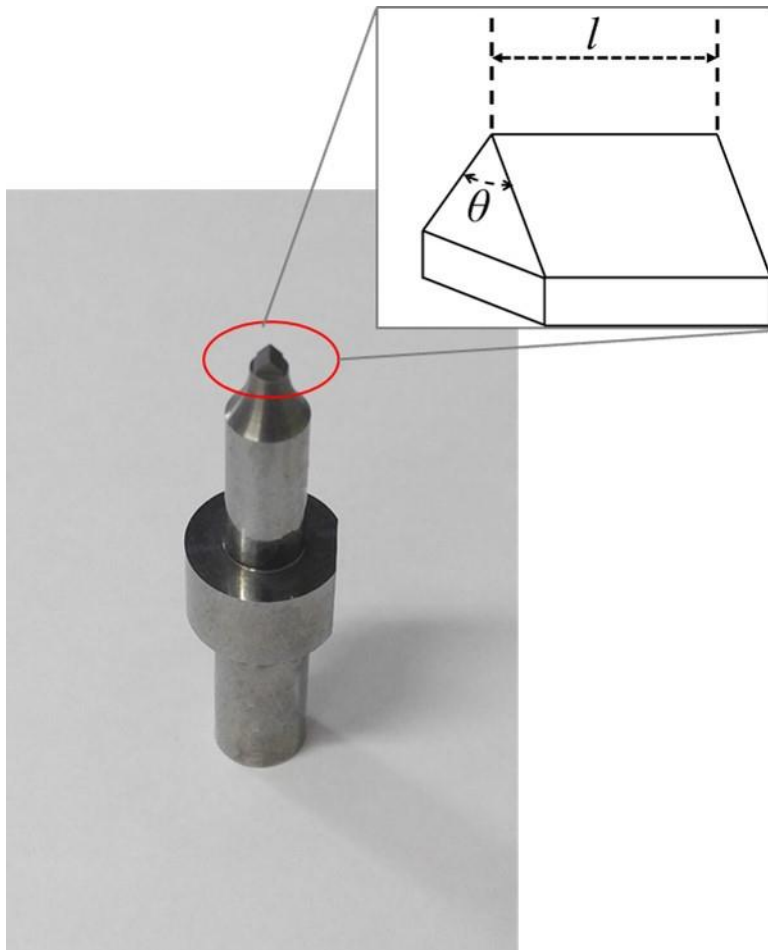
### **3.2.2 Zero Index of Wedge Indenter**

As a wedge indenter has not an initial point contact but a line contact characteristic, manufacturing a perfectly sharp wedge indenter is not easy. From the limitations on indenter shape, the initial contact is instable. From several indentation tests with smaller indenting depth than the general indenting depth (Fig. 3.6), the specific minimum indentation depth where linear contact occurs is certified. The indenting depth is conservatively matched as  $10 \mu\text{m}$ , and is converted into load, 6 kgf. As the zero index is the initially determined load value, for the obtaining stable indenting load - depth curve, the zero index is set at 6 kgf.

### 3.3. Determination of Indent Interval

The intervals between the indents in indentation tests are recommended to be 10 times the indentation depth for such widely used indenters such as sharp or spherical indenters, as shown in Fig. 3.7. Therefore four indentation tests and one Vickers indentation test need a rectangular testing area of  $1.5 \sim 2 \text{ cm}^2$ . Fig. 3.8. shows that curved surfaces may impose restrictions on the testing area: it might be decreased by more than 30% of testing area by using Knoop indentation only.

According to ISO documents [18], test results are not affected by any plastic deformation introduced by a previous indentation in a series. For convenience in determining the indent interval, finite element analysis is used and the deformed plastic zone over yield strength is certified (see Fig. 3.9). For common applications, the material with the largest yield strength over elastic modulus ratio is selected. The two cases composed of two parallel indents are considered as in Fig. 3.10, for the more general case, four indentations are also considered and compared to the Knoop indentation model in Fig. 3.11. Fig. 3.12 shows photographs of wedge and Knoop indents on stainless pipe.

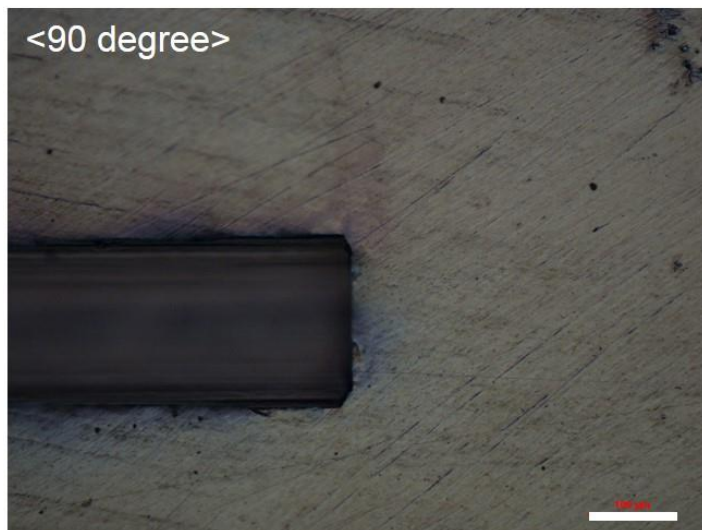


**Fig. 3.1** Shape of wedge indenter.

(a)



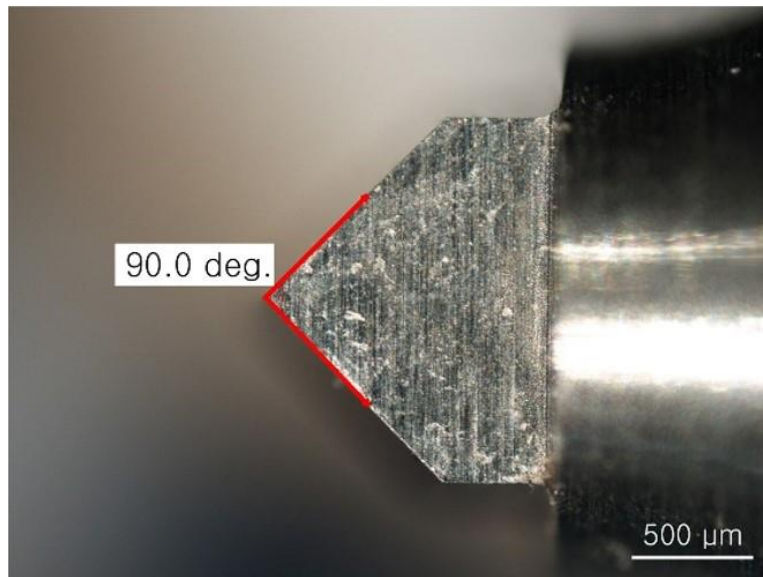
(b)



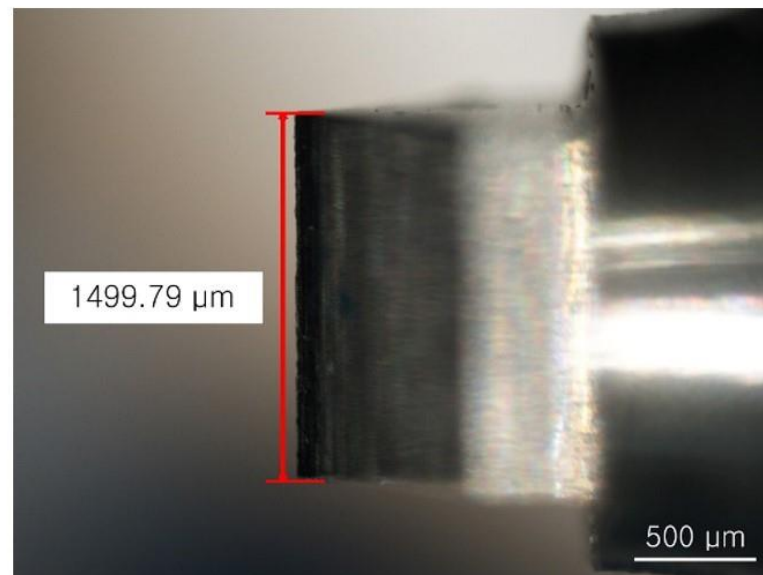
**Fig. 3.2** Indent of wedge indenter with  
(a) 60 degree angle (b) 90 degree angle.



(a)

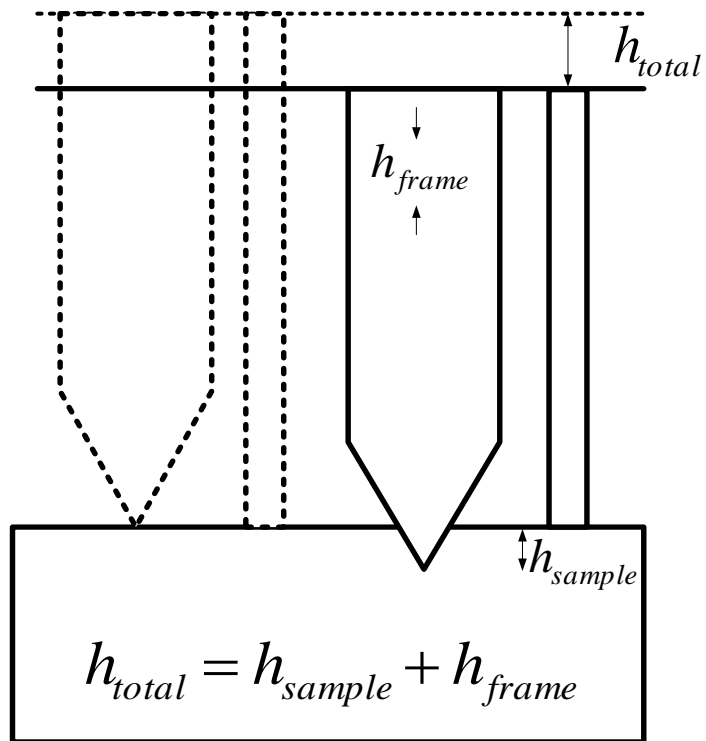


(b)

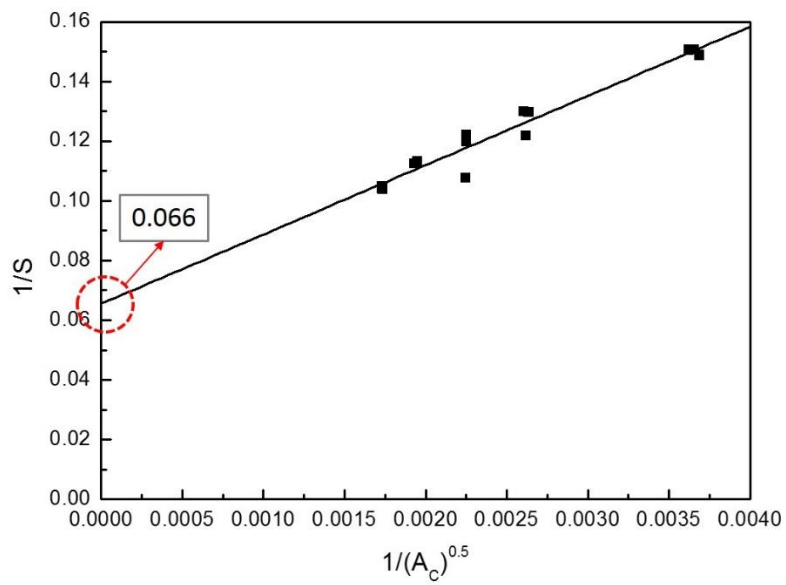


**Fig. 3.3** Specification verification of suggested wedge indenter.

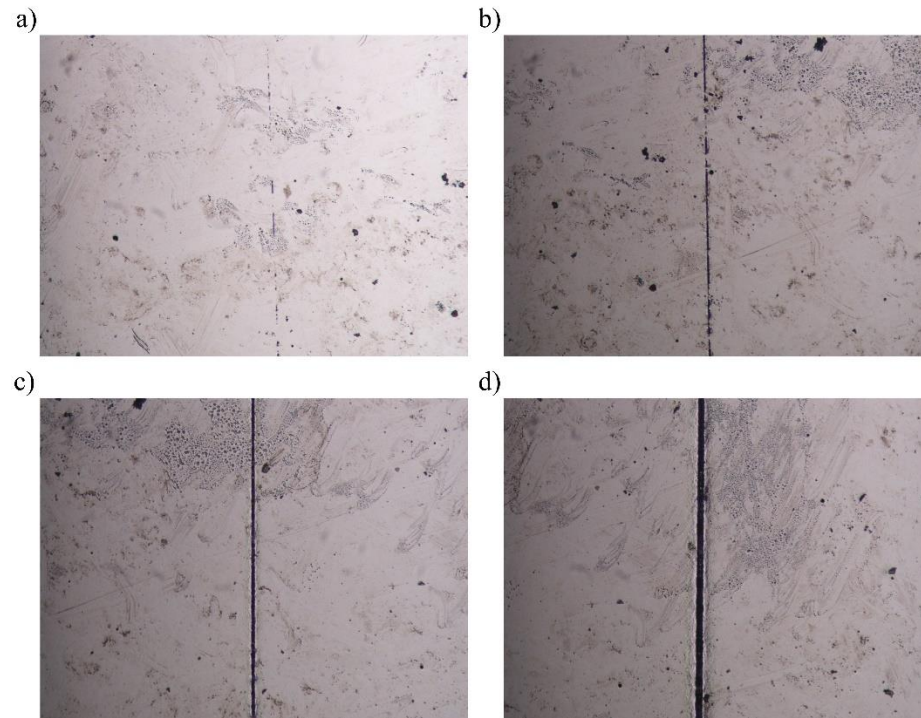
(a) included angle (b) edge length.



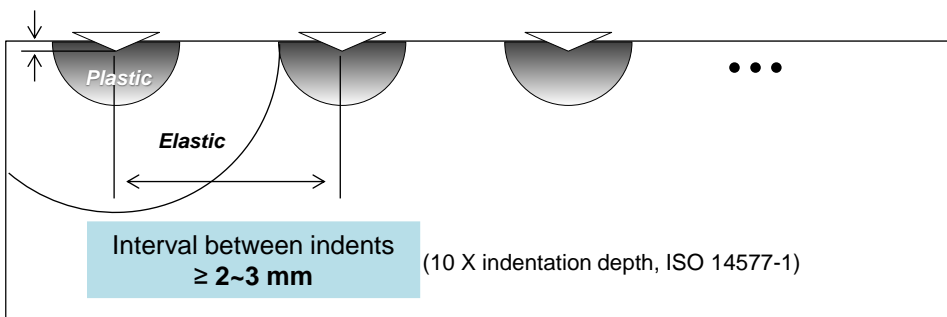
**Fig. 3.4** Deformation of indenting frame and sample [81].



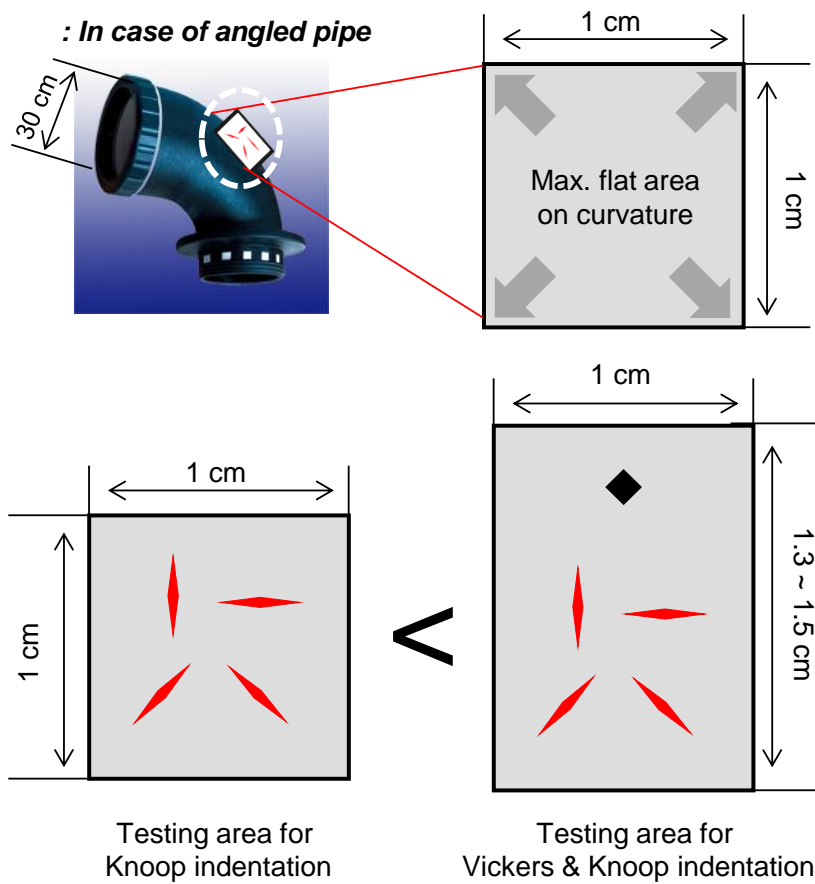
**Fig. 3.5** Machine compliance of wedge indenter.



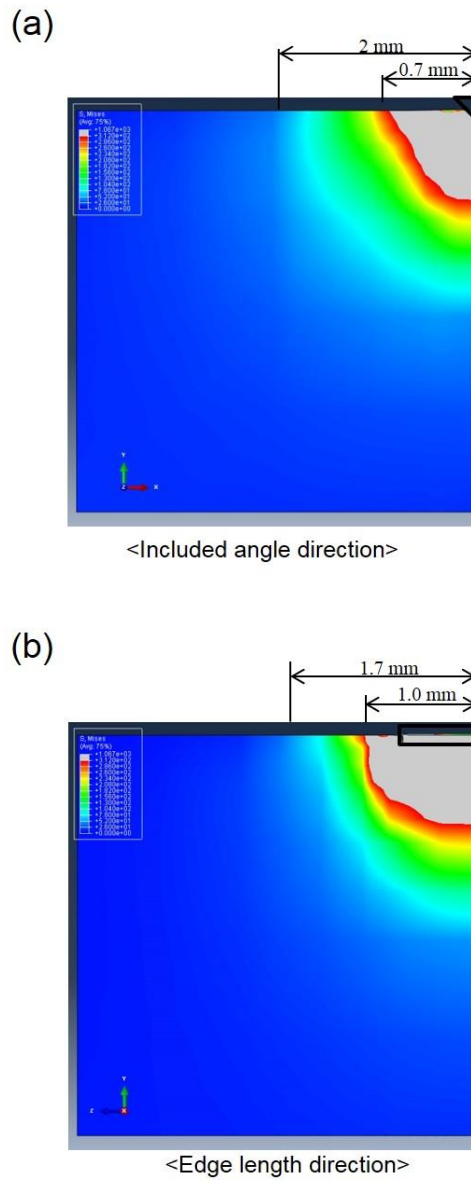
**Fig. 3.6** Several indentation tests smaller indenting depth than that of generally used: (a)  $1\mu\text{m}$  (b)  $3\mu\text{m}$  (a)  $10\mu\text{m}$  (a)  $20\mu\text{m}$ .



**Fig. 3.7** Recommended intervals between indents  
in indentation tests [76].



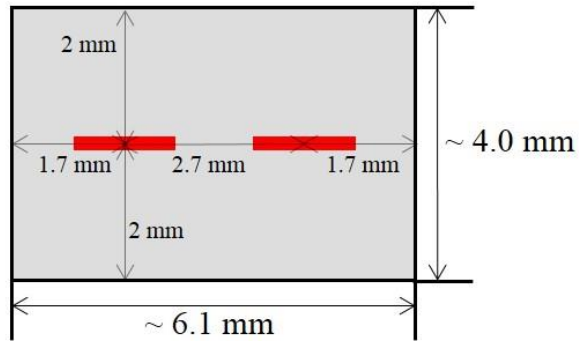
**Fig. 3.8** Comparison of required testing area  
for Vickers/Knoop and Knoop indentation models [80].



**Fig. 3.9** Plastic zone size beneath wedge indenter:  
(a) included angle direction (b) edge length direction.

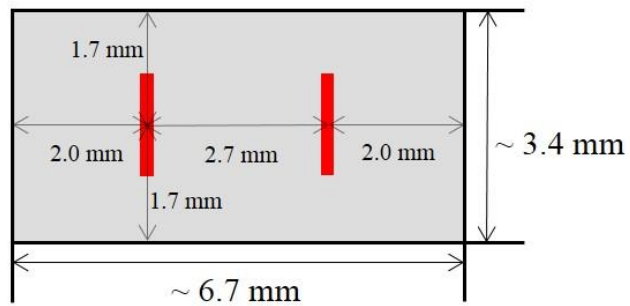
(a)

<Wedge indent size - case 1>



(b)

<Wedge indent size - case 2>

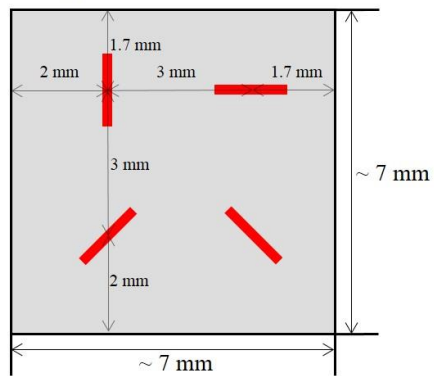


**Fig. 3.10** Considerations for indent size of two wedge indentations.



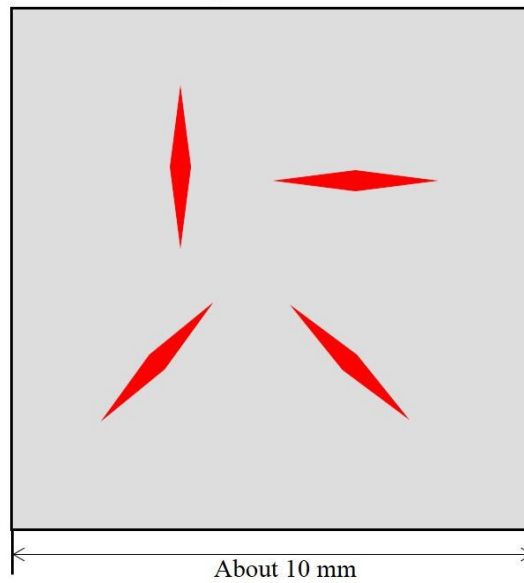
(a)

< Wedge indent size - case 3 >

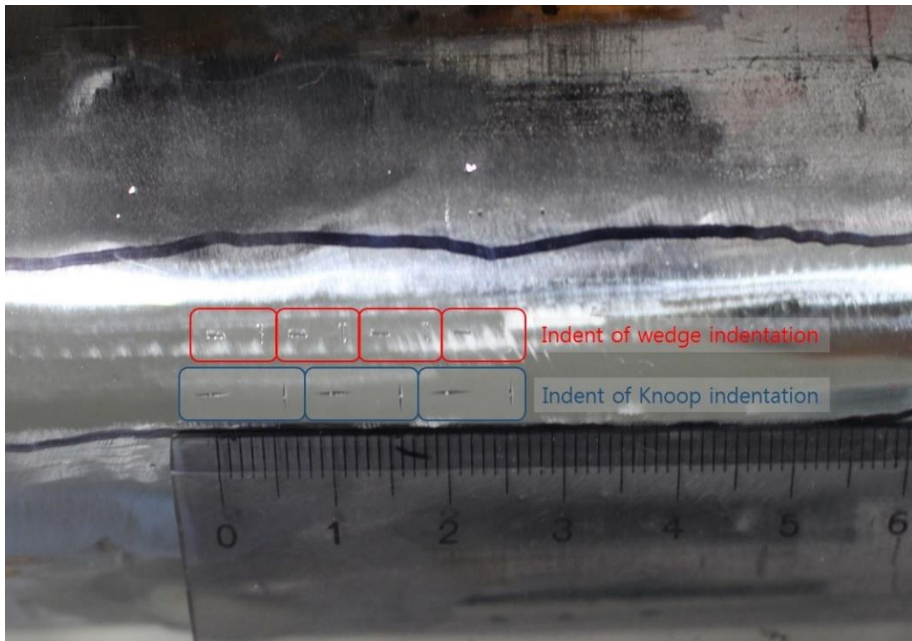


(b)

<Knoop Indentation>



**Fig. 3.11.** Considerations for indent size  
of four wedge indentations and four Knoop indentations.



**Fig. 3.12.** Comparison of indent size of two wedge indentation (red)  
and two Knoop indentation (blue)



## Chapter 4

---

---

# Determination of Conversion Factor ( $\beta$ ) for Evaluating Stress Magnitude and Directionality

### *Contents*

4.1. Modeling of Conversion Factor with Uniaxial stress state ..	96
4.2. Physical Meaning of Conversion Factor Ratio .....	100
4.2.1. Subjected area of Penetrating Indenter .....	101
4.2.2. Subjected area of Plastic Zone Beneath Indenter .....	102
4.3. Indentation Dependency of Conversion Factor Ratio.....	103

## 4.1. Modeling of Conversion Factor with Uniaxial stress state

Han et al. [6] and Choi et al. [68] introduced conversion factors as  $\alpha_{//}$  and  $\alpha_{\perp}$  for instrumented Knoop indentation testing that are variables relating the residual stress to the indentation load difference. They obtained stress directionality with a constant conversion factor ratio, of 0.34, regardless of residual stress state and indentation depth. This is an empirically determined value, without consideration of its physical meaning.

Following a similar procedure, the conversion factors, its ratio, and its summation are obtained for the wedge indenter. When wedge indentations are made on a specimen in nonequibiaxial stress, the indentation load-depth curves change depending on indenter direction. If  $\sigma_{res}^x$  is larger than  $\sigma_{res}^y$ , when the edge length direction coincides with  $\sigma_{res}^x$ , the load value at a given indenting depth  $h$ ,  $L_x$ , attains its maximum. If the edge length direction is perpendicular to  $\sigma_{res}^x$ , the load value at a given indentation depth  $h$ ,  $L_y$ , is a minimum at that indentation depth. The load

differences  $\Delta L_x$  and  $\Delta L_y$  between a stressed and stress-free specimen are calculated by considering the effect of each principal stress on the indenting load (Fig.4.1).

$$\Delta L_x = \beta_{//} \sigma_{res}^x + \beta_{\perp} \sigma_{res}^y \quad (4-1)$$

$$\Delta L_y = \beta_{\perp} \sigma_{res}^x + \beta_{//} \sigma_{res}^y \quad (4-2)$$

where  $\beta_{//}$  and  $\beta_{\perp}$  are conversion factors linking the residual stress to the indentation load difference and the subscripts mean the direction between the principal stress and the edge length direction of the wedge indenter; the concept is similar to the conversion factors,  $\alpha_{//}$ ,  $\alpha_{\perp}$  in instrumented Knoop indentation (Fig. 4.2).

In order to obtain information on stress directionality, the ratio of load differences can be addressed:

$$\frac{\Delta L_x}{\Delta L_y} = \frac{\beta_{//} \sigma_{res}^x + \beta_{\perp} \sigma_{res}^y}{\beta_{\perp} \sigma_{res}^x + \beta_{//} \sigma_{res}^y}, \quad (4-3)$$

$$\frac{\Delta L_x}{\Delta L_y} = \frac{\frac{\beta_{//}}{\beta_{\perp}} + \frac{\sigma_{res}^y}{\sigma_{res}^x}}{1 + \frac{\beta_{//}}{\beta_{\perp}} \frac{\sigma_{res}^y}{\sigma_{res}^x}}, \quad (4-4)$$

$$p = \frac{\sigma_{res}^y}{\sigma_{res}^x} = \frac{\frac{\Delta L_x}{\Delta L_y} - \frac{\beta_{//}}{\beta_{\perp}}}{1 - \frac{\beta_{//}}{\beta_{\perp}} \frac{\Delta L_x}{\Delta L_y}} \quad (4-5)$$

To evaluate the stress directionality,  $p$ , four variables,  $\Delta L_x$ ,  $\Delta L_y$ ,  $\beta_{//}$  and  $\beta_{\perp}$ , must be obtained. In particular, each conversion factors ( $\beta_{//}$ ,  $\beta_{\perp}$ ) are predetermined variables obtained from the linear slopes between load differences ( $\Delta L_x$ ,  $\Delta L_y$ ) and applied uniaxial stresses regardless of residual stress state and material. To determine these conversion factors, indentation tests were performed in various uniaxial tensile stress states.

The relationships obtained between applied stress (which corresponds to residual stress) and load differences in two orthogonal directions are plotted in Fig 4.3. The two slopes of the relations yield the ratio and sum:

$$\frac{\beta_{//}}{\beta_{\perp}} = 0.463 \quad (4-6)$$

$$\beta_{//} + \beta_{\perp} = 0.03037 \quad (4-7)$$



## 4.2. Physical Meaning of Conversion Factor Ratio

In previous research [69, 77], the conversion factor  $\beta$  for a wedge indenter is defined as:

$$\beta = \frac{\Delta L}{\sigma_{res}} \quad (4-8)$$

where  $\sigma_{res}$  and  $\Delta L$  are residual stress and load difference, respectively.

Since the conversion factor is a relationship between load (or force) and stress, we presume that it is relevant to any subjected area.

#### 4.2.1. Subjected area of Penetrating Indenter

First, since the indentation load differs with indenter orientation of indenter, the surface penetrated by the indenter is considered. The perpendicular area of the indent penetration can be calculated from indenter geometry if we ignore the elastic, plastic deformation near the indenter. The areas are designated  $A_i^\theta$ ,  $A_i^l$  along with the included angle direction and edge length direction (Fig. 4.4):

$$A_i^\theta = \frac{1}{2}h^2 \tan\left(\frac{\theta}{2}\right) \quad (4-9)$$

$$A_i^l = hl \quad (4-10)$$

where  $h$  is indentation depth,  $\theta$  is included angle, and  $l$  is edge length. Since the suggested wedge indenter has 90 degree included angle, 1.5 mm edge length, and 100  $\mu\text{m}$  indentation depth, the ratio of two penetrated area converges to 0.033, and it is not suited the experimentally determined conversion factor ratio.

#### **4.2.2. Subjected area of Plastic Zone beneath Indenter**

As the residual stress evaluation algorithm is correlated with the deviatoric stress term induced by the indentation load, it can be assumed that the size of the plastic deformed zone related by a conversion factor. Thys, the size of the plastic zone under the wedge indenter is compared with conversion factor ratio obtained experimentally. Because the method for experimentally identifying the plastic zone size is not well established, a finite element analysis of wedge indentation is introduced. The analysis was conducted by inputting mechanical properties of 6 materials (see Table 4.1), the subjected area ratio from two directional plastic zone size conversion factor ratio at 100  $\mu\text{m}$  indentation depth. The plastic zone size is calculated by counting the plastic region which exceeds the input yield strength of material as gray area in Fig. 4.5. The ratio, 0.474 is determined as in Table 4.2., and it is deduced that the relation between conversion factor and subjected area of plastic zone under indenter is present.

### 4.3. Indentation Dependency of Conversion Factor Ratio

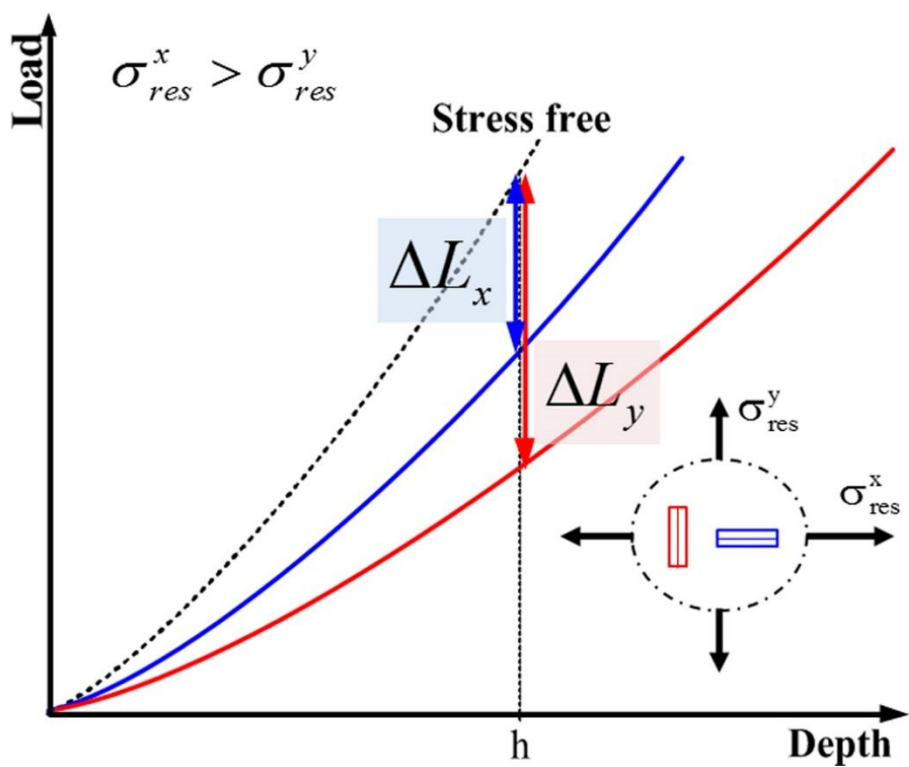
For the Knoop indenter [10], the conversion factor ratio ( $\alpha_{//} / \alpha_{\perp}$ ) converges to 0.34 independent of indentation depth because of the indenter's geometrical self-similarity in both perpendicular directions. However, a wedge indenter has the indenter's geometrical self-similarity in the included angle direction, but there is no geometrical self-similarity in the edge length direction (Fig. 4.6). Hence, a linear relationship between the conversion factor ratio and indentation depth is deduced. Fig.4.7 shows a linear relationship between the conversion factor ratio from the load difference obtained in experiments and finite element analysis and indentation depth. For determining physical meaning of conversion factor ratio, the two directional subjected areas of plastic zone are considered through finite element analysis approach. The plastic zone area is obtained from various steps in ABAQUS that correspond to 60  $\mu\text{m}$ , 70  $\mu\text{m}$ , 80  $\mu\text{m}$ , 90  $\mu\text{m}$ , and 100  $\mu\text{m}$  indentation depth. The plot of the plastic zone size ratio and indentation depth shows linearity as expected (Fig. 4.8) and is a meaningful result. However, the slope and intercept values are somewhat different from Fig. 4.7, the further studies are needed on this difference.

**Table 4.1.** Mechanical properties used for plastic zone size ratio.

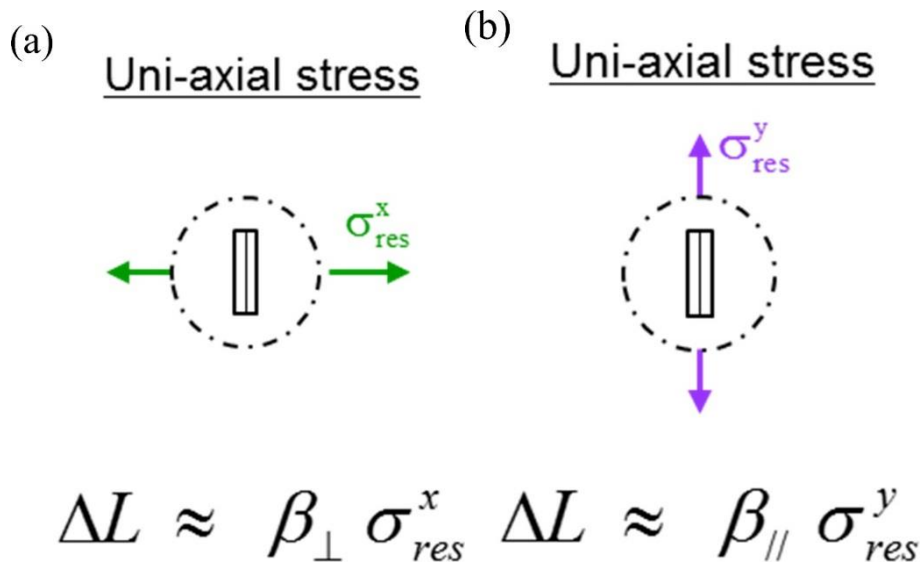
Materials	Poisson's ratio	Elastic modulus (GPa)	Yield strength (MPa)
S45C	0.29	202	320
STS303	0.30	206	328
STS304	0.29	183	235
STS410	0.28	198	418
Al2024	0.33	72	408
Cu11000	0.33	102	228

**Table 4.2.** Plastic zone size of two directions and the ratio.

	$A_p^\theta$	$A_p^l$	$\frac{A_p^\theta}{A_p^l}$
S45C	254602	499094	0.510
STS303	126118	255703	0.493
STS304	236226	455105	0.518
STS410	228076	470633	0.485
Al2021	178964	417198	0.429
Cu11000	164782	401525	0.410

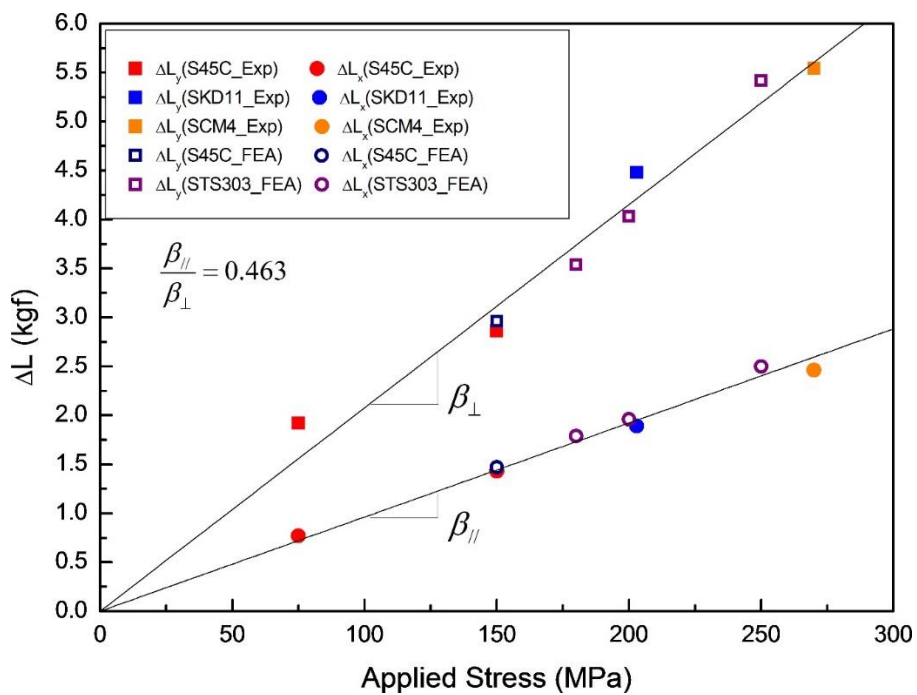


**Fig. 4.1.** Schematic indentation load-depth curve from two wedge indentations in the biaxial stress state.

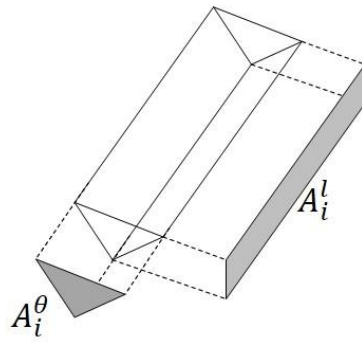


**Fig. 4.2.** Definition of conversion factor (a)  $\beta_{\perp}$ , (b)  $\beta_{\parallel}$ .



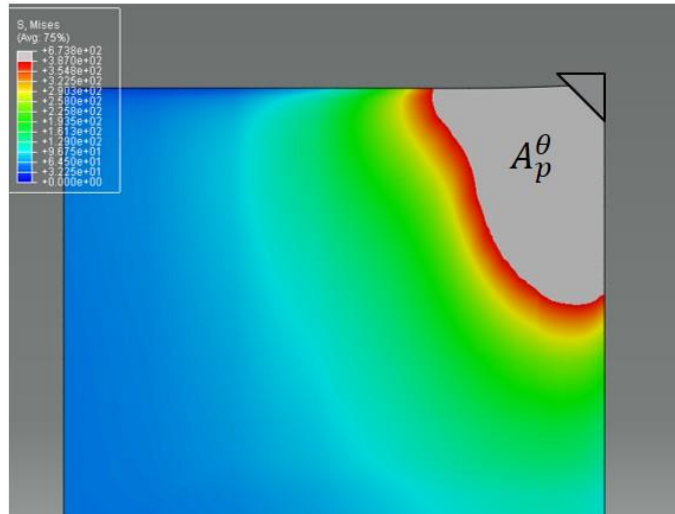


**Fig. 4.3.** Relationship between applied stresses and load differences [77].

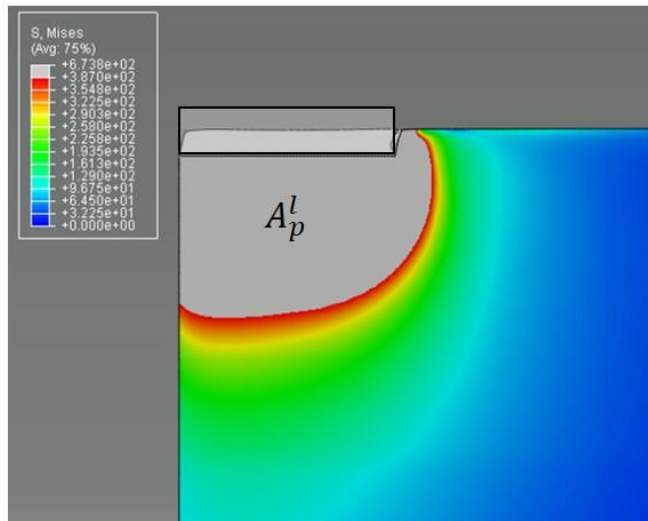


**Fig. 4.4.** Subjected area of penetrating wedge indenter.

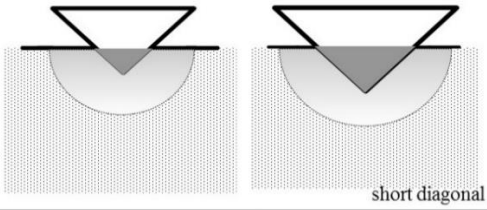
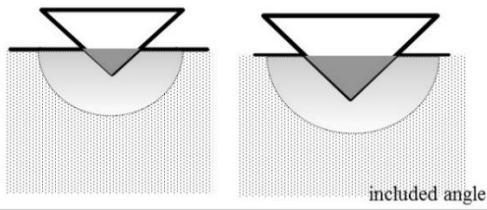
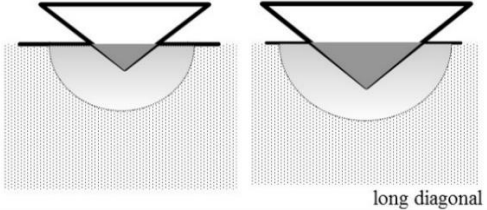
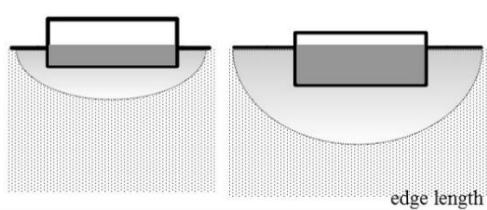
(a)



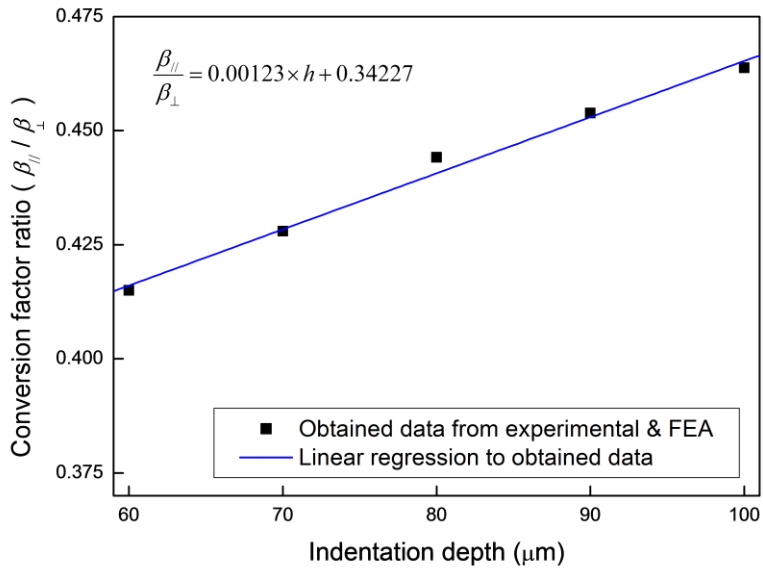
(b)



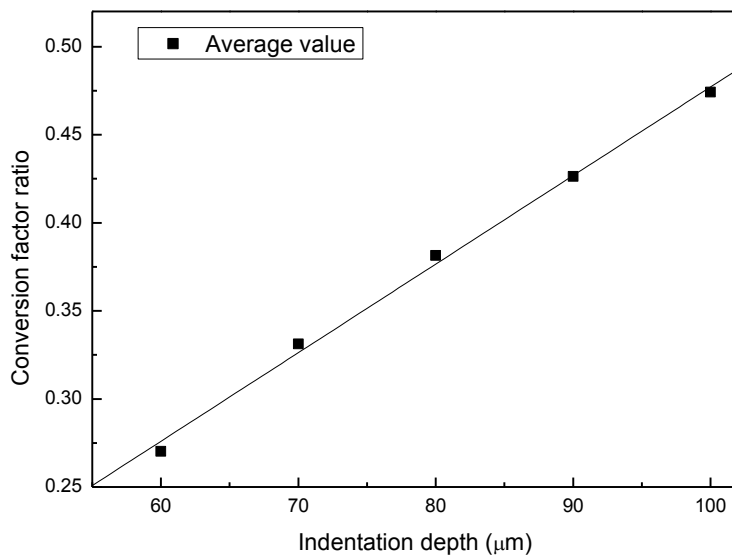
**Fig. 4.5.** Determination of plastic zone size of two directions by finite element analysis.

	<Knoop indenter>	<Wedge indenter>
Direction1	 short diagonal	 included angle
Direction2	 long diagonal	 edge length
Conversion factor ratio	<p>Both directions have geometrical self-similarity for entire indentation depth</p> <p style="text-align: center;">↓</p> <p style="text-align: center;"><b><u>Constant conversion factor ratio</u></b> independent of indentation depth</p>	<p>Included Angle direction has geometrical self-similarity, but edge length direction does not.</p> <p style="text-align: center;">↓</p> <p style="text-align: center;"><b><u>Conversion factor ratio</u></b> <b><u>dependent of indentation depth</u></b></p>

**Fig. 4.6.** Geometrical self-similarity consideration of two directions  
for reviewing the conversion factor ratio dependency on indentation depth.



**Fig. 4.7.** Conversion factor ratio dependency on indentation depth determined from load difference of experiments and FEA [77].



**Fig. 4.8.** Conversion factor ratio dependency on indentation depth determined from ratio of plastic zone size.



## Chapter 5

---

---

# Modeling for Evaluating Residual Stress Magnitude and Directionality

### *Contents*

5.1	Modeling for Evaluating Sum of Biaxial Residual Stress	
	Magnitudes with Wedge Indentation .....	116
5.2	Modeling for Evaluating Residual Stress Directionality and	
	Magnitude with Wedge Indentation .....	119
	5.2.1 Known Principal Direction .....	119
	5.2.2 Unknown Principal Direction .....	121



## 5.1. Modeling for Evaluating Sum of Biaxial Residual Stress Magnitudes with Wedge Indentation

To evaluate the surface residual stress by instrumented indentation testing, with a Vickers indenter, the load difference between the stressed state and stress-free state is needed: with a Knoop indenter, two indentations are needed. A novel modeling with wedge indenter is introduced that is based on the summation of Eq. (4-1) and Eq. (4-2):

$$\Delta L_x + \Delta L_y = \beta_{//} \sigma_{res}^x + \beta_{\perp} \sigma_{res}^x + \beta_{\perp} \sigma_{res}^y + \beta_{//} \sigma_{res}^y \quad (5-1)$$

The sum of the residual stresses can be obtained by rearranging Eq. (5-1):

$$\sigma_{res}^x + \sigma_{res}^y = \frac{1}{(\beta_{//} + \beta_{\perp})} \Delta L_x + \Delta L_y \quad (5-2)$$

As the sum of the conversion factors is predetermined (see Eq. (4-7)), the sum of the residual stresses can be obtained by any load differences from two wedge indentations on principal directions.

The sum of load differences at 90° intervals for the case of unknown principal direction is found. To estimate the principal direction and stress ratio of the residual stress, four times indentation tests at 45° intervals are needed and the relation of the sum of load differences between 0°, 90° and 45°, 135° is found:

$$\Delta L_0 = \beta_{\perp} \sigma_{res}^0 + \beta_{//} \sigma_{res}^{90} \quad (5-3)$$

$$\Delta L_{90} = \beta_{//} \sigma_{res}^0 + \beta_{\perp} \sigma_{res}^{90} \quad (5-4)$$

$$\Delta L_{45} = \beta_{\perp} \sigma_{res}^{45} + \beta_{//} \sigma_{res}^{135} \quad (5-5)$$

$$\Delta L_{135} = \beta_{//} \sigma_{res}^{45} + \beta_{\perp} \sigma_{res}^{135} \quad (5-6)$$

The sum of Eq. (5-3), Eq. (5-4) and Eq. (5-5), Eq. (5-6) is

$$\Delta L_0 + \Delta L_{90} = (\beta_{\perp} + \beta_{//})(\sigma_{res}^0 + \sigma_{res}^{90}) \quad (5-7)$$

$$\Delta L_{45} + \Delta L_{135} = (\beta_{\perp} + \beta_{//})(\sigma_{res}^{45} + \sigma_{res}^{135}) \quad (5-8)$$

This model is based on the assumption that the evaluated each directional residual stresses by wedge indentation is independent on the orientation of wedge indentation as a reference line. This approach is the same that a

principal direction from the hardness obtained axisymmetric indenter is invariant of orientation. Oppel [78] suggested that the relationship between normal stress and change of Knoop hardness is linear and also that this relation is valid for angular orientation (Fig. 5.1). He also found that changes in hardness were equal for 45° and 135° indenter orientation, which the sum of hardness changes in directions perpendicular to each other for a particular point at a particular loading is constant, and that hardness changes do not depend on shear stresses. This relation is expressed as

$$\sigma_{res}^0 + \sigma_{res}^{90} = \sigma_{res}^{45} + \sigma_{res}^{135} = \sigma_{\theta} + \sigma_{\theta+90} \quad (5-9)$$

From Eq. (5-7), Eq. (5-8) and Eq. (5-9), the load difference relation can be expressed as:

$$\Delta L_0 + \Delta L_{90} = \Delta L_{45} + \Delta L_{135} \quad (5-10)$$

## 5.2 Modeling for Evaluating Residual Stress Directionality and Magnitude with Wedge Indentation

### 5.2.1 Known Principal Direction

For a known principal axis of targeted surface residual stress, as in weldment, only two wedge indentation tests on the axis which are known in advance are needed (See Fig. 5.2(a)). The principal surface residual stress can be expressed as in Eq. (4-1) and Eq. (4-2) and rearranged as Eq. (5-3) and Eq. (5-4).

$$\Delta L_0 = \beta_{\perp} \sigma_{res}^0 + \beta_{//} \sigma_{res}^{90} \quad (5-3)$$

$$\Delta L_{90} = \beta_{//} \sigma_{res}^0 + \beta_{\perp} \sigma_{res}^{90} \quad (5-4)$$

Eq. (4-5) can be used for evaluating the stress ratio,  $p$ , and can be expressed as

$$p = \frac{\sigma_2}{\sigma_1} = \frac{\frac{\Delta L_{90}}{\beta_{\perp}} - \frac{\beta_{\parallel}}{\Delta L_0}}{1 - \frac{\beta_{\parallel}}{\beta_{\perp}} \frac{\Delta L_{90}}{\Delta L_0}} \quad (5-11)$$

By combining the stress magnitudes as expressed in Eq. (5-2), the principal residual stresses can be summarized as:

$$\sigma_1 = \frac{(\Delta L_0 + \Delta L_{90})}{(\beta_{\perp} + \beta_{\parallel})} \frac{1}{1+p} = \frac{(\Delta L_0 + \Delta L_{90})}{(\beta_{\perp} + \beta_{\parallel})} \frac{1 - \frac{\beta_{\parallel}}{\beta_{\perp}} \frac{\Delta L_{90}}{\Delta L_0}}{1 - \frac{\beta_{\parallel}}{\beta_{\perp}} \frac{\Delta L_{90}}{\Delta L_0} + \frac{\Delta L_{90}}{\Delta L_0} - \frac{\beta_{\parallel}}{\beta_{\perp}}} \quad (5-12)$$

$$\sigma_2 = \frac{(\Delta L_0 + \Delta L_{90})}{(\beta_{\perp} + \beta_{\parallel})} \frac{p}{1+p} = \frac{(\Delta L_0 + \Delta L_{90})}{(\beta_{\perp} + \beta_{\parallel})} \frac{\frac{\Delta L_{90}}{\beta_{\perp}} - \frac{\beta_{\parallel}}{\Delta L_0}}{1 - \frac{\beta_{\parallel}}{\beta_{\perp}} \frac{\Delta L_{90}}{\Delta L_0} + \frac{\Delta L_{90}}{\Delta L_0} - \frac{\beta_{\parallel}}{\beta_{\perp}}} \quad (5-13)$$

### 5.2.2. Unknown Principal Direction

As mentioned in the previous chapter, the basic concept of estimating principal direction by wedge indentation is based on four wedge indentation tests at a randomly oriented  $0^\circ$  to  $135^\circ$  at  $45^\circ$  interval in Fig.5.2(b). The residual stresses of each directions are  $\sigma_{res}^0$ ,  $\sigma_{res}^{90}$ ,  $\sigma_{res}^{45}$ , and  $\sigma_{res}^{135}$ . The load differences induced by wedge indentation along the defined four directions are determined as  $\Delta L_0$ ,  $\Delta L_{90}$ ,  $\Delta L_{45}$ , and  $\Delta L_{135}$ .

These four load differences can be thought of as two sets of load difference with 90 degree interval. From the stress directionality evaluation model, Eq. (4-5), The stress ratios between  $\sigma_{res}^0$ ,  $\sigma_{res}^{90}$  and  $\sigma_{res}^{45}$ ,  $\sigma_{res}^{135}$  can be evaluated by the ratios of  $\Delta L_0$ ,  $\Delta L_{90}$ , and  $\Delta L_{45}$ ,  $\Delta L_{135}$ . Here,  $p'$  and  $p''$  are expressed as

$$p' = \frac{\sigma_{res}^{90}}{\sigma_{res}^0} = \frac{\frac{\Delta L_{90}}{\beta_{//}} - \frac{\beta_{//}}{\beta_{\perp}}}{1 - \frac{\beta_{//}}{\beta_{\perp}} \frac{\Delta L_{90}}{\Delta L_0}} \quad (5-14)$$

$$p'' = \frac{\sigma_{res}^{135}}{\sigma_{res}^{45}} = \frac{\frac{\Delta L_{135}}{\beta_{//}} - \frac{\beta_{//}}{\beta_{\perp}}}{1 - \frac{\beta_{//}}{\beta_{\perp}} \frac{\Delta L_{135}}{\Delta L_{45}}} \quad (5-15)$$

From the plane stress transformation on [79],  $\sigma_\theta$  is expressed by rotating of the stress direction using the following two equations:

$$\sigma_\theta = \frac{\sigma_x + \sigma_y}{2} + \frac{\sigma_x - \sigma_y}{2} \cos 2\theta + \tau_{xy} \sin 2\theta \quad (5-16)$$

$$\tan 2\theta_p = \frac{2\tau_{xy}}{\sigma_x - \sigma_y} \quad (5-17)$$

The relation between the principal angle and the four directional stresses  $\sigma_{res}^0$ ,  $\sigma_{res}^{45}$ ,  $\sigma_{res}^{90}$ , and  $\sigma_{res}^{135}$  is as follows, where for convenience, x and y are replaced with 0 and 90:

$$\sigma_\theta = \frac{\sigma_{res}^0 + \sigma_{res}^{90}}{2} + \frac{\sigma_{res}^0 - \sigma_{res}^{90}}{2} \cos 2\theta + \tau_{xy} \sin 2\theta \quad (5-18)$$

$$\tan 2\theta_p = \frac{2\tau_{xy}}{\sigma_{res}^0 - \sigma_{res}^{90}} \quad (5-19)$$

Based on Oppel's approach to the independence of Knoop hardness and

orientation, the effect of shear stress on load differences,  $\tau_{xy}$  of Eq. (5-19) can be inserted into Eq. (5-18) to yield

$$\sigma_{\theta} = \frac{\sigma_{res}^0 + \sigma_{res}^{90}}{2} + \frac{\sigma_{res}^0 - \sigma_{res}^{90}}{2} \cos 2\theta + \frac{\sigma_{res}^0 - \sigma_{res}^{90}}{2} \cdot \tan 2\theta_p \sin 2\theta \quad (5-20)$$

When we consider the case  $\theta = 45^\circ$ , Eq. (5-20) becomes

$$\sigma_{45} = \frac{\sigma_{res}^0 + \sigma_{res}^{90}}{2} + \frac{\sigma_{res}^0 - \sigma_{res}^{90}}{2} \cdot \tan 2\theta_p \quad (5-21)$$

Dividing both sides of Eq. (5-21) by  $\sigma_{res}^0 + \sigma_{res}^{90}$  yields

$$\frac{\sigma_{45}}{\sigma_{res}^0 + \sigma_{res}^{90}} = \frac{1}{2} + \frac{1}{2} \frac{\sigma_{res}^0 - \sigma_{res}^{90}}{\sigma_{res}^0 + \sigma_{res}^{90}} \cdot \tan 2\theta_p \quad (5-22)$$

By substituting  $\sigma_{res}^0 + \sigma_{res}^{90}$  into  $\sigma_{res}^{45} + \sigma_{res}^{135}$  on the left side, Eq. (5-22) can be expressed as



$$\frac{\sigma_{45}}{\sigma_{res}^{45} + \sigma_{res}^{135}} = \frac{1}{2} + \frac{1}{2} \frac{\sigma_{res}^0 - \sigma_{res}^{90}}{\sigma_{res}^0 + \sigma_{res}^{90}} \cdot \tan 2\theta_p \quad (5-23)$$

Rearranging Eq. (5-23) produces

$$\frac{\sigma_{res}^{45} - \sigma_{res}^{135}}{\sigma_{res}^{45} + \sigma_{res}^{135}} = \frac{\sigma_{res}^0 - \sigma_{res}^{90}}{\sigma_{res}^0 + \sigma_{res}^{90}} \cdot \tan 2\theta_p \quad (5-24)$$

The principal direction is expressed as

$$\frac{\sigma_{res}^{45} - \sigma_{res}^{135}}{\sigma_{res}^{45} + \sigma_{res}^{135}} = \frac{\sigma_{res}^0 - \sigma_{res}^{90}}{\sigma_{res}^0 + \sigma_{res}^{90}} \cdot \tan 2\theta_p \quad (5-25)$$

$$\tan 2\theta_p = \frac{\sigma_{res}^0 + \sigma_{res}^{90}}{\sigma_{res}^0 - \sigma_{res}^{90}} \cdot \frac{\sigma_{res}^{45} - \sigma_{res}^{135}}{\sigma_{res}^{45} + \sigma_{res}^{135}} \quad (5-26)$$

By dividing  $\sigma_{res}^0$ ,  $\sigma_{res}^{45}$  on the right side of Eq. (5-26), the principal direction can be expressed by following stress ratio:

$$\tan 2\theta_p = \frac{1 + \frac{\sigma_{res}^{90}}{\sigma_{res}^0} \cdot \frac{1 - \frac{\sigma_{res}^{135}}{\sigma_{res}^{45}}}{1 - \frac{\sigma_{res}^{90}}{\sigma_{res}^0} + \frac{1 + \frac{\sigma_{res}^{135}}{\sigma_{res}^{45}}}{\sigma_{res}^{45}}} \quad (5-27)$$

$$\tan 2\theta_p = \frac{1 + p'}{1 - p'} \cdot \frac{1 - p''}{1 + p''} \quad (5-28)$$

For the principal stress ratio expressed by  $p'$  or  $p''$  and  $\theta_p$ , replacing  $\theta$  with  $\theta_p$  and  $\theta_p + 90^\circ$  in Eq. (5-20) yields

$$\sigma_1 = \frac{\sigma_{res}^0 + \sigma_{res}^{90}}{2} + \frac{\sigma_{res}^0 - \sigma_{res}^{90}}{2} \cos 2\theta_p + \left( \frac{\sigma_{res}^0 - \sigma_{res}^{90}}{2} \right) \sin 2\theta_p \cdot \tan 2\theta_p \quad (5-29)$$

$$\sigma_2 = \frac{\sigma_{res}^0 + \sigma_{res}^{90}}{2} - \frac{\sigma_{res}^0 - \sigma_{res}^{90}}{2} \cos 2\theta_p - \left( \frac{\sigma_{res}^0 - \sigma_{res}^{90}}{2} \right) \sin 2\theta_p \cdot \tan 2\theta_p \quad (5-30)$$

The principal stress ratio  $P$  can be expressed as

$$\frac{\sigma_2}{\sigma_1} = \frac{\frac{\sigma_{res}^0 + \sigma_{res}^{90}}{2} - \frac{\sigma_{res}^0 - \sigma_{res}^{90}}{2} \cos 2\theta_p - \left( \frac{\sigma_{res}^0 - \sigma_{res}^{90}}{2} \right) \sin 2\theta_p \cdot \tan 2\theta_p}{\frac{\sigma_{res}^0 + \sigma_{res}^{90}}{2} + \frac{\sigma_{res}^0 - \sigma_{res}^{90}}{2} \cos 2\theta_p + \left( \frac{\sigma_{res}^0 - \sigma_{res}^{90}}{2} \right) \sin 2\theta_p \cdot \tan 2\theta_p} \quad (5-31)$$

Eq. (5-31) is rearranged as

$$\frac{\sigma_2}{\sigma_1} = \frac{(\sigma_{res}^0 + \sigma_{res}^{90}) \cos 2\theta_p - (\sigma_{res}^0 - \sigma_{res}^{90}) \cos^2 2\theta_p - (\sigma_{res}^0 - \sigma_{res}^{90}) \sin^2 2\theta_p}{(\sigma_{res}^0 + \sigma_{res}^{90}) \cos 2\theta_p + (\sigma_{res}^0 - \sigma_{res}^{90}) \cos^2 2\theta_p + (\sigma_{res}^0 - \sigma_{res}^{90}) \sin^2 2\theta_p} \quad (5-32)$$

$$\frac{\sigma_2}{\sigma_1} = \frac{(\sigma_{res}^0 + \sigma_{res}^{90}) \cos 2\theta_p - (\sigma_{res}^0 - \sigma_{res}^{90}) (\cos^2 2\theta_p + \sin^2 2\theta_p)}{(\sigma_{res}^0 + \sigma_{res}^{90}) \cos 2\theta_p + (\sigma_{res}^0 - \sigma_{res}^{90}) (\cos^2 2\theta_p + \sin^2 2\theta_p)} \quad (5-33)$$

By using two sets of stress ratio, Eq. (5-33) becomes

$$P = \frac{\sigma_2}{\sigma_1} = \frac{(1 + p') \cos 2\theta_p - (1 - p')}{(1 + p') \cos 2\theta_p + (1 - p')} \quad (5-34)$$

When x and y in Eq. (5-2) are replaced by 1 and 2, the equation can be

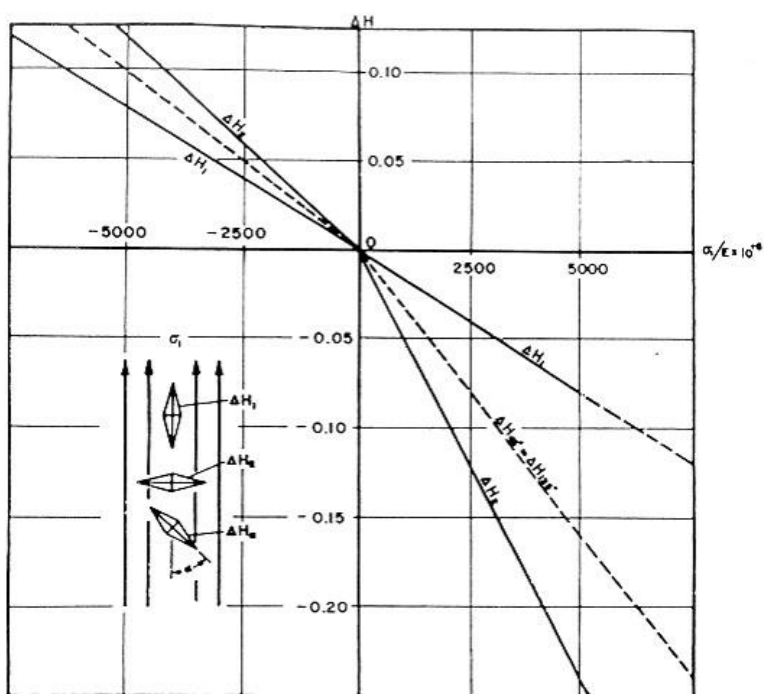
expressed as

$$\sigma_1 + \sigma_2 = \frac{1}{(\beta_{//} + \beta_{\perp})} \Delta L_0 + \Delta L_{90} \quad (5-35)$$

By combining Eq. (5-34) and Eq. (5-35), the principal stresses can be expressed as

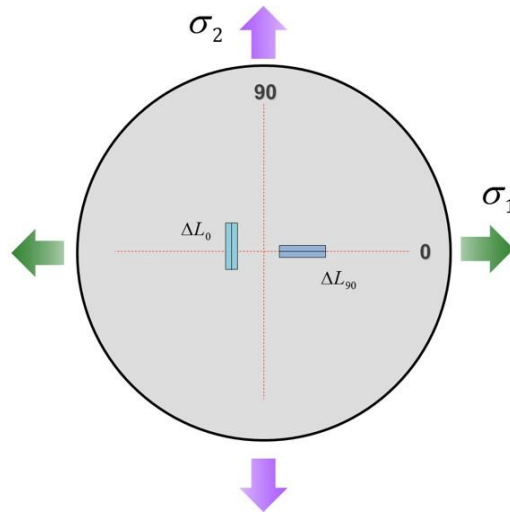
$$\sigma_1 = \frac{(\Delta L_0 + \Delta L_{90})}{(\beta_{\perp} + \beta_{//})} \frac{(1 + p') \cos 2\theta_p + (1 - p')}{2 \cdot (1 + p') \cos 2\theta_p} \quad (5-36)$$

$$\sigma_2 = \frac{(\Delta L_0 + \Delta L_{90})}{(\beta_{\perp} + \beta_{//})} \frac{(1 + p') \cos 2\theta_p - (1 - p')}{2 \cdot (1 + p') \cos 2\theta_p} \quad (5-37)$$

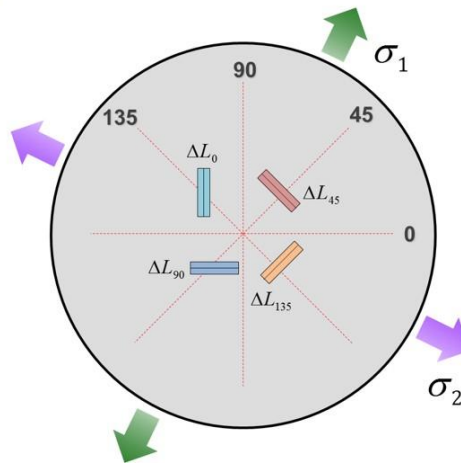


**Fig. 5.1.** Change of Knoop (axisymmetric) hardness of aluminum and steel due to uniaxial stress [78].

(a)



(b)



**Fig. 5.2** Schematic drawing of wedge indentations:

(a) known principal direction (b) unknown principal direction.

	Known principal direction (2 times indentations)	Unknown principal direction (4 times indentations)
Schematic drawing		
Obtained value from indentation	$\Delta L_0 \Rightarrow \mathbf{p}$ $\Delta L_{90}$	$\Delta L_0 \Rightarrow \mathbf{p}'$ $\Delta L_{90}$ $\Delta L_{45} \Rightarrow \mathbf{p}''$ $\Delta L_{135}$
Principal direction	-	$\theta_p = \frac{1}{2} \tan^{-1} \left( \frac{(1+p')(1-p'')}{(1-p')(1+p'')} \right)$
Magnitude of Stress	$\sigma_1 = \frac{(\Delta L_0 + \Delta L_{90})}{(\beta_{\perp} + \beta_{\parallel})} \frac{1}{1+p}$ $\sigma_2 = \frac{(\Delta L_0 + \Delta L_{90})}{(\beta_{\perp} + \beta_{\parallel})} \frac{\mathbf{p}}{1+p}$	$\sigma_1 = \frac{(\Delta L_0 + \Delta L_{90})}{(\beta_{\perp} + \beta_{\parallel})} \frac{(1+p') \cos 2\theta_p + (1-p')}{2 \cdot (1+p') \cos 2\theta_p}$ $\sigma_2 = \frac{(\Delta L_0 + \Delta L_{90})}{(\beta_{\perp} + \beta_{\parallel})} \frac{(1+p') \cos 2\theta_p - (1-p')}{2 \cdot (1+p') \cos 2\theta_p}$

**Fig. 5.3** Summary of wedge indentations: (a) known principal direction (b) unknown principal direction.

## Chapter 6

---

---

### Experimental Verification of Model

#### *Contents*

6.1. Experimental Apparatus .....	132
6.1.1. Testing Equipment and Specimens .....	132
6.1.2. Stress Generating Jig .....	134
6.2. Finite Element Analysis Condition .....	135
6.3. Results and Discussion .....	137
6.3.1. Verification of Experiments with Stress-generating jig .....	137
6.3.2. Comparison of Residual Stress Summation with Previous Vickers Model .....	138



## **6.1 Experimental Details**

### **6.1.1 Testing Equipment and Specimens**

The AIS 3000 equipment made by Frontics Inc., Republic of Korea, (Fig. 6.1), used for the instrumented indentation tests. The resolution of load and depth resolution is 5.6 gf and 0.1  $\mu\text{m}$ , the maximum load was 300 kgf and loading and unloading speed were fixed at 0.3 mm/min. The experiments were performed as displacement control condition and maximum indentation depth was determined as 100  $\mu\text{m}$ . The wedge indenter was made of tungsten carbide by H.M.TEC in Republic of Korea (Fig. 3.1).

To determine the conversion factor ratio, the experimental process used on three samples: SCM4, S45C and SKD11, properties of which appear in Table 6.1. As the residual stress is not a material property but a stress state, it can be deduced that the residual stresses are independent of materials. For convenient and rapid material supply, the experimental materials were carbon steel. The 10-mm-thick cruciform samples (Fig. 6.2) were machined from a bare plate and heat-treated to remove internal

manufacturing stress. After stress relaxation by annealing, no bending or warping was observed in the sample. Indentation samples were finely polished with no. 1500 sand paper.

To verify the model developed here, six kinds of materials (Al6061, SKD11, S45C, STS304, STS316, STS440C) were used: material properties are summarized in Table 6.2. The specimen shape and heat treatment are the same as those of specimens for the conversion factor ratio determination.

### 6.1.2 Strain Apparatus

A stress-generating jig was designed to apply strain to the cruciform specimen by two independent orthogonal loading axes, as shown in Fig. 6.2. Surface strains were induced by stress-applying screws at the end of each specimen, and they were indicated by strain gauge on the exposed specimen surface. The biaxial stresses were calculated from biaxial strains of the two orthogonal axes using the elastic modulus and Poisson's ratio. The Tresca yield criterion is considered for preventing plastic deformation, two orthogonal principal stresses were determined below each specimen's yield strength. The applied stress states for conversion factor ratio determination are shown in Table 6.3, and the applied stress states for principal stress determination consisted of uniaxial, equibiaxial, and nonequibiaxial stress, as summarized in Table 6.3.

## 6.2 Finite Element Analysis Condition

Finite element analysis was performed using the commercial finite element code ABAQUS 6.12. Various uniaxial applied stress states were generated in the specimens, and wedge indentation was conducted twice perpendicular and parallel to the applied uniaxial stress direction. The specimens were S45C and STS303. The simulation of wedge indentation was made up of 104,832 elements of C3D8R mesh-type specimen, 1901 elements of R3D4 and 20 elements of R3D3 mesh-type indenter (Fig. 6.3.). The elastic modulus and yield strength of STS 303 were 206 GPa and 328 MPa, and those of S45C were 202 GPa and 320 MPa. The material models for the specimens were both isotropic plastic hardening and the friction coefficient between specimen and indenter was 0.2. The Knoop indentation simulations comparing the load difference sensitivity in residual stress with wedge indentation were performed with 21,071 mesh elements. The simulation were supplemented by the linear relationship between two load differences and applied stress (150 MPa, 180 MPa and 250 MPa,  $p=0$ ). The S45C specimen with 150 MPa applied stress was intended to match the experimental data, and the purpose of considering

material STS 303 was to examine the feasibility of extending the new model to other types of materials. The size of specimen was 8 mm in the included angle direction (x-direction), 8 mm in the edge length direction (z-direction), and 4 mm in the indenting direction (y-direction). The mesh of the specimen beneath indenter was made up of a mesh region size 0.031 mm in the x-direction, 0.031 mm in the z-direction and 0.016 mm in the y-direction. The entire zone size with fine mesh was 0.50 mm, 3.0 mm, and 0.25 mm in the x-, z-, and y- directions, respectively: and as shown in Fig. 6.3 (b), the zone size covers the region directly penetrated by the indenter, and the highly deformed region that occurs in sink-in or pile up in indentation testing. For efficient analysis, the mesh size increases with distance from the indenter.

## **6.3 Results and Discussion**

### **6.3.1 Verification of Experiments with Stress-generating Jig**

In order to confirm the two set of load difference sum at  $90^\circ$  interval are converged, four times wedge indentation test are conducted on 7 combinations of materials and applied stress states (see Fig. 6.4).

To verify the wedge indentation model, indentation tests were performed on 16 combinations (Table 6.3) of materials and applied stress states, as mentioned in the previous section. Fig 6.5 shows the evaluated principal stress directions of uniaxial, equibiaxial, and nonequibiaxial stress states. Fig 6.6 is the results of evaluated principal stress ratios of uniaxial, equibiaxial, and nonequibiaxial stress states. Fig 6.7, Fig 6.8 and Fig. 6.9 are the evaluated results of maximum, minimum and summation of principal stress, these validations are shown to be within about  $\pm 20\%$  error range for the principal stress ratio and angle and  $\pm 30$  MPa for sum of stress magnitude. The results for all six materials suggest that the new model can be applied to common metallic materials for room-temperature wedge indentation tests.

### **6.3.2 Comparison of Residual Stress Sum with Previous Vickers Model**

In order to verify the novel developed indentation model, the magnitude of surface residual stress is evaluated with a Vickers indenter and wedge indenter. The residual stress with Vickers indenter is evaluated using Eq. (2-20) and that with wedge indenter is evaluated with Eq. (5-2). The contact area of Vickers indenter is observed by optical microscopy. The results are compared in Fig. 6.10.

As shown in Fig 6.10., the residual stress values from the wedge indentation model are reasonably matched, but a little bit overestimated compared to those from the Vickers indenter. This residual stress difference results from the inclusion of plastic pile-up. As the results from Vickers indentation model take plastic pile-up into account, the contact area is larger than in the wedge indentation model, which ignores plastic pile-up. The wedge indentation model takes into account only the load difference sum and constant conversion factor sum: for more accurate results, more consideration of contact morphology is needed.

**Table 6.1.**

Experimental and simulation conditions for determination of conversion factors: various materials and applied tensile stress states.

Number	Materials	Elastic modulus (GPa)	Yield strength (MPa)	Applied uniaxial tensile stress (MPa)
Experimental #1	S45C	202	320	75
Experimental #2	S45C	202	320	150
Experimental #3	SKD11	209	700	203
Experimental #4	SCM4	200	362	270
Simulation #1	S45C	202	320	150
Simulation #2	STS303	206	328	180
Simulation #3	STS303	206	328	200
Simulation #4	STS303	206	328	250



**Table 6.2.**

Mechanical properties of materials for model verification.

Materials	Poisson's ratio	Elastic modulus (GPa)	Yield strength (MPa)
Al6061	0.33	68.9	250
SKD11	0.27	209	700
S45C	0.29	212	343
STS304	0.29	193	215
STS316	0.27	193	250
STS440C	0.27	204	204

**Table 6.3.**

Applied stress state conditions and principal direction for model verification.

Classification	Materials	Applied			
		Stress (MPa)			Principal direction(°)
		$\sigma_1$	$\sigma_2$	$\sigma_1 + \sigma_2$	
Uniaxial	Al6061	55.1	0.0	55.1	40
	STS440C	255.0	0.0	255.0	20
	STS316	150.2	0.0	150.2	23
Equibiaxial	Al6061	50.1	49.3	99.4	40
	S45C	150.0	150.0	300.0	38
	STS440C	225.2	223.6	448.8	23
	STS304	76.4	75.8	152.3	15
	STS316	104.6	103.4	208.1	15
Nonequibiaxial	Al6061	136.8	54.8	191.6	35
	SKD11	174.9	35.9	210.9	28
	S45C	75.9	55.5	131.4	20
	STS440C	142.8	93.8	236.6	15
	STS440C	213.8	164.6	378.4	25
	STS304	109.8	57.9	167.7	0
	STS316	195.1	62.5	257.7	37

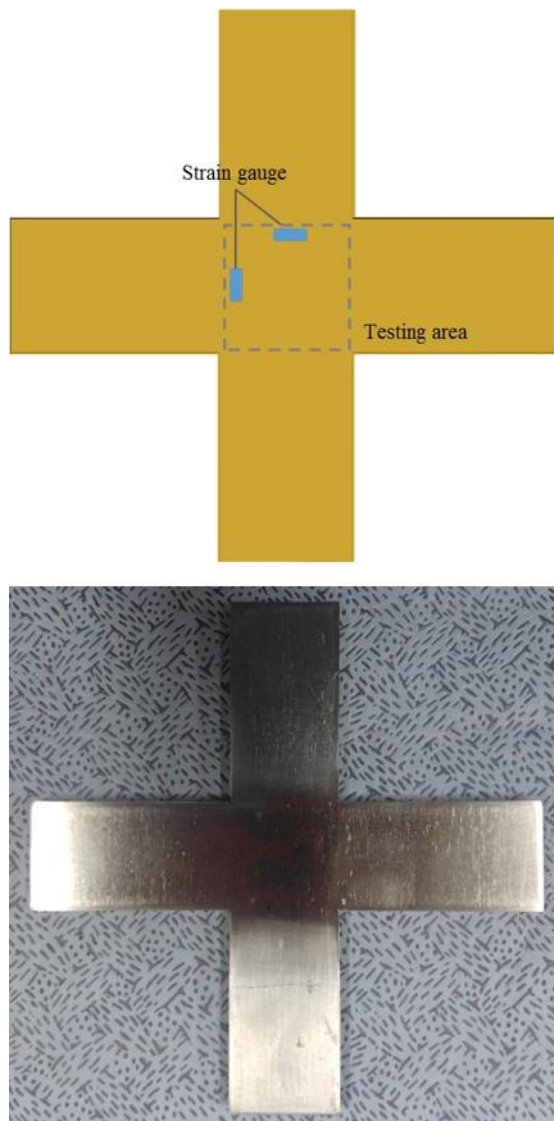
**Table 6.4.**

Summary of applied stress state conditions and evaluated stress magnitude and directionality.

Classification	Materials	Applied				Evaluated				
		Stress (MPa)			Principal direction(°)	Stress ratio	Stress (MPa)			Principal direction(°)
		$\sigma_1$	$\sigma_2$	$\sigma_1 + \sigma_2$		$P$	$\sigma_1 + \sigma_2$	$\sigma_1$	$\sigma_2$	
Uniaxial	Al6061	55.1	0.0	55.1	40	0.01	53.0	52.3	0.6	33.3
	STS440C	255.0	0.0	255.0	20	-0.07	210.5	227.5	-17.0	28.6
	STS316	150.2	0.0	150.2	23	0.09	176.9	161.6	15.3	30.5
Equibiaxial	Al6061	50.1	49.3	99.4	40	0.98	99.1	50.0	49.1	41.2
	S45C	150.0	150.0	300.0	38	1.02	305.5	151.3	154.1	27.8
	STS440C	225.2	223.6	448.8	23	0.74	398.5	228.7	169.8	23.1
	STS304	76.4	75.8	152.3	15	0.92	190.0	99.0	91.0	18.4
	STS316	104.6	103.4	208.1	15	1.11	216.7	102.8	113.8	9.8
Nonequibiaxial	Al6061	136.8	54.8	191.6	35	0.39	183.8	132.1	51.6	39.4
	SKD11	174.9	35.9	210.9	28	0.20	198.3	165.0	33.3	27.2
	S45C	75.9	55.5	131.4	20	0.85	138.3	74.7	63.6	19.8
	STS440C	142.8	93.8	236.6	15	0.58	205.2	129.5	75.7	16.5
	STS440C	213.8	164.6	378.4	25	0.75	368.5	210.5	158.0	31.2
	STS304	109.8	57.9	167.7	0	0.50	183.4	122.6	60.8	-2.4
	STS316	195.1	62.5	257.7	37	0.39	266.9	191.8	75.1	39.7

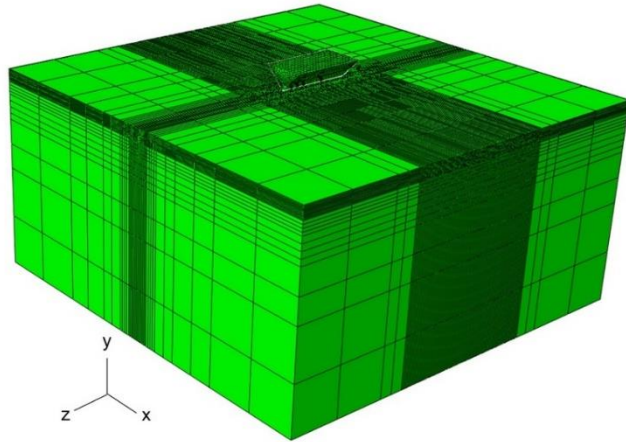


**Fig. 6.1** AIS 3000 equipment made by Frontics Inc.

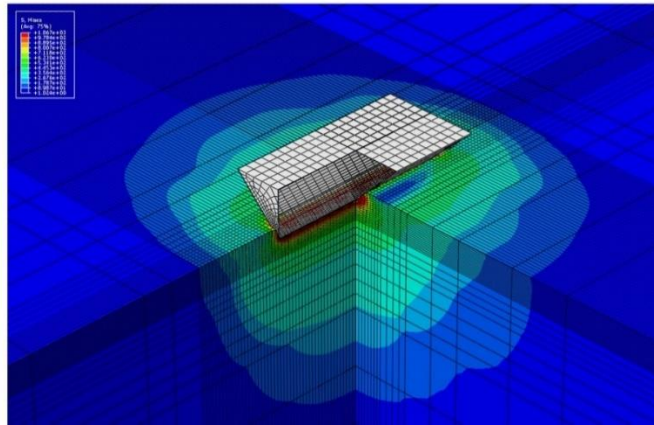


**Fig. 6.2** Schematic drawing and photograph of 10-mm-thick cruciform samples.

(a)

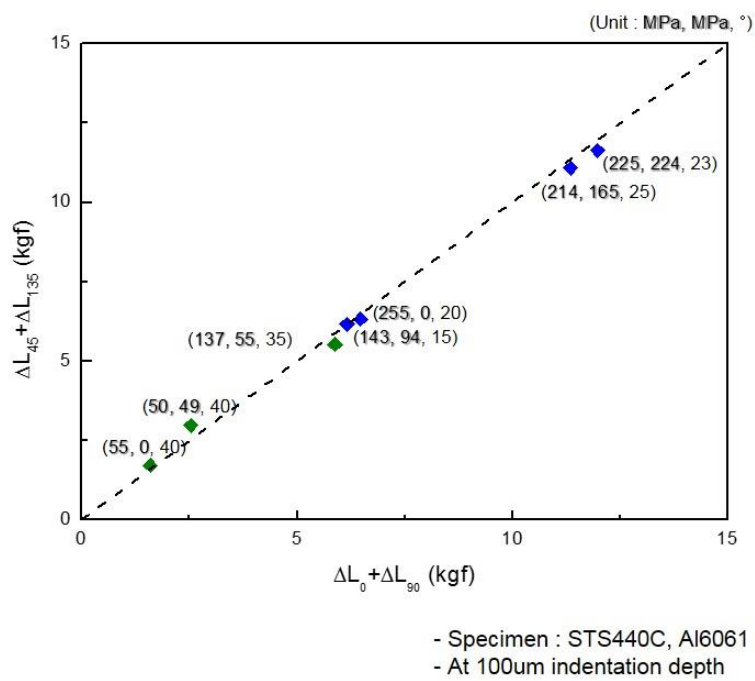


(b)

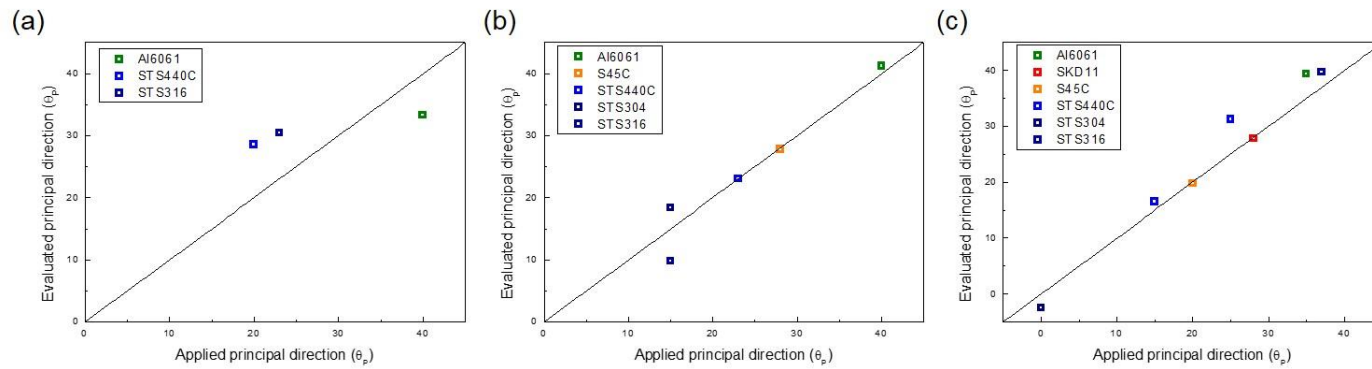


**Fig. 6.3** Finite Element Analysis modeling of wedge indentation

(a) meshed wedge indenter and specimen (b) deformed shape of specimen in wedge indentation.



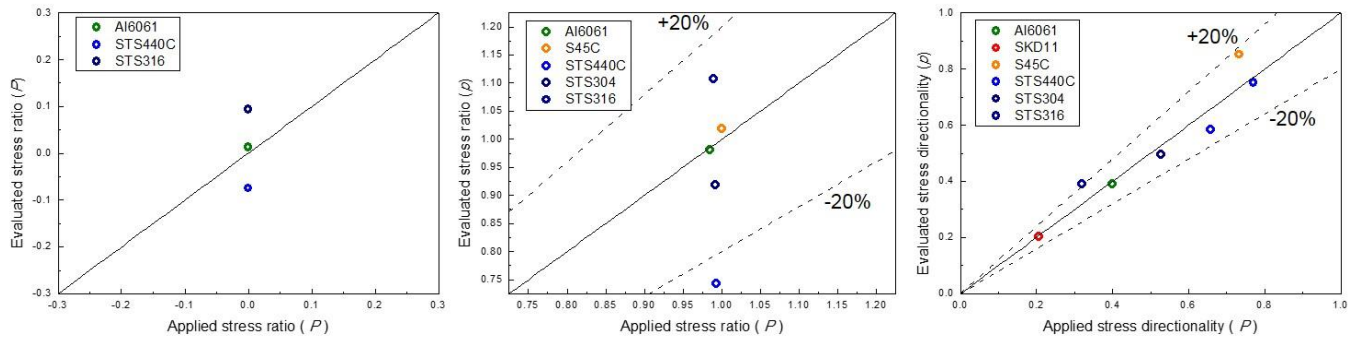
**Fig. 6.4** Verification of invariant residual stress sum.



**Fig. 6.5** Verification of principal direction:

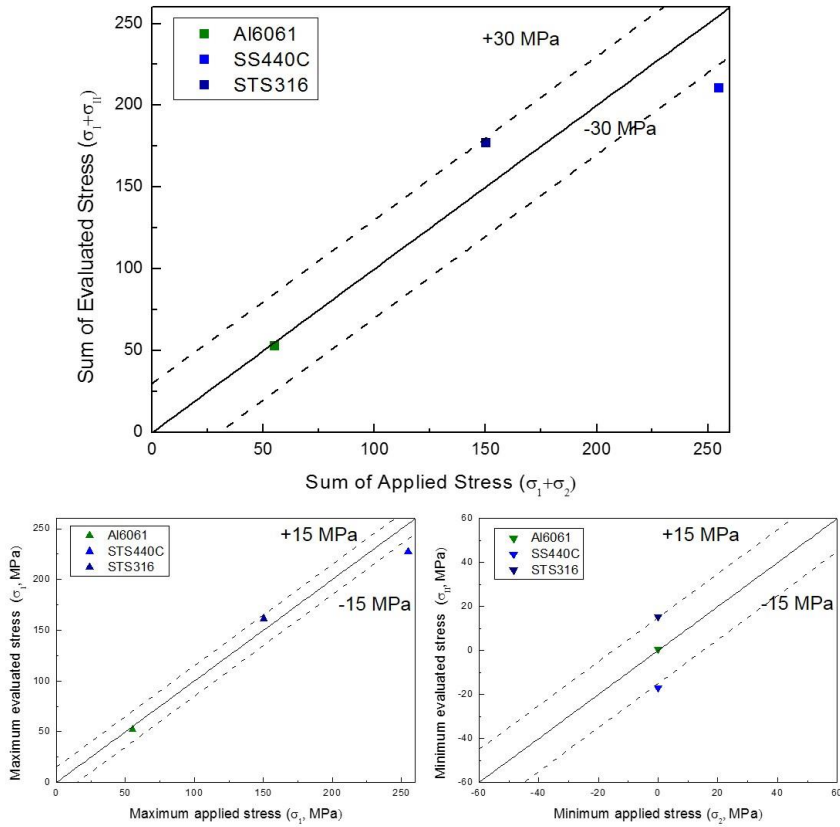
(a) uniaxial stress state, (b) equibiaxial stress state, (c) nonequibiaxial stress state.



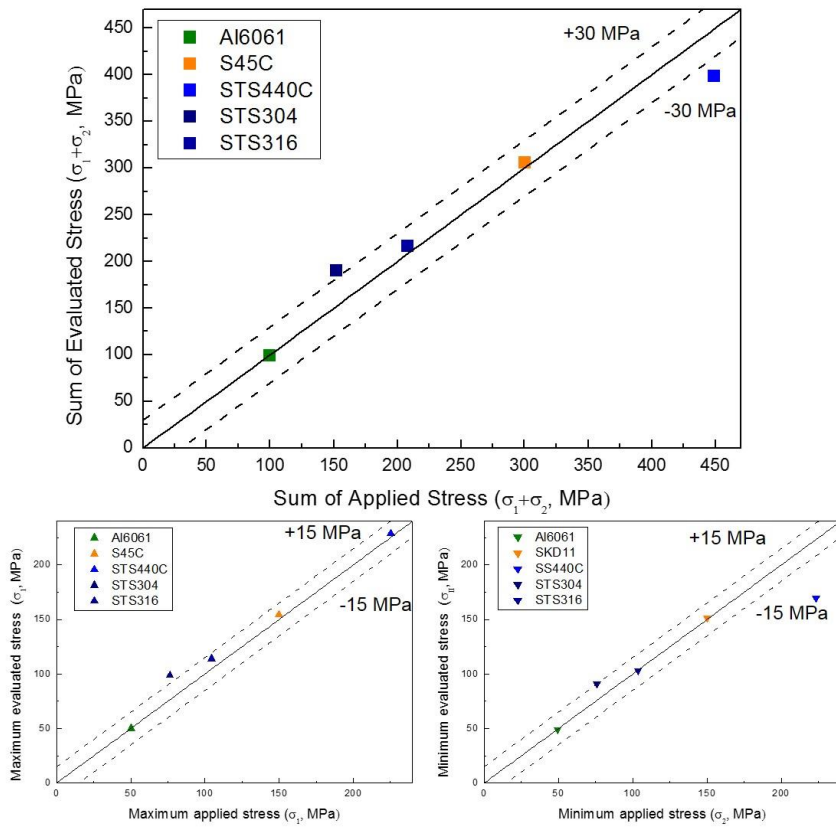


**Fig. 6.6** Verification of principal stress ratio:

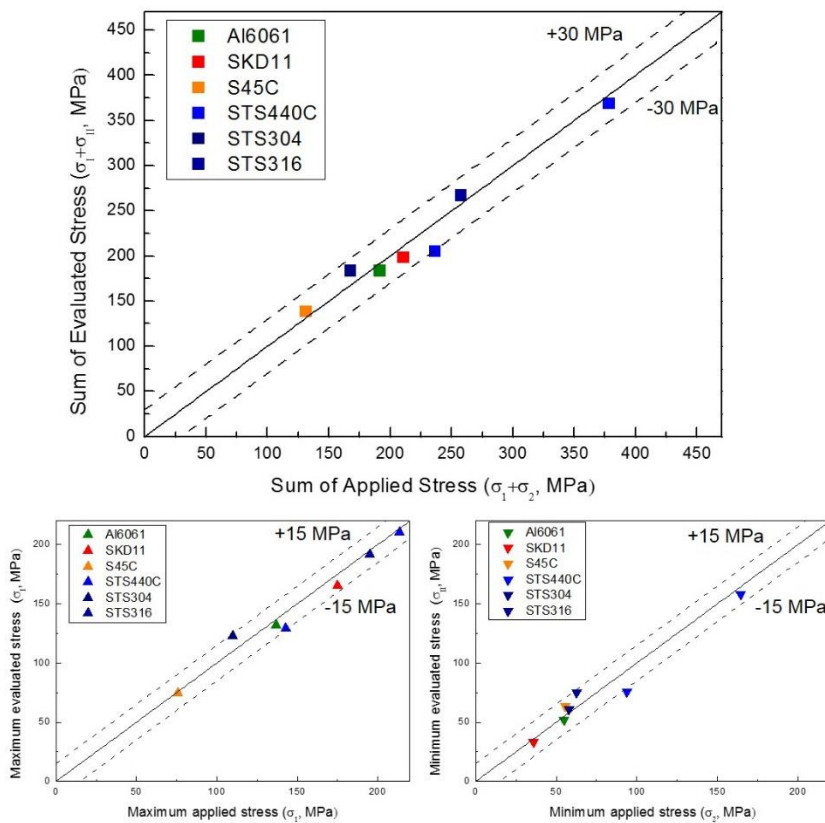
(a) uniaxial stress state, (b) equibiaxial stress state, (c) nonequibiaxial stress state.



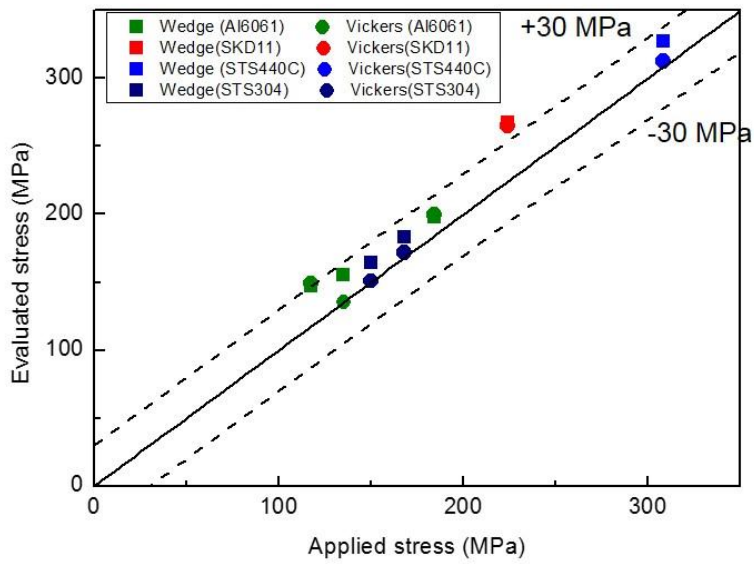
**Fig. 6.7** Verification of principal stress magnitude  
from uniaxial stress state.



**Fig. 6.8** Verification of principal stress magnitude  
from equibiaxial stress state.



**Fig. 6.9** Verification of principal stress magnitude  
from nonequibiaxial stress state.



**Fig. 6.10** Comparison stress magnitude sum  
between wedge indentation and Vickers indentation.

# Chapter 7

---

---

## Conclusion

A wedge indentation model is proposed to evaluate the biaxial residual stress using instrumented indentation test. The suggested model is modified from a previous model using both a Vickers and a Knoop indenter, since the latter is difficult to use in in-field testing and cannot be applied to facilities of certain shapes such as angled pipelines and weldments. In previous research, the ratio of conversion factors was taken as constant, based on empirical results because of the geometrical self-similarity in the long diagonal and short diagonal directions. To obtain the conversion factors of wedge indentation, experimental and finite element analysis are performed and the sum and ratio are determined. In addition, evaluating the sum of surface biaxial residual stress was modeled with two wedge indentations. A model for finding the principal stress direction and magnitude was suggested with four wedge indentation tests. On the basis of this result, two wedge indentation models were established for two testing conditions: known and unknown principal direction. The model was verified experimentally using a stress-generating jig, and the results show good agreement (within about 20% error or 30 MPa) in evaluating the applied principal direction and stress magnitude.

The primary results of this thesis are the following.

1. The wedge indentation model to evaluate and quantify the stress directionality  $p$  was described. From experiments on four combinations of materials and stress states and finite element analysis of four conditions, perpendicular and parallel conversion factors were obtained by linear slope between applied stress states and load differences. The conversion factor ratio was 0.463 and the sum of conversion factors was 0.03037 at 100  $\mu\text{m}$  indentation depth. The physical meaning of the conversion factor ratio was examined by matching the conversion factor ratio and the plastic zone size beneath the wedge indenter. Different from the conversion factor ratio for the Knoop indenter, the conversion factor for a wedge indenter has geometrical self-similarity on the included angle direction not on the edge length direction. It was also shown that the relationship between conversion factor ratio and indentation depth is linear and that the ratio of subjected plastic zone size is linear with indentation depth.
2. The model for evaluating the sum of surface biaxial residual stress was constructed with the sum of two load difference and sum of conversion factors. When there is no information on principal



directions, it was shown that the load differences set at  $90^\circ$  intervals could be used in evaluating residual stress magnitude.

3. Two wedge indentation models have been developed for two test conditions: for known principal direction and unknown principal direction: for these conditions two and four wedge indentation respectively, are necessary. The summary was attached in Fig.5.10.
4. For experimental verification of the wedge indentation model, indentation tests were performed on 16 combinations of materials and stress state using a stress-generating jig as summarized in Table 6-3. The results for the stress directionality from the new model show good agreement (within about 20% error range), and the stress magnitude results were valid to 15 MPa. In addition, these results suggest that the new model can be applied to general metallic materials.
5. To extend the validity of the wedge indentation model, it was compared to the previous Vickers indentation model. The evaluated values of residual stress magnitude values matched reasonably well (see Fig. 6.10).

## References

- [1] J. Lu, M. James, G. Roy: Handbook of Measurement of Residual Stresses (Fairmont press, Lilburn, 1996).
- [2] I.C. Noyan, J.B. Cohen: Residual Stresses (Springer-Verlag, New York, 1987).
- [3] S. Suresh, A.E. Giannakopoulos, Acta Mater. 46, 5755 (1998).
- [4] Y.-H. Lee, D. Kwon, Scripta Mater. 49, 459 (2003).
- [5] Y.-H. Lee, D. Kwon, Acta Mater. 52, 1555 (2004).
- [6] J.-H. Han, J.-S. Lee, Y.-H. Lee, M.-J. Choi, G. Lee, K.-H. Kim and D. Kwon, Key Eng. Mater, 345-346, 1125 (2007)
- [7] F. Knoop, C.G. Peters, W.B. Emerson, J. Res. Natl. Bur. Stand. 23, 39 (1939).
- [8] F. Ebrahimi, A. Gomez, T.G. Hicks, Scripta Mater. 34, 337 (1996).
- [9] M.E. Stevenson, M. Kaji, R.C. Bradt, J. Eur. Ceram. Soc. 22, 1137 (2002).
- [10] G.U. Oppel, Exp. Mech. 4, 135 (1964).

- [11] K. Zeng, A.E. Giannakopoulos, D. Rowcliffe, P. Meier, J. Am. Ceram. Soc. 81, 689 (1998).
- [12] A.E. Giannakopoulos, Th. Zisis, Int. J Solids Struc, 48, 175 (2011).
- [13] Th. Zisis, A.E. Giannakopoulos, Int. J Solids Struc, 48, 3217 (2011).
- [14] A.E. Giannakopoulos, Th. Zisis, Mech. Mater. 57, 53, (2013).
- [15] M.L. Weaver, M.E. Stevenson, R.C. Bradt, Mat. Sci. Eng. A 345 25, 113 (2003).
- [16] J. Borc, Materials Chemistry and Physics 137, 617 (2012).
- [17] P.J. Blau, Scr. Metal. 14, 719 (1980).
- [18] S. Mukerji, T. Kar, Mater. Res. Bull. 35, 711 (2000).
- [19] E. Amitay-Sadovsky, H.D. Wagner, Polymer 39, 2387 (1998).
- [20] J. Li, C. Ding, Surf. Coat. Tech. 135, 229 (2001).
- [21] P.E. Riches, N.M. Everitt, D.S. McNally, J. Biomech. 33, 1551 (2000).
- [22] E.K. Girija, G.R. Sivakumar, S. Narayana Kalkura, P. Ramasamy, D.R. Joshi, P.B. Sivaraman, Mat. Chem. Phys. 63, 50 (2000).
- [23] P.E. Riches, N.M. Everitt, A.R. Heggie, D.S. McNally, J. Biomech.

30, 1059 (1997)

[24] M.-J. Choi, Ph. D. thesis (Seoul National University, Seoul, 2012).

[25] V. Hauk: Structural and Residual stress Analysis by Nondestructive Methods (Elsevier Science B.V., Amsterdam, 1997)

[26] W. Cheng, I. Finnie: Residual Stress Measurement and the Slitting Method (Springer, 2007).

[27] T. Mura: Micromechanics of Defects in Solids (Martinus Nijhoff Publishers, Hague, 1982).

[28] K. Masubuchi: Analysis of Welded Structures: Residual Stress, Distortion, and their Consequences, (Pergamon Press Ltd, London, 1980)

[29] W.D. Nix, Metall. Mater. Trans. A 20, 2217 (1989)

[30] L.B. Freund, S. Suresh: Thin Film Materials: Stress, Defect Formation, and Surface Evolution, (Cambridge University Press, Cambridge, 2003)

[31] W.D. Nix, B.M. Clemens, J. Mater. Res. 14, 3467 (1999)

[32] F. Spaepen, Acta Mater. 48, 31 (2000)

[33] C.V. Thompson, Annu. Rev. Mater. Sci. 30, 159 (2000)

- [34] R.C. Cammarata, T.M. Trimble, D.J. Srolovitz, J. Mater. Res. 15, 2468 (2000)
- [35] J.A. Floro, M.B. Sinclair, E. Chason, L.B. Freund, R.D. Twisten, R.Q. Hwang, G.A. Lucadamo, Phys. Rev. Lett. 84, 701 (2000)
- [36] L.B. Freund, E. Chason, J. Appl. Phys. 89, 4866 (2001)
- [37] J.A. Floro, S.J. Hearne, J.A. Hunter, P. Kotula, E. Chason, S.C. Seel, C.V. Thompson, J. Appl. Phys. 89, 4886 (2001)
- [38] J.A. Floro, E. Chason, R.C. Cammarata, D.J. Srolovitz, MRS Bulletin 27, 19 (2002)
- [39] G.S. Schajer; Practical Residual Stress Measurement Methods, (Wiley-Blackwell, 2013)
- [40] P.A. Flinn, Mater. Res. Soc. Symp. Proc. 130, 41 (1989).
- [41] ISO 14577-1: Metallic Materials - Instrumented Indentation Test for Hardness and Materials Parameters - Part 1: Test Method (2002).
- [42] ISO 14577-2: Metallic materials - Instrumented indentation test for hardness and materials parameters - Part 2: Verification and calibration of testing machines (2002).

- [43] ISO 14577-3: Metallic materials - Instrumented indentation test for hardness and materials parameters - Part 3: Calibration of reference blocks (2002).
- [44] ISO 14577-4: Metallic Materials - Instrumented Indentation Test for Hardness and Materials Parameters - Part 4: Test Method for Metallic and Non-metallic Coatings (2007).
- [45] W.C. Oliver, G.M. Pharr, J. Mater. Res. 7, 1564 (1992).
- [46] K.L. Johnson, Contact Mechanics (Cambridge University Press, Cambridge, 1985).
- [47] J. Mencik, M.V. Swain, J. Mater. Res. 10, 1491 (1995).
- [48] K.W. McElhaney, J.J. Vlassak, W.D. Nix, J. Mater. Res. 13, 1300 (1998).
- [49] J. Alcala, A.C. Barone, M. Anglada, Acta Mater. 48, 3451 (2000).
- [50] J. Malzbendera, G. With, J. Mater. Res. 17, 502 (2002).
- [51] Y. Choi, H.S. Lee, D. Kwon, J. Mater. Res. 19, 3307 (2004).
- [52] E.C. Jeon, J.Y. Kim, M.K. Baik, S.H. Kim, J.S. Park, D. Kwon, Mater. Sci. Eng. A 419, 196 (2006).

- [53] S.H. Kim, B.W. Lee, Y. Choi, D. Kwon, Mater. Sci. Eng. A-Struct. 415, 59 (2006).
- [54] J.Y. Kim, K.W. Lee, J.S. Lee, D. Kwon, Surf. Coat. Tech. 201, 4278 (2006).
- [55] Y.H. Lee, J.H. Hahn, S.H. Nahm, J.I. Jang, D. Kwon, J. Phys. D-Appl. Phys. 41, 074027 (2008).
- [56] S.K. Kang, J.Y. Kim, C.P. Park, H.U. Kim, D. Kwon, J. Mater. Res. 25, 337 (2010).
- [57] O. Bartier, X. Hernot, G. Mauvoisin, Mech. Mater. 42, 640 (2010).
- [58] S.H. Kim, B.W. Lee, Y. Choi, D. Kwon, Mater. Sci. Eng. A-Struct. Mater. Prop. Microstruct. Process. 415, 59 (2006).
- [59] E. Jeon, M.K. Baik, S.H. Kim, B.W. Lee, D. Kwon, Key Engineering Materials, 297, 2152 (2005).
- [60] J.-H. Ahn, D. Kwon, Journal of Materials Research, 16, 3170 (2001).
- [61] K.-W. Lee, K.-H. Kim, J.-Y. Kim, D. Kwon. Journal of Physics D: Applied Physics. 41, 074014. (2008).
- [62] T.Y. Tsui, W.C. Oliver, and G.M. Pharr, J.Mater.Res. 11, 752 (1996).

- [63] A. Bolshakov, W.C. Oliver, and G.M. Pharr, J. Mater. Res. 11, 760 (1996).
- [64] J.G. Swadener, B. Taljat, And G.M. Pharr, J.Mater.Res. 16, 2091 (2001).
- [65] A.E. Giannakopoulos, J. App. Mech. 70, 638 (2003).
- [66] J.-I. Jang, J. Ceram. Process. Res. 10, 291 (2009)
- [67] Y.-H. Lee, K. Takashima, Y. Higo and D. Kwon, Scripta Mater. 49, 459 (2003).
- [68] M.-J. Choi, S.-K. Kang, I. Kang, and D. Kwon, J. Mater. Res. 27, 1 (2011).
- [69] Y.-C. Kim, M.-J. Choi, D. Kwon, and J.-Y. Kim, Metals Mater. Int., 21, 850 (2015)
- [70] Y.-C. Kim, H.-J. Ahn, D. Kwon, and J.-Y. Kim, Metals Mater. Int., 22, 12 (2016)
- [71] T.S. Byun, J.W. Kim, J.H. Hong, J. Nucl. Mater. 252, 187 (1998).
- [72] J.B. Ju, Ph. D. thesis in Seoul National University, (2003).
- [73] J.S. Lee, J.-i. Jang, B.W. Lee, Y. Choi, S.G. Lee, and D. Kwon, Acta.



Mater. 54, 1101 (2006).

[74] K.-W. Lee, Ph. D. thesis (Seoul National University, Seoul, 2011).

[75] G.E. Dieter, Mechanical Metallurgy (McGraw-Hill Book Co., New York, 1986).

[76] ISO/TR 29381: Metallic materials - Measurement of mechanical properties by an instrumented indentation test - Indentation tensile properties (2008).

[77] H.-J.Ahn, J.-h.Kim, H.Xu, J.Lee, J.-Y. Kim , Y.-C. Kim, and D. Kwon, Metals Mater. Int. (2016, Accepted)

[78] G.U. Oppel, Exp. Mech. 4, 135 (1964).

[79] G.E. Dieter, Mechanical Metallurgy (McGraw-Hill Book Co., New York, 1986)

[80] Y.-C.Kim, Ph. D. thesis (Seoul National University, Seoul, 2013).

[81] S.-K.Kang, Ph. D. thesis (Seoul National University, Seoul, 2011).

## 초 록

발전설비나 교통관련 구조물의 광범위한 손상은 생명의 손실을 유발하고 복구를 위해 많은 노력과 비용이 필요하기 때문에, 안전성 평가나 구조 신뢰성, 건전성 평가는 사고 예방에 매우 중요하다. 예기치 않은 사고나 고장을 막기 위해 구조물에 노출된 응력 상태를 고려해야 한다. 특히, 잔류 응력은 외부 하중이나 열응력 등의 다른 응력 없이 재료 또는 구조물에 존재하는 응력 상태로 정의된다. 재료를 제조하고 가공하는 거의 모든 과정에서 잔류응력이 발생하며, 이러한 잔류응력이 외부 응력과 결합되면, 균일하고 벌크 스케일 재료로부터 구해진 항복 강도 값 이하의 응력에서도 구조물의 손상이나 파괴가 발생된다. 또한, 사용 중 구조물의 신뢰성에도 영향을 끼치기 때문에, 잔류응력을 정량적으로 평가하는 것은 산업 구조물과 설비의 안전한 사용 및 경제적인 유지보수를 위한 기본요소이다.

연속압입시험법은 압입하중 - 깊이 곡선을 분석하여 기계적 특성을 평가하기 위해 고안된 기법으로 시험방법이 간편하고 원리가 간단하여 실구조물의 기계적 특성평가 및 잔류응력 평가에 활용되고 있다. 지난 수십 년 동안 연속압입시험법은 경도 및 탄성 계수를 넘어서 인장 특성, 파괴 인성, 피로 특성, 충격 특성, 계면 접착력 및 잔류 응력을 평가하는 방법론으로 확장되어 왔다.

연속압입시험법을 통한 잔류응력 평가기법은 무응력 상태의 시편 또는 지역과 응력이 존재하는 영역에 연속압입시험을 수행하여, 두개의 압입하중-깊이 곡선의

차이를 비교하는 것에 기반을 두고 있다. 한다. 기존의 연구는 Vickers 압입자를 사용하여 평균 표면 잔류 응력을 평가했으며, Knoop 압입자라는 비대칭 압입자를 사용하여 주응력방향 및 응력비를 평가하였다. 그러나 기존 연구에서는 용접부 부근의 잔류응력 분포변화 양상을 파악하거나, 곡면부 파이프 등 압입시험 수행에 필요한 면적을 최소화 해야하는 이슈가 존재하였기 때문에, 본 논문에서는 wedge 압입자를 활용하여, 잔류응력의 방향성 및 크기 평가법을 제안하고자 연구를 수행하였다.

본 연구에서는 기존의 Knoop 압입시험모델 적용에 필요한 면적에 절반정도가 되도록 길이와 내각으로 구성된 wedge 압입자의 형상을 제안하였다. 이렇게 제안된 압입자가 잔류응력 평가에 효용성이 있는지 검토하기 위해 유한요소해석을 수행하였으며, 압입면적 축소 대비 타당한 잔류응력 민감도를 확인하였다. 또한 wedge 압입자만의 응력환산계수를 실제 실험과 유한요소해석을 병행하여 확보하였으며, 응력환산계수의 비를 압입자 하부의 소성변형면적 비율과 연계하여 그 물리적 의미를 설명하였다. 또한, 잔류응력의 크기는 응력환산계수의 합과 90도 간격으로 수행된 압입시험의 하중 차의 합으로 모델링하였으며, 주응력 방향에 대한 사전정보의 유무에 따라 2 회 압입시험 또는 4 회 압입시험을 통해 얻어진 하중차와 응력환산계수의 비를 통해 잔류응력의 방향성 평가법에 대한 모델링을 수행하였다.

새롭게 고안된 wedge 압입 모델을 검증하기 위해 응력유도지그와 다양한 소재 및 응력상태의 조합으로 구성된 금속십자시편을 제작하여 검증하였다. 또한 새로운

모델과 기존의 Vickers 압입시험 모델을 비교하여 두 가지 데이터에서 서로 좋은 일치성을 확인하였다.

주요어: 잔류응력; 연속압입시험법; Wedge 압입자; 응력환산계수; 응력크기; 응력 방향성

학 번: 2010-20614